Die approbierte Originalversion dieser Diplom-/Masterarbeit ist an der Hauptbibliothek der Technischen Universität Wien aufgestellt (http://www.ub.tuwien.ac.at).

The approved original version of this diploma or master thesis is available at the main library of the Vienna University of Technology (http://www.ub.tuwien.ac.at/englweb/).

DIPLOMARBEIT

Structural Design of a Miniaturised Bi-Propellant Thruster for the Attitude Control of Satellites

ausgeführt zum Zwecke der Erlangung
des akademischen Grades eines Diplom-Ingenieur
unter der Leitung von

O.Univ.Prof. Dipl.-Ing. Dr. Franz Rammerstorfer

Institut für Leichtbau und Struktur-Biomechanik (E317)

eingereicht an der Technischen Universität Wien
Fakultät für Maschinenwesen und Betriebswissenschaften

von

Georg Decker
E700/e0325472
Obere Zweiggasse 3
9524 Villach

Wien, im Oktober 2011

Abstract

This work originated as part of GRASP (Green Advanced Space Propulsion) project, founded by the European Union to research and develope environmentally friendly and sustainable Green Propellants for spacecraft. A preliminary design study of a miniaturised liquid bi-propellant thruster, to be operated with the fuels ethanol or kerosene and hydrogen peroxide as oxidizer was created. The thruster is being cooled by radiative heat transfer into space. An exemplaric model was derived from this study for the coming thermo-mechanical inquiry of the structure by utilizing the Finite elements analysis (FEA). The physics to describe the fluid flow, as well as the heat transfer from the fluid into the wall of the thrust chamber are progammed in the APDL language and implemented during the FEA. A concurrent enquiry to find suitable materials finally resulted in a combination of either a platinum-rhodium alloy or iridium as a material for the thrust chamber and a nickel base alloy used for parts with moderate thermal loads. The physical and mechanical material properties were implemented as temperature dependent quantities. The materials were mechanically idealised for the analysis to be of perfect plasticity post yield type. The thermo-mechanical stress analyses with regard to the stationary operating conditions in addition to transient heating were conducted with a three dimensional thruster model. The results showed that an inquiry of the structural effects, in response to thermal cyclic loading, by using a 2-D axially symmetric thruster model was justified. It was found that both materials undergo strong ratcheting in the proximity of the bi-material joint in this case.

Kurzfassung

Diese Arbeit entstand im Zuge des GRASP (Green Advanced Space Propulsion) Projekts der Europäischen Union zur Erforschung alternativer, umweltfreundlicher Treibstoffe, sogenannter "Green Propellants" für Raumfahrzeuge. Dafür wurde eine Entwurfstudie eines miniaturisierten Zweistofftriebwerks, welches mit den Treibstoffen Kerosin oder Ethanol unter Verwendung von Wasserstoffperoxid als Oxidator betrieben werden kann, erstellt. Das Triebwerk wird durch Wärmeabstrahlung in den Raum gekühlt. Dieser Entwurf wurde als exemplarisches Modell für die weitere thermomechanische Untersuchung der Struktur mittels der Finite Elemente Methode (FEM) herangezogen. Die Physikalischen Methoden zur Erfassung der Strömungsverhältnisse und zur Modellierung des Wärmeübergangs der Verbrennungsgase beim Durchströmen der Brennkammer und der Expansionsdüse wurden als APDL-Routinen programmiert und in die FEM-Analyse implementiert. Parallel dazu wurde eine Recherche zur Auswahl geeigneter Materialien durchgeführt, wobei die Entscheidung letztlich auf die beiden Materialkombinationen einer Platin-Rhodium Legierung sowie Iridium für die Brennkammer und Düse und einer Nickelbasis Legierung für den Einsatz in thermisch geringer belasteten Triebwerkskomponenten fiel. Die physikalischen und mechanischen Materialeigenschaften wurden der Analyse als temperaturabhängige Größen zugeführt. Das mechanische Verhalten der Werkstoffe wurde als elastisch-ideal plastisch angenommen. Ein dreidimensionales Modell wurde zur thermomechanischen Spannungsanalyse der stationären Betriebszustände, als auch während des transienten Anfahrverhaltens des Triebwerks verwendet. Dies rechtfertigte die Verwendung eines rotationssymmetrischen 2-D Modells zur Untersuchung der Auswirkungen von thermisch zyklischen Belastungen. In diesem Lastfall wurden speziell im Bereich der Fügestelle beider Materialen in großem Ausmaß auftretendes Ratcheting festgestellt.

Acknowledgement

First and foremost, my gratitude is to my adviser Prof. Dr. Franz Rammerstorfer for his valuable suggestions and discussions concerning the present work. He is also the person I owe not only my interest on structural mechanics but a critical perception regarding the former.

I also want to express my thank to the people from the Space Propulsion & Advanced Concepts group at AIT Austrian Institute of Technology. Particularly Dr. Martin Tajmar, Dr. Carsten Scharlemann and Dr. Alexander Woschnak for the opportunity to acquire practical experience in this discipline.

I would like to thank Ing. Friedrich Druck for his offers to come in touch with interesting mechanical engineering tasks.

I am deeply grateful, because none of this would have been possible without the caring support of my parents Burgi and Karl.

I want to thank Sylvia for being the wonderful lady she is.

Contents

Abstract i

Kurzfassung ii

Acknowledgement iii

1 Introduction 1
- 1.1 Propulsion Systems 1
- 1.2 Fundamentals of Thermal Propulsion Systems 4

2 GRASP Bi-Propellant Thruster 7
- 2.1 Motivation 7
- 2.2 Miniaturised Liqud Bi-Propellant Thrust Engine 8
- 2.3 Engine Components 8
  - 2.3.1 Decomposition Chamber and Catalyst 8
  - 2.3.2 Combustion Chamber 10
  - 2.3.3 Nozzle 10
- 2.4 Thruster Performance and Geometrical Dimensions 11

3 Materials 16
- 3.1 Thrust Chamber Materials 16
  - 3.1.1 Platinum-Rhodium Alloy 17
  - 3.1.2 Iridium 18
- 3.2 Material of the Decomposition Chamber and Remaining Parts 22
- 3.3 Material implementation in FEM 24

4 Modelling of the Thruster 25
- 4.1 Geometric Model 25

4.2 Thermal Loads 31
4.2.1 Convective Heat Transfer Inside the Nozzle and Combustion Chamber 31
4.2.2 Radiative Heat Transfer at Exterior Surfaces 40
4.2.3 Further Contributions to Heat Transfer 41
4.3 Mechanical Loads 42
4.4 Thermal and Structural FEA Model 44

5 FEA Results and Discussion **50**
5.1 Material Combination with Pt-10%Rh DPH 50
5.1.1 Stationary Thermal Analysis 50
5.2 Material Combination with Iridium 52
5.2.1 Thermal Analysis of the 3-D Model 52
5.2.2 3-D Thermo-Stress Analysis 58
5.2.3 2-D Cyclic Thermo-Stress Analysis 65

6 Conclusion **71**

A Appendix **73**
A.1 Integrals from the turbulent boundary-layer analysis 73

Bibliography **76**

1 Introduction

Since ever Propulsion in space has been linked to outstanding solutions towards optimal performance. This thesis is part of a greater effort to develope a miniaturised bipropellant thruster, using "Green Propellants".

The main subject is the investigation of thermo-mechanical loads exerted on the structural parts of this thruster during operation with the finite elements analysis (FEA). Here the focus is drawn to the thrust chamber, considered to be the most critical component. In conjunction to the mechanical analysis, a selection of suitable materials as well as the definition of geometrical dimensions for a preliminary design study of the thruster are further contributions.

1.1 Propulsion Systems

Propulsion systems represent fundamental components for the majority of spacecrafts launched from earth into space. Their reliability of operation together with accurate operating characteristics are crucial factors of success during specific periodes of a mission in space. Currently the generation of thrust is mainly based on the conservation of momentum of a spacecraft or rocket and the propellant, expelled from the former with a specific exhaust velocity. They can be classified into primary or main engines and secondary propulsion systems [25], due to their utilisation during the mission as listed in Table 1.1. Another way to classify propulsion systems is to distinguish between specific attributes as listed below [53]:

- Type of energy used to accelerate the propellant
    - Chemical energy (liquid and solid propellants)
    - Electric energy (electrothermal, electromagnetic, electrostatic)

  - Nuclear energy (nuclear fission)
- Internal or external supply of energy
- Internal or external propellant and without propellant

Table 1.1: Classification of Propulsion Systems according to typical applications, where Δv is the required change of velocity and F stands for the thrust.

Primary Systems	**Secondary Systems**
Launch vehicle propulsion $\Delta v \approx 7 - 11$ km/s F in the range of MN	*Orbit control* $\Delta v \approx 10 - 600$ m/s $F \approx 0.5 - 100$ N
Orbit transfer propulsion $\Delta v \approx 1$ up to a couple of km/s F in the range of kN (N for electric propulsion)	*Attitude control, station-keeping* $\Delta v \approx 20$ m/s $F \approx 1$mN $- 10$ N

In all conventional chemical propulsion engines the energy to generate thrust is stored inside the propellants and set free by means of a chemical reaction. They can be divided into following types:

Liquid propellant rocket engines Monopropellant and bipropellant configuration (fuel plus oxidizer)

Solid propellant rocket engines Basic configuration (the solid propellant contains both fuel and oxidizer) and hybride configuration (the solid charge contains only the fuel, the oxidizer is a separate liquid)

Solid propellant engines are primarily used as boosters during the first stage of the launch periode in some spacecrafts, namely the Ariane 5, and the former Space Shuttles. Liquid monopropellant thrusters are operated with a metastable, reactive propellant which decomposes into a gaseous fluid if brought into contact with a certain catalyst. Hydrazine (N_2H_4) and hydrogen peroxide (H_2O_2) are commonly used propellants but there are attempts to find candidates with higher decomposition temperatures like ammonium dinitramide (ADN), as discussed in [12]. Liquid bipropellant systems typically use oxidizers like oxygen (LOX) or mixed oxides of nitrogen (MON)

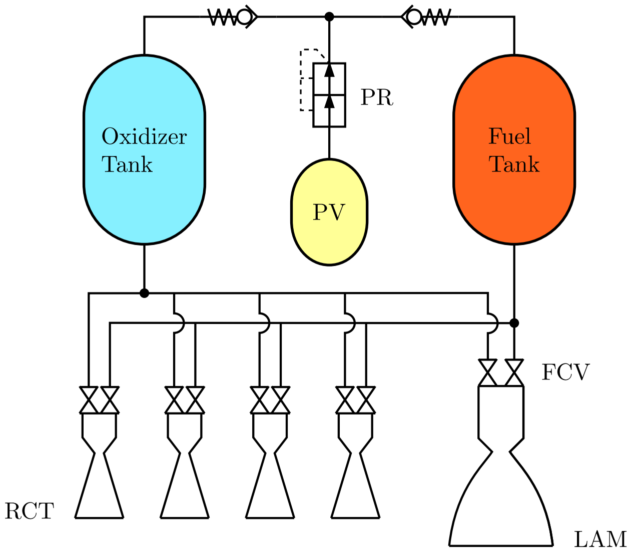

Figure 1.1: Basic schematic of a gas-pressure-fed, liquid bipropellant propulsion system for satellites. *PR* Redundant series pressure regulator, *PV* Pressure vessel, *FCV* Flow control valves, *LAM* Liquid apogee motor, *RCT* Reaction control thrusters.

and fuels like hydrogen (LH2), kerosene or monomethyl-hydrazine (MMH), to be burned in the combustion chamber.

The thruster focused on in this work is a miniaturised, liquid fuelled bipropellant engine with a nominal thrust of 1 N. Possible applications for the 1 N thruster class comprise the fields of secondary propulsion systems as listed in Table 1.1. Especially attitude maintenance, earth and sun acquisition, station-keeping, relocation in geostationary orbits (GEO), atmospheric drag compensation in low earth orbits (LEO), or de-orbit manoeuvres at the end of life. It could also be used as an apogee motor to transfer micro-satellites from intermediate launch orbits into final orbits. In the basic configuration of a liquid propulsion system for satellites, as shown in Figure 1.1, the apogee motor as well as the reaction control thrusters use the same propellants, thus saving structural mass in addition to a simplification of the piping and the regulation devices to control the flow of fluid. The number and type of thrusters and their arrangement within a satellite bus depends on several points e.g. the satellite mass and distribution, disturbances and the accuracy and timespan of on-orbit manoeuvres. Considering different propulsion system layouts like the MYRIADE micro satellites, designed for LEO up to 1000 km with a mass of 120 kg are equiped with four 1 N thrusters [19], compared with the large AlphaBus for satellites to operate in geostationary orbit GEO with a mass between 6 and 8 tonnes using a 500 N apogee motor and 16 attitude control thrusters each delivering 10 N [18].

1.2 Fundamentals of Thermal Propulsion Systems

The principle of classical rocket propulsion is based upon the change of momentum of an object if mass is ejected from it with a certain relativ velocity. This can be expressed by the momentum equation applied to a control volume V which envelopes a rocket engine that moves with the velocity $\vec{v}$ in a fixed coordinate system (Figure 1.2)

$$\frac{\mathrm{d}\vec{J}}{\mathrm{d}t} = \vec{R} - \oint\limits_{\partial V} \rho(\vec{u}\cdot\vec{n})\vec{v}_{abs}\mathrm{d}S, \quad \vec{v}_{abs} = \vec{u} + \vec{v}, \quad \vec{R}\ldots \text{external forces acting upon } V.$$

Allowing only pressure loads to act upon the control volume in the following the first expression is found to be

$$\vec{R} = \oint\limits_{A_e}(-p_e)\vec{n}\mathrm{d}S + \oint\limits_{\partial V - A_e}(-p_a)\vec{n}\mathrm{d}S = A_e(p_a - p_e)\vec{n}_e,$$

where A_e is the cross-sectional area at the end of the nozzle, p_a and p_e are the pressures of the ambient and at the exit of the nozzle respectively. The momentum flow results in

$$\oint\limits_{\partial V} \rho(\vec{u}\cdot\vec{n})\vec{v}_{abs}\mathrm{d}S = \oint\limits_{A_e} \rho(\vec{u}\cdot\vec{n})\vec{v}_{abs}\mathrm{d}S = \rho_e u_e A_e(\vec{u}_e + \vec{v}),$$

where u_e is the exhaust velocity, relative to the rocket. Another way to express the change of momentum of the rocket is to differentiate the product of its mass M_R and velocity $\vec{v}$ with respect to time yielding

$$\frac{\mathrm{d}\vec{J}}{\mathrm{d}t} = \frac{\mathrm{d}\vec{v}}{\mathrm{d}t}M_R + \frac{\mathrm{d}M_R}{\mathrm{d}t}\vec{v} = \frac{\mathrm{d}\vec{v}}{\mathrm{d}t}M_R - \dot{m}\vec{v}, \quad \text{where} \quad \frac{\mathrm{d}M_R}{\mathrm{d}t} = -\dot{m} = -\oint\limits_{A_e} \rho(\vec{u}\cdot\vec{n})\mathrm{d}S = -u_e\rho_e A_e$$

is the decrease of the rocket mass due to the mass flow rate of the propellant. The combination of both momentum equations and rearrangement gives the following expression with regard to the y-direction

$$\frac{\mathrm{d}v}{\mathrm{d}t} M_R = \rho_e u_e^2 A_e + A_e(p_e - p_a) = \dot{m} u_e + A_e(p_e - p_a) = F \tag{1.1}$$

which is known as the *thrust equation.* In the next step thermodynamic relations are introduced to link unknown quantities of the thrust equation 1.1 with thermal parameters of the fluid. The gaseous fluid in the rocket engine is assumed to have ideal gas characteristics. The energy released by the internal combustion or catalytic decomposition raises the temperature of the gas up to T_c at a constant pressure p_c in the chamber. At the inlet of the convergent part of the De Laval nozzle the gas undergoes an expansion process, thereby accelerated towards the divergent section. The expansion is assumed to be isentropic and the motion of the gas through the nozzle is an idealized one-dimensional flow [32]. If the ratio of ambient to chamber pressure is lower as or equal to the ratio of critical to chamber pressure then the velocity in the throat u_t is equal to the critical sonic velocity c_{crit} (or $M_t = u_t/c_{crit} = 1$),

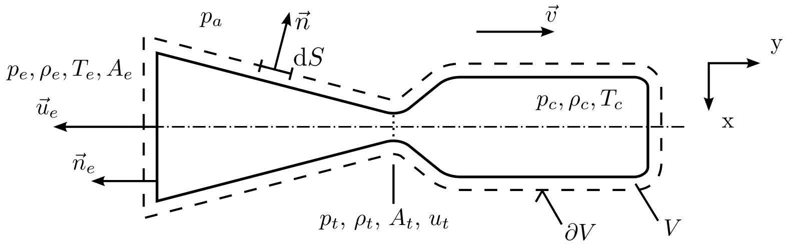

Figure 1.2: Moving rocket engine.

$$\frac{p_a}{p_c} \leq \frac{p_{crit}}{p_c} = \left(\frac{2}{\kappa+1}\right)^{\frac{\kappa}{\kappa-1}}, \quad c_c = \sqrt{\kappa R T_c} \rightarrow u_t = c_{crit} = c_c \left(\frac{2}{\kappa+1}\right)^{\frac{1}{2}} = \left(\frac{2 R T_c \kappa}{\kappa+1}\right)^{\frac{1}{2}}.$$

Together with the term for the density ρ_t and the area A_t in the cross section of the throat

$$\rho_t = \rho_{crit} = \rho_c \left(\frac{2}{\kappa+1}\right)^{\frac{1}{\kappa-1}} = \frac{p_c}{R T_c} \left(\frac{2}{\kappa+1}\right)^{\frac{1}{\kappa-1}},$$

the mass flow rate is found to be

$$\dot{m} = A_t u_t \rho_t = p_c A_t \left[\frac{\kappa}{RT_c} \left(\frac{2}{\kappa+1} \right)^{\frac{\kappa+1}{\kappa-1}} \right]^{\frac{1}{2}} . \tag{1.2}$$

By applying the principle of energy conservation between the entry of the chamber (where the velocity is small enough to be neglected) and the exit of the nozzle combined with the isentropic relation between pressure and temperature the exhaust velocity u_e can be written as

$$u_e = \left[\frac{2\kappa R T_c}{\kappa - 1} \left(1 - \frac{p_e}{p_c} \right)^{\frac{\kappa-1}{\kappa}} \right]^{\frac{1}{2}} . \tag{1.3}$$

Substitution of the mass flow rate and the exhaust velocity in equation (1.1) with (1.2) and (1.3) and some rearrangement the thrust equation can we rewritten as

$$F = p_c A_t \left[\frac{2\kappa^2}{\kappa - 1} \left(\frac{2}{\kappa+1} \right)^{\frac{\kappa+1}{\kappa-1}} \left(1 - \frac{p_e}{p_c} \right)^{\frac{\kappa-1}{\kappa}} \right]^{\frac{1}{2}} + A_e(p_e - p_a). \tag{1.4}$$

In this equation terms containing the gas constant R cancel, which points out that the thrust is not influenced by the molar mass $\mathcal{M}$ of the exhaust gas (since $R = \mathcal{R}/\mathcal{M}$, where $\mathcal{R}$ stands for the universal gas constant). Although the influence of the molar mass from the propellant of choice is clearly found from equation(1.2) which is proportional to the square root of $\mathcal{M}$. The mass flow rate $\dot{m}$ is not only reduced by a lower molar mass but also with an increase of the combustion temperature T_c. The same conditions lead to an increase of the exhaust velocity as seen from equation (1.3). A low mass flow rate coupled with a higher exhaust velocity to retain the thrust level, increases the burning time for a specified amount of propellant mass thus yielding a higher gain of impulse. Integration of the thrust equation (1.1) in its simpliest form gives

$$\Delta v = u_e \ln \left(\frac{M_0}{M_0 - M_P} \right) , \tag{1.5}$$

where M_0 is the mass of the spacecraft at the time of ignition and M_P is the consumed mass of propellants. Hence the effect of a higher exhaust velocity increases the resulting change of the spacecraft velocity Δv for a specific amount of propellant.

2 GRASP Bi-Propellant Thruster

2.1 Motivation

Green advanced space propulsion (GRASP) is a research project funded by the European Union (EU) which started in December 2008 over a duration of 3 years. The research is aimed at the developement of ecologically sound, non-polluting propellants for spacecrafts, referred to as "Green Propellants". Today hydrazine and its derivatives like MMH together with appropriate oxidizers are widely-used in secondary propulsion systems, see [26] and [54]. Their benefits are good storage capability at room temperature, low system complexity and flight proven, reliable operation in continuous and pulsed mode. The disadvantages in short are a low exhaust velocity of about 1700 ms^{-1} for hydrazine used as mono-propellant and the highly toxic and carcinogenic effects which require special safty measures for handling. Due to the latter issue the assembly hangar or the vehicle launch site has to be evacuated during fuelling only a short time before take off. Avoiding these potential environmental hazards by the use of harmless Green Propellants would also lead to a reduction of costs during the flight preparation [40]. The work in connection to this thesis, is focused on the structural design of the thruster. The main contribution is the investigation of the structural response of the combustion chamber and nozzle due to thermo-mechanical loads exerted during the operation.

2.2 Miniaturised Liqud Bi-Propellant Thrust Engine

Within the framework of the GRASP project general conditions for the utilization of Green Propellants and the design a bi-propellant thruster are beeing examined. Hydrogen peroxide (H_2O_2) with a concentration of 87.5 % was chosen as a liquid oxidizer. In conjunction to this selection two types of liquid hydrocarbons, ethanol and kerosene are to be considered as fuel propellants.

Important parts of the project linked to the thruster design are:

- Design and material selection of different catalyst types for hydrogen peroxide followed by tests with an experimental decomposition chamber model to characterise the catalytic reaction
- Experimental ignition tests carried out at a test bed including the decomposition chamber model together with an adjustable combustion chamber model. Both propellants, the liquid fuel and H_2O_2 in its decomposed gaseous state, are injected into the combustion chamber to specify conditions which cause a spontaneous self-ignition to trigger the combustion

2.3 Engine Components

The bi-propellant thruster and its functional units are depicted in a flow sheet as shown in Figure 2.1. The main structural parts are the decomposition and the combustion chamber, together with the nozzle, which are linked by the propellant manifold. Further components are the catalyst, propellant lines with the throttle and flow control valves, and the injectors.

2.3.1 Decomposition Chamber and Catalyst

The decomposition chamber is functionally equal to a pressure vessel. Towards the propellant supply side the chamber is closed by a cap with the inlet, to which the

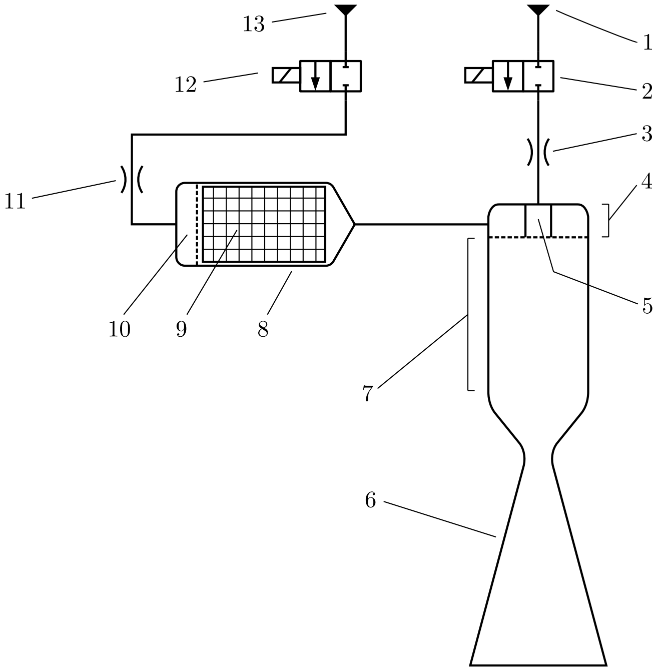

Figure 2.1: Components of the GRASP bi-propellant thruster: *1* Fuel supply interface (Ethanol/Kerosene), *2* Flow control valve (FCV) fuel, *3* Fuel line throttle valve, *4* Propellant manifold with oxidizer injector, *5* Fuel injector, *6* De Laval nozzle, *7* Combustion chamber, *8* Decomposition chamber, *9* Catalyst, *10* Decomposition chamber injector, *11* Oxidizer line throttle valve, *12* FCV oxidizer, *13* Oxidizer supply interface.

propellant supply pipe is connected. Inside the chamber the injector for the liquid hydrogen peroxide is placed adjacent to the inlet. The incoming liquid is atomized by the injector and directed to the face of the catalyst. Hydrogen peroxide undergoes an exothermal decomposition into oxygen and water vapour while passing through the catalyst

$$\mathrm{H_2O_2} + x_w \mathrm{H_2O} \;\longrightarrow\; (1 + x_w)\mathrm{H_2O} + \frac{1}{2}\mathrm{O_2}.$$

The concentration of the aqueous hydrogen peroxide solution is specified to be $C =$ 87.5 wt. %. The molar fraction x_w is determined by the mass fraction of water in the solution and the relation of the molar masses of water and H_2O_2 which gives

$$x_w = \frac{\mathcal{M}_{\mathrm{H_2O_2}}}{\mathcal{M}_{\mathrm{H_2O}}} \left(\frac{1 - C}{C} \right) = \frac{34.014}{18.015} \left(\frac{1 - 0.875}{0.875} \right) = 0.2697 \text{ mol}.$$

From the exit of the decomposition chamber the hot gases are transferred into the propellant manifold of the thruster.

2.3.2 Combustion Chamber

Both propellant lines are attached to the propellant manifold, which is mounted on top of the combustion chamber. The manifold passes the separate fluid streams to the attached injector, which directs them into the combustion chamber. The geometry of the injector is configured in a way that both propellants are sufficiently mixed to create a self-igniting gas shortly after entering the chamber. The volume of the combustion chamber, per definition this is the volume lying between the injector and the nozzle throat section, is determined by the expression

$$V_c = \frac{\dot{m} t_s}{\rho_c} = A_t L^*, \tag{2.1}$$

where t_s is the propellant stay time in the chamber. L^* is the empirically found characteristic length that guarantees a sufficient residence time of the gases in the chamber to establish a stationary and complete combustion. Considering the propellant configuration of hydrogen peroxide/RP-1 a range of the characteristic length $L^* = 1.525 - 1.780$ m is given in [32]. The shape of the combustion chamber is chosen to be cylindrical, as shown in Figure 2.2, with the cross-sectional area $A_c = \varepsilon_c A_t$ (ε_c is the contraction area ratio) and having the length l_c. From this configuration, with the convergent cone to be included and edge radii neglected, the combustion chamber volume is calculated according to

$$V_c = \left[R_c^2 l_c + \frac{(R_c^3 - R_t^3)}{3 \tan\theta} \right] \pi. \tag{2.2}$$

2.3.3 Nozzle

A convergent-divergent De Laval nozzle is connected to the end of the combustion chamber. The combusted gases entering the nozzle with a relatively low flow velocity

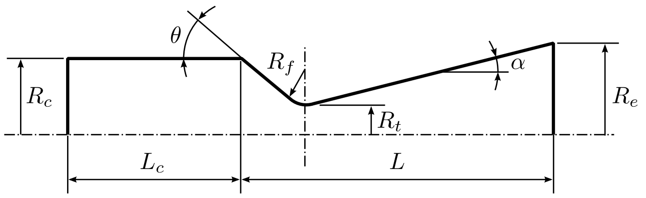

Figure 2.2: Basic contour of the combustion chamber and the conical nozzle.

are accelerated in the convergent part up to the speed of sound in the narrowest cross section of the throat. Downstream the nozzle in its divergent part the flow velocity exceeds the speed is of sound and the gases are further accelerated in the supersonic range. A conical shaped contour of the nozzle is used for this thruster, as depicted in Figure 2.2. This type allows easy manufacturing compared with a bell-shaped nozzle. Since the contour at the exit is not parallel to the axis of symmetry the flow velocity has an additional perpendicular component which does not contribute to the thrust. In relation to the ideal nozzle with an axis parallel flow the loss of gas momentum is expressed by the correction factor or the thrust efficiency $\lambda = \frac{1}{2}(1 + \cos\alpha)$. The geometrical parameters are chosen with respect to the approved values as given in [32]. The half angles of the convergent and divergent sections are $\theta = 30°$ and $\alpha = 15°$ respectively and the thrust efficiency yields $\lambda = \frac{1}{2}(1 + \cos 15) = 0.983$. The radius of the throat fillet R_f is chosen to be equal the radius R_t of the cross-sectional throat area A_t. Finally the expansion area ratio $\varepsilon = A_e/A_t$ yields the exit radius R_e in relation to the throat radius R_t.

2.4 Thruster Performance and Geometrical Dimensions

In addition to the equations stated above in section 1.2 some practical parameters are introduced in the following, which are used to specify the layout of the thruster geometry. Beginning with the dimensionless *thrust coefficient* factor C_f, which indicates the performance of the nozzle regarding the conversion of thermal energy into kinetic energy from the exhaust gases. It is defined by the relation

$$C_f = \frac{F}{p_c A_t} = \left[\frac{2\kappa^2}{\kappa - 1} \left(\frac{2}{\kappa + 1} \right)^{\frac{\kappa+1}{\kappa-1}} \left(1 - \frac{p_e}{p_c} \right)^{\frac{\kappa-1}{\kappa}} \right]^{\frac{1}{2}} + A_e(p_e - p_a). \tag{2.3}$$

The last term of this equation is obtained from (1.4) after rearranging. As second parameter the *characteristic velocity* c^* is introduced as

$$c^* = \frac{p_c A_t}{\dot{m}} = \left[\frac{\mathcal{M}}{\mathcal{R} T_c} \kappa \left(\frac{2}{\kappa + 1} \right)^{\frac{\kappa+1}{\kappa-1}} \right]^{-\frac{1}{2}}, \tag{2.4}$$

wherein the last term is obtained due to a substitution of $\dot{m}$ with equation (1.2). This factor is determined by the choice of the propellant combination. Since the value of $\kappa \geq 1$ remains in a close range for commonly used gases, c^* mainly depends on the combustion temperature T_c and the reciprocal of the molar mass $\mathcal{M}$. This term, with the dimension of velocity, characterises the combustion efficiency of a thruster.

In rocket engineering the *specific impulse*, defined as [1]

$$I_{sp} = \frac{F}{g_0 \dot{m}},$$

is a commonly used parameter to compare the exhaust velocities of rocket motors, because the unit is given in seconds.

Chemical equilibrium of the decomposition and combustion

The determination of the thermodynamic steady state of the propellants yields basic input parameters for the model of thermal loads to be applied inside the structural components of the thruster. The chemical equilibrium calculations of the decomposition and the combustion of the propellants were computed with the program CEA (Chemical Equilibrium with Applications) [44]. The computation is of the problem type *Rocket -rkt* with following options selected for the combustion chamber: *Infinite Area*, *Frozen at Throat*. For both chambers the internal pressure is assumed to be equal, thus any decrease of pressure between or inside the catalyst- and the combustion chamber is neglected. The two pressure levels considered are 10 bar at the nominal load and 12 bar at the design limit load.

---

[1] Standard acceleration of gravity $g_0 = 9.80665\text{ms}^{-2}$

Decomposition of hydrogen peroxide: In the initial storage condition hydrogen peroxide is present in liquid form at a temperature of 293 K. The properties of the gas mixture in the catalyst chamber after a complete decomposition of H_2O_2 are listed in Table 2.1.

Table 2.1: Thermodynamic and thermal transport properties of the decomposed hydrogen peroxide mixture with a nominal concentration of 87.5 %.

Pressure p_D	10	12	bar
Temperature T_D	960.3	960.3	K
Density ρ_D	2.7511	3.3013	$\mathrm{kgm^{-3}}$
Specific heat c_D	1.778	1.778	$\mathrm{kJkg^{-1}K^{-1}}$
κ_D	1.2705	1.2705	—
Molar mass	21.966	21.966	$\mathrm{kgkmol^{-1}}$
Dyn. viscosity η_D	4.153	4.153	$10^{-5}\ \mathrm{Nsm^{-2}}$
Therm. conductivity λ_D	0.0866	0.0866	$\mathrm{Wm^{-1}K^{-1}}$
Prandtl Number Pr_D	0.8525	0.8525	—

Combustion of Ethanol and Kerosene: The theoretical thrust performance was optimised with regard to maximum exhaust velocity, expressed by the specific impulse I_{sp}, by utilizing the *CEA* code [2]. The mixture ratios of oxidizer/fuel were predetermined for the nominal combustion pressure of 10 bar and an expansion area ratio $\varepsilon = 100$ to be 4.6 for ethanol and 7.25 for kerosene. With these parameters but a pressure of 12 bar the properties of the combustion gas mixture, computed with the *CEA* code, are listed in Table 2.2. By reviewing the data it is found that kerosene shows a slightly better theoretical perfomance due to the higher I_{sp} compared with that of ethanol. Thus only the property data of the fuel/oxidizer combination of kerosene and H_2O_2 is taken into account for present computations.

Geometrical dimensions

The thrust F is specified with 1 N for a nominal pressure of 10 bar in the combustion chamber. Both aria ratios for the nozzle exit and the combustion chamber are given

---

[2] written by S. Gordon and B. J. McBride, download from `http://www.grc.nasa.gov/WWW/CEAWeb/ceaHome.htm`

Table 2.2: Thermodynamic, thermal transport and thrust performance properties of the combustion gas mixture.

	Ethanol		Kerosene (Jet-A)		dimension
O/F ratio	4.6		7.25		—
Pressure p_c	10	12	10	12	bar
Temperature T_c	2548.18	2554.91	2635.77	2643.91	K
Density ρ_c	1.0101	1.2098	0.9838	1.1779	$\mathrm{kgm^{-3}}$
Specific heat c_c	4.105	4.016	4.397	4.292	$\mathrm{kJkg^{-1}K^{-1}}$
κ_c	1.137	1.138	1.133	1.1345	—
Molar mass	21.402	21.416	21.560	21.578	$\mathrm{kgkmol^{-1}}$
Dyn. viscosity η_c	9.284	9.305	9.497	9.522	$10^{-5}\ \mathrm{Nsm^{-2}}$
Therm. conductivity λ_c	0.311	0.312	0.319	0.320	$\mathrm{Wm^{-1}K^{-1}}$
Prandtl Number Pr_c	0.7599	0.7601	0.7488	0.7489	—
I_{sp}	308.444	308.709	312.981	313.318	s
C_f	1.8785	1.879	1.878	1.879	—
c^*	1562.0	1562.7	1585.0	1586.0	$\mathrm{ms^{-1}}$

as $\varepsilon = 100$ and $\varepsilon_c = 80$ respectively. Together with the value of the thrust coefficient C_f at 10 bar, taken for kerosene according to Table 2.2, and equation (2.3) the throat area can be computed

$$A_t = \frac{F}{p_c C_f} = \frac{1}{10 \cdot 10^5\ 1.8781} = 0.532 \cdot 10^{-6}\ \mathrm{m}^2, \tag{2.5}$$

from which the throat radius directly follows to be

$$R_t = \left(\frac{F}{p_c C_f \pi}\right)^{\frac{1}{2}} = \left(\frac{1}{10 \cdot 10^5\ 1.8781\ \pi}\right)^{\frac{1}{2}} = 4.117 \cdot 10^{-4}\ \mathrm{m}. \tag{2.6}$$

The throat radius represents a basic dimension whereof the remaining geometrical parameters can be easily obtained from

$$
\begin{aligned}
R_e &= R_t\sqrt{\varepsilon} = 4.117\cdot 10^{-4}\sqrt{100} = 4.117\cdot 10^{-3}\ \text{m},\\
R_c &= R_t\sqrt{\varepsilon_c} = 4.117\cdot 10^{-4}\sqrt{80} = 3.682\cdot 10^{-3}\ \text{m},\\
L_c &= \left(\frac{1}{\varepsilon_c^2}\right)\left[L^* - \frac{R_t}{3\tan\theta}(\varepsilon_c^{\left(\frac{3}{2}\right)} - 1)\right] =\\
&= \frac{1}{80}\left[1.780 - \frac{4.117\cdot 10^{-4}}{3\tan(30)}(80^{\left(\frac{3}{2}\right)} - 1)\right] = 2.013\cdot 10^{-2}\ \text{m},\\
R_f &= R_t = 4.117\cdot 10^{-4}\ \text{m}.
\end{aligned}
$$

A plot of the nozzle contour is illustrated in Figure 2.3. Due to the similarity of the thrust coefficients and for practical reasons the geometrical dimensions are chosen to be the same for both fuel configurations. The resulting flow parameters of the CEA code at the throat position can be used to determine the mass flow rate. Putting the values for the free stream velocity $u_t = 1042\ \text{ms}^{-1}$, which is equal to the speed of sound, the flow density $\rho_t = 0.6055\ \text{kgm}^{-3}$ and the throat area from above into equation (1.2) this yields

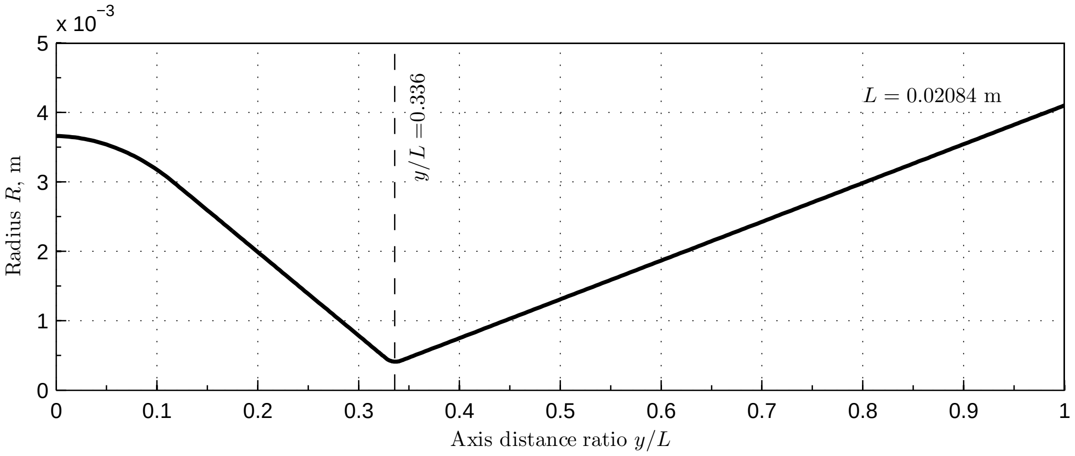

Figure 2.3: Shape of the conical nozzle, radius plotted versus relative length coordinate.

$$\dot{m} = A_t u_t \rho_t = 0.532\cdot 10^{-6}\cdot 1042\cdot 0.6055 = 0.336\cdot 10^{-3}\ \text{kgs}^{-1}. \tag{2.7}$$

3 Materials

The topic of high-temperature materials is an extensive field in present material research, with the main objective towards increasing service temperature levels. The utilization of these materials is cruzial for the realisation and efficiency of high temperature applications. The choice of a material which fulfills these specific, often contrary demands, mostly is a compromise between different material properties like:

- Maximum service temperature
- Physical and mechanical properties as functions of temperature
- Creep behavior and time-to-failure (TTF)
- Low cycle fatigue (LCF) and high cycle fatigue (HCF) characteristics
- Superior resistance against corrosion at elevated temperatures

3.1 Thrust Chamber Materials

A rather difficult question to answer is the finding of proper materials when focusing on the thrust chamber, consisting of the combustion chamber and the nozzle extension, as the critical high-temperature part of the present thruster. As a consequence of the applied cooling principle through radiation the resulting wall temperatures are higher compared with those of actively cooled walls. Regarding the miniaturised size of the thruster further aspects have to be drawn onto manufacturing issues like shaping and joining of the parts. In the following two metals, the platinum-rhodium alloys and Iridium, currently used for radiatively cooled thrust chambers are described more in detail. These materials are then considered in the combined FEM analysis.

3.1.1 Platinum-Rhodium Alloy

Platinum which belongs to the platinum group metals (PGM) is regarded as one of the most inert metals against corrosion and oxidation at elevated temperatures. Pure platinum is a very ductile face-centered cubic (f.c.c.) material that has no ductile-to-brittle transition temperature. For the structural use in high temperature applications, platinum is most commonly alloyed with Rhodium or Iridium to improve the mechanical strength by solid solution hardening. Primary application fields of these alloys are found e.g. in the glass and fibre glass production, laboratory equipment, diverse sensors, and elektrodes. Especially in European space progamms Pt-Rh alloys, as the successors of the nickel based alloy Nimonic 90, currently are the material of choice for small chemical satellite thrusters [28], allowing operational temperatures up to 1600°C. In connection with an exceptionally good oxidation resistance and mechanical behaviour this alloy provides enhanced fuel efficiency and fail-safe operation. Therefore Pt-10%Rh DPH is the first material candidate focused on here, which is additionally strengthened by dispersion hardening (DPH) with zirconium and or yttrium oxide. Having the adequate size ($< 1\mu$m) and spacial distance ($< 10\mu$m), these finely dispersed oxide particles effectively hamper the movement of dislocations as well as the excessive grain coarsening that takes place at high temperature levels for long time periodes [22]. Figure 3.1 clearly shows the retarded microstructure of the dispersion harded material (b), in relation to the drastic growth of the grain boundaries approaching to the thickness of the probe which consists of the conventional Pt-10%Rh alloy (a). Grain boundaries of this extent reduce the mechanical strength

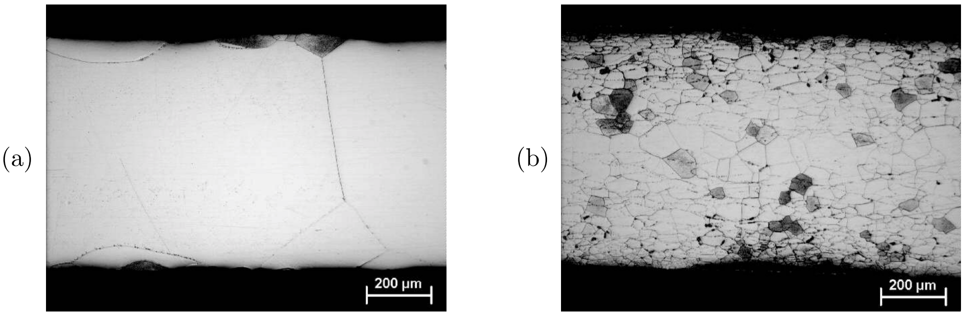

Figure 3.1: Microstructures of the platinum base materials (a) conventional Pt-10%Rh alloy and (b) Pt-10%Rh DPH after a longterm exposure of 10,000 h at temperatures over 1200°C, from [22].

and cause anisotropic behaviour, another reason why the DPH alloy shows better mechanical behaviour under such service conditions than conventional Pt-Rh alloys. Some physical properties to be listed in the following are:
density $\rho = 19800$ kgm^{-3}, melting point $T_m = 2123$ K (both values come from [17]), specific heat $C = 131.2$ Jkg^{-1}K^{-1} (for pure platinum at 273.15 K, from [3]) and data of the thermal conductivity λ versus temperature is given below (linearly interpolated, data originate from [57]).

T, (K) :	293.15	673.15	1073.15	1273.15	1473.15	1673.15	1873.15
λ, (Wm^{-1}K^{-1}) :	74.4	73.7	79.2	85.1	88.7	89.3	87.9

The mechanical properties at discrete temperature points and values of the coefficient of thermal expansion (CTE), as input for the structural FEM analysis, are listed in Table 3.1. Stress-strain diagrams, as shown in Figure 3.2, at different test temperatures beginning from 1200°C up to 1600°C suggest to characterise the material as perfect plastic one.
The strength benefit drawn from the introduction of oxide dispersoids into the Pt-matrix is emphasized in Figure 3.3, where creep-rupture curves of selected platinum based alloys form reference [23] are shown. Here the Pt-30%Ir alloy is the only material that reaches higher stress levels at specific times to failure than the DPH material. In the following sections this alloy is denominated as 'Pt10Rh'.

3.1.2 Iridium

Iridium, a member of the platinum group metals, is considered as one of the chemically most stable metals. Examples of its structural use are for instance crucibles to melt and grow single crystals of metal oxides for solid state lasers and semiconductors [30], or capsules enclosing the radioactive heat sources in radioisotope thermoelectric generators onboard of spacecrafts [36]. In an effort to improve the efficiency of thrusters in the range of 22 up to 440 N, research activities were conducted by NASA about chamber materials that could sustain higher service temperatures as the well established niobium alloy C103, which is limited to 1643 K due to the protective silica

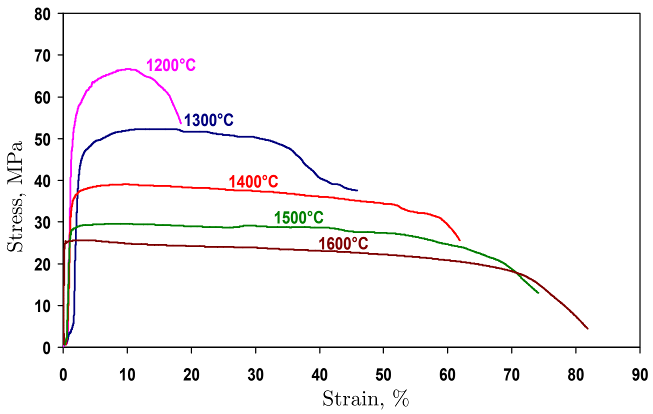

Figure 3.2: Stress-strain curves at high temperatures of the material Pt-10%Rh DPH, from [21].

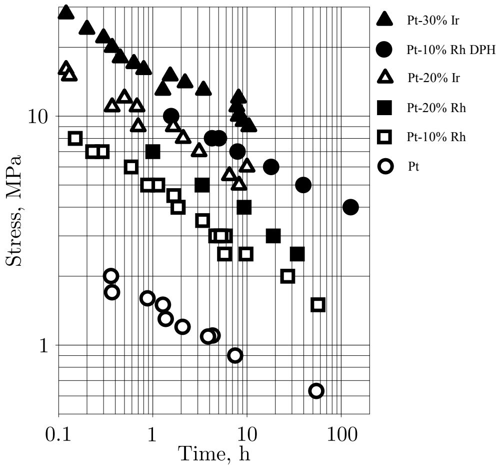

Figure 3.3: Creep-rupture curves of selected platinum based alloys at a temperature of 1600°C, from [23].

coating [37]. In this developement the chamber walls were made of rhenium, which has a melting point of around 3448 K, coated with an protective iridium layer against oxidation, allowing wall temperatures between 2273 K and 2573 K for more than 11 hours of operation accumulated during the 44 test firings [38].

Although Ir has a f.c.c. crystal structure, which generally indicates a material that possesses a certain amount of ductility, it tends to fail by cleavage under tensile loading at room temperature. Large diffusion zones at the grain boundaries, containing elements like carbon, oxygen and hydrogen, obstruct the transfer of dislocations which agglomerate inside the grain (high work hardening rate) and secondly the weak grain boundary cohesion are likely to be the reasons for the dominating brittle-mixed mode fracture (intergranular and transgranular cracksurface) [56]. Tensile test data, given in reference [43], show a significant ductility increase within the interval of 600 K up to 1200 K. In conjunction with a sharp drop of the ultimate tensile stress whilst yield stress values remain nearly constant the work hardening rate was suggested to be strongly decreasing in this temperature range and the ductile-brittle transition temperature (DBTT) was stated to be around 900 K. It was also reported that the shift of DBTT is directly proportional to the strain rate. As a consequence, the conventional deformation processing and shaping of iridium is restricted to a large extent, e.g.

Table 3.1: Mechanical properties of Pt-10%Rh DPH.

Temperature (K)	Elastic modulus [a] (GPa)	Poisson ratio [b] –	CTE [c] (10^{-6}K^{-1})	$R_{p0.2}$ [d] (MPa)	R_m [d] (MPa)	A [d] (%)
293	212.6	0.363	10.0	243.0	362	30
673	197.9	0.372	10.5	–	–	–
1073	179.2	0.374	11.0	–	–	–
1273	145.9	0.38	11.5	–	–	–
1473	136.3	–	13.5	47.2	67.4	18.4
1673	126.7	–	16.0	33.2	39.3	59.2
1873	117.1	–	16.0	21.4	23.0	82.9

a) Elastic modulus, values at temperatures below 1273 K taken from [39], the remaining values originate from [20].
b) Poisson ratio values, taken from [39].
c) Thermal expansion values originate from [16].
d) Data at 298 K is taken from [17], data at 1273 K and above are determined from [21].

regarding initial working temperatures for ingots to be as high as 2075 K [45] or the avoidance of immoderately high tensile stresses. Nevertheless processes like extrusion forming of bars and rolling into thin sheet are practicable. The miniaturised dimensions of the present thruster would favour manufacturing processes able to built near net-shape structures like electrodeposition or chemical vapour deposition (CVD). A molybdenum mandrel, profiled with the inner geometry, is hereby coated with subsequent layers of iridium till reaching the desired thickness. Finally the free standing structure is obtained after a complete removal of the mandrel through dissolution with nitric acid [51]. Another possibility could be the electrical discharge machining (EDM) of a prefabricated iridium rod. Iridium can be joined by welding with the common gas tungsten arc (GTA) technique, but more preverable are electron beam welding (EBW) or laser welding because of their higher energy concentration in a small fusion zone, resulting in a fine microstructure after rapid solidification. Joining iridium to nickel based alloys with laser welding is already practiced to fabricate spark plugs.

The physical properties of interest are listed in the following:
density $\rho = 22650$ kgm^{-3} ([17]), melting point $T_m = 2720.15$ K ([7]), specific heat $C = 128.4$ Jkg^{-1}K^{-1} (at 273.15 K, from [3]), and the thermal conductivity λ versus

Table 3.2: Mechanical properties of iridium.

Temperature (K)	Elastic modulus a) (GPa)	Poisson ratio b) –	CTE c) (10^{-6}K^{-1})	$R_{p0.2}$ d) (MPa)	R_m d) (MPa)	A d) (%)
298	525.5	0.254	6.194	118.4	395.0	9.6
773	472.7	0.265	7.585	108.3	455.5	19.5
1073	439.9	0.275	8.626	103.4	343.5	28.8
1373	406.1	0.279	9.793	92.8	224.7	37.9
1873	350.6	–	11.086	43.9	91.7	55.7
2173	317.0	–	13.521	19.3	41.2	72.1

a) Elastic modulus values originate from [39], data at 1873 K and 2173 K are linearly extrapolated.
b) Poisson ratio values, taken from [39].
c) CTE values calculated according to $6.13 \cdot 10^{-6} + 2.56 \cdot 10^{-9} t + 0.7 \cdot 10^{-12} t^2$, t in ℃, from [50].
d) Data at 298 K up to 1373 K taken from batch S–65 in [36], data at 1873 K and 2173 K are determined from [21].

Table 3.3: Creep-rupture strength values of iridium at high temperatures, from [24].

TTF	Creep-rupture strength, (MPa)				
(h)	1923 K	2073 K	2273 K	2473 K	2573 K
1	31.8	24.4	14.1	7.1	5.4
10	27.7	18.4	8.9	4.4	3.3
100	15.6	11.0	4.6	2.7	2.0
1000	8.8	7.0	1.5	–	–
10,000	5.0	4.4	–	–	–

temperature is given below (data originate from [57]).

T, (K)	: 273	600	800	1000	1200	1400	1600	1800	2000
λ, (Wm^{-1}K^{-1})	: 148	136	130	125	121	117	110	106	103

Elastic properties and tensile test data, as well as the CTE-values at selected temperature levels are given in Table 3.2. The durability of iridium parts under the influence of tensile stresses can be estimated with the creep-rupture strength values that are listed in Table 3.3 at specified temperature levels and time-to-failure values.

3.2 Material of the Decomposition Chamber and Remaining Parts

Nickel based high temperature alloys are the potential materials candidates for the remaining parts of the model. From the large variety of this material class the alloy NiCr25FeAlY (material number EN-DIN 2.4633, known under the commercial designations Nicrofer6025 HT or alloy 602 CA) was picked for the simulation. The chemical composition of this Ni based alloy, according to [4], typically consists of 25 wt% Cr, 9.5 wt% Fe, 2.3 wt% Al and 0.18 wt% C, complemented by the microalloying elements Ti, Y, and Zr. Beneath the solid solution strengthening the high carbon content allows the formation of carbide particles in a finely distributed state, due to titanium and zirconium, which preferably precipitate along the grain boundaries. This effectively reduces the creep deformation due to boundary diffusion leading to a further improvement of the high temperature strength and the time-to-failure. Protective layers against oxidation are formed by chromia Cr_2O_3 and the self healing alumina Al_2O_3, latter one is laying between metal and the chromium oxide [14]. Benefits from the alumina sub-layer are drawn because of the high thermodynamic stability above 1223 K, where chromium oxide already begins to form the volatile chromium trioxide CrO_3 and secondly it is built up at low oxygen partial pressures thus preventing the carburisation of the base material in the presence of carbon rich gas atmospheres. The maximum service temperature of this alloy is limited to 1473 K [46].

Some of the physical properties according to the datasheet [2] are given in the following:
density $\rho = 7900$ kgm^{-3}, melting range $1643.15 - 1673.15$ K, data of the specific heat C and the thermal conductivity λ versus temperature is listed below.

T, (K)	: 293	573	773	973	1173	1373
λ, (Wm^{-1}K^{-1})	: 11.3	16.0	19.2	22.2	26.1	29.3
C, (Jkg^{-1}K^{-1})	: 450	525	580	630	690	740

Values of the stress amplitude leading to fatigue failure after 10^6 cycles are compared with those of the creep-rupture strength in Figure 3.4, both at the same temperature

Table 3.4: Mechanical property data[a)] versus temperature of the NiCr25FeAlY alloy.

Temperature (K)	Elastic modulus (GPa)	Poisson ratio –	CTE ($10^{-6}K^{-1}$)	$R_{p0.2}$ (MPa)	R_m (MPa)	A_5 (%)
293	215	0.3	11.9	270	675	42
573	197	–	14.0	200	600	45
773	189	–	14.7	180	560	44
973	169	–	15.7	170	420	34
1173	137	–	17.1	120	215	85
1373	102	–	17.6	50	80	96

a) The property data, except the Poisson ratio, is stated according to reference [2].

of 1373 K. Here the fatigue strength, which declines by a reduction of the oscillation frequency or an increase of the material temperature, is significantly higher than values of the static creep-rupture strength plotted at the equivalent frequencies of 0.28 and 2.78 Hz. The mechanical properties of the NiCr25FeAlY alloy together with the CTE-values are found in Table 3.4. The value of the Poisson ratio equal 0.3 well agrees with those from the similar alloy 690 over the service temperature range.

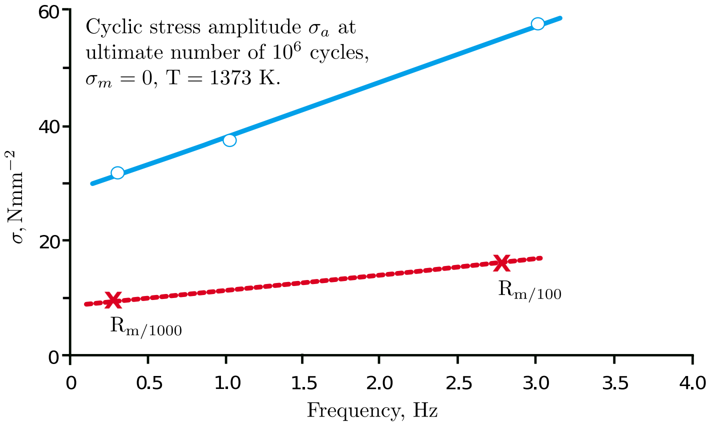

Figure 3.4: Comparison of the stress amplitudes at 0.3, 1, and 3 Hz in fatigue tests (blue circles) with the creep-rupture strength values for TTF of 100 h and 1000 h at 1373 K (red crosses), of the NiCr25FeAlY alloy according to [4].

3.3 Material implementation in FEM

Whenever it was applicable the material data, as given in the preceding sections, was implemented in form of a temperature dependent data table. If there are more than a single data point available the ANSYS code linearly interpolates the property data versus temperature, otherwise the data is kept constant. The mechanical material behaviour is idealised as perfect plasticity post yield, thus the bilinear isotropic material option (BISO) with a tangent modulus equal zero was chosen. Due to the temperature dependence of both the elastic modulus $E(T)$ and the yield strength $R_{p0.2}(T)$ this nonlinear material model also varies with temperature.

4 Modelling of the Thruster

4.1 Geometric Model

The geometry and layout of the FEM model is based up on a preliminary design study for this type of thruster. This design study resulted in a first draft of the thruster as depicted in Figure 4.1 (b). An exploded view of the principal components is shown in Figure 4.1 (a). The thermal barrier cylinder, with part number (7), is placed between the mounting plate (which is not included here) and the propellant manifold (4) to reduce thermal soakback into the satellite structure. The major draft guidelines were set in advance by the thrust chamber geometry and dimensions as described in Section 2.4, and the assignment of a L-shaped configuration where the decomposition chamber is perpendicular connected to the injector manifold.

Another aspect that has to be fullfilled by the design was drawn from the criteria, that parts of the thruster should be integrally joined to each other by welding. To reduce the number of parts in the FEM model the single components Cap and Decomposition chamber as well as the Insert ring, Fuel-needle and Propellant manifold were integrally merged into two seperate components. Figure 4.2 shows the drawing of the thruster model including the main dimensions, where the front view represents a cut through the plane of symmetry. The dimension values differ slightly from those given at the end of Section 2.4 due to numerical rounding for technical reasons and meaningful tolerances. Creation and modification of model geometry was done with the CAD software Solid Works. The geometry data, present in the Initial Graphics Exchange Specification (IGES) format, is being read in by ANSYS during the input process routine to build the geometrical FEM model. The total mass of the thruster, by using the platinum alloy as thrust chamber material, is 18.6 g whereof 6.6 g are accounted for the thrust chamber. Due to the higher density of Iridium the total

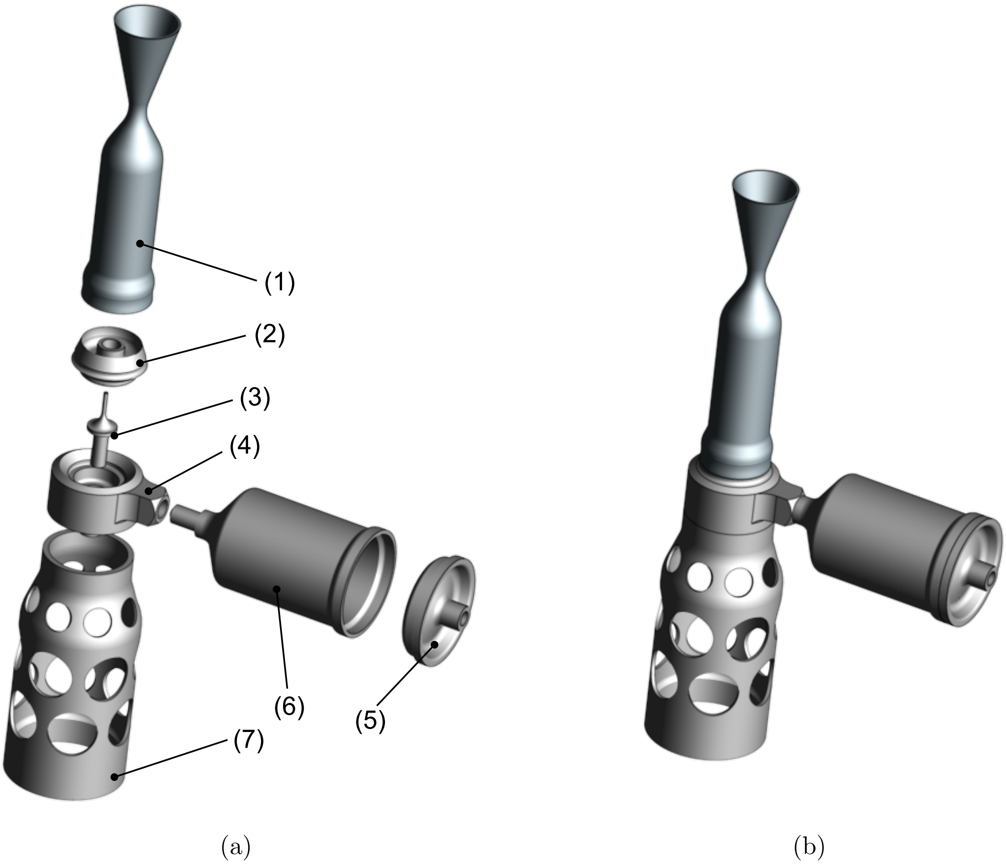

Figure 4.1: (a) Exploded view of the structural components: (1) Thrust chamber, (2) Insert ring with injector, (3) Fuel-needle, (4) Propellant manifold, (5) Cap, (6) Decomposition chamber, (7) Thermal barrier cylinder. (b) Thruster in assembly configuration.

mass of this configuration is 23.8 g, in this case the thrust chamber adds 7.5 g to the thruster mass.

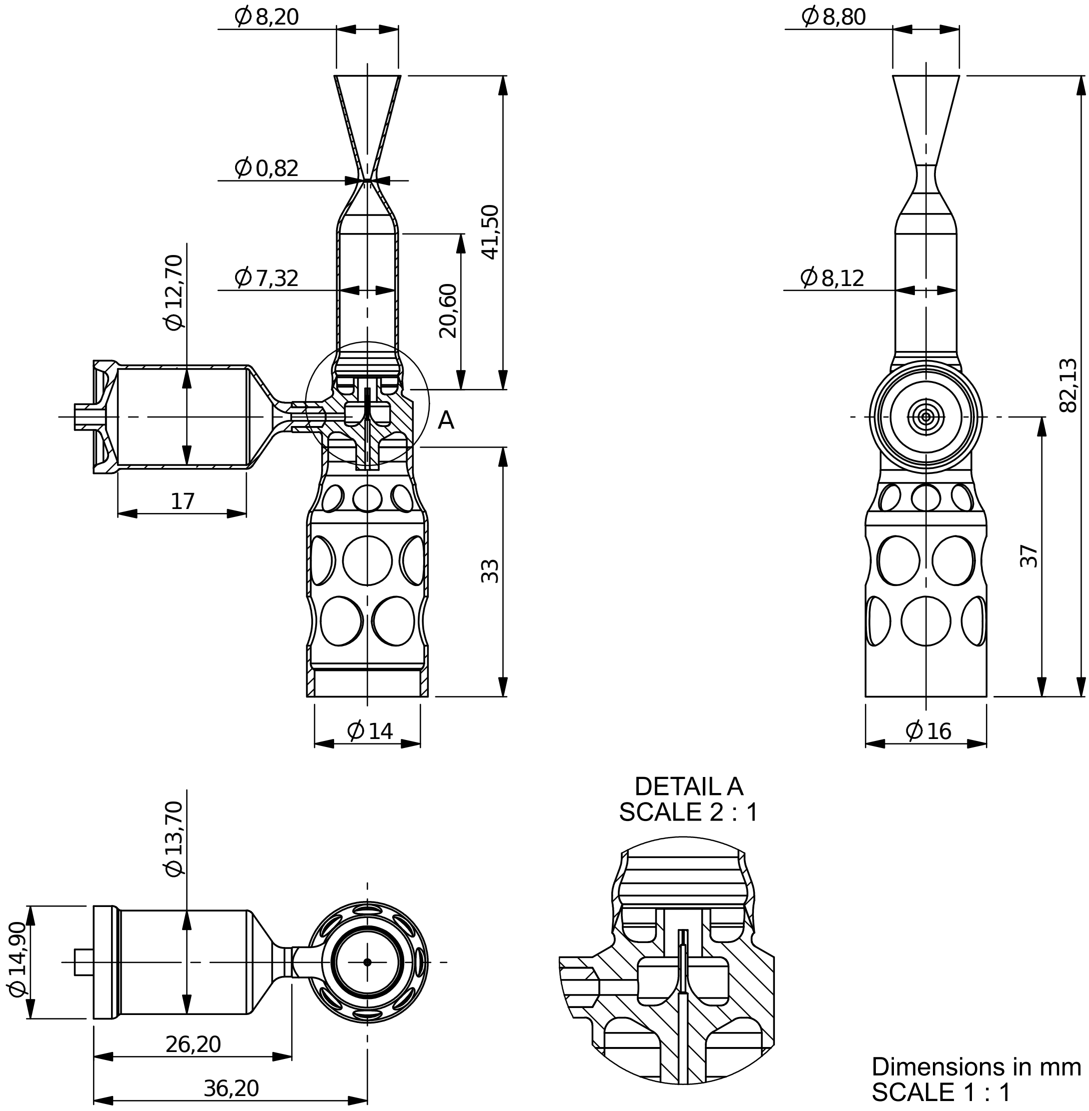
Ø8,20
Ø0,82
Ø7,32
Ø12,70
41,50
20,60
A
17
33
Ø14
Ø8,80
Ø8,12
82,13
37
Ø16
Ø13,70
Ø14,90
26,20
36,20
DETAIL A
SCALE 2 : 1
Dimensions in mm
SCALE 1 : 1

Figure 4.2: Drawing of the thruster in first angle projection with a section view along the symmetry plane, as depicted in the front view and in Detail A.

3D-Model

The volumetric FEM model is shown in Figure 4.3 (a). This is the half-section of the thruster model, gained by utilizing the symmetry along the x-y plane, which allows a reduction of the number of elements to build the mesh. After the geometry data set is imported the generated volumes are glued together, so that they share the same areas at their interfaces. With only one area defined per interface the nodes to be located on are also shared by adjacent volumes. Hence the coupling of degrees of freedom (DOF's) between the two separate nodal sets after generating the mesh is being omitted. The coloured faces indicate parts of the cross section that define the two dimensional model. Here the red-coloured area marks the thrust chamber made of either platinum based Pt-10% Rh DPH or iridium,whereas the blue-coloured section is linked to the nickel-based alloy. The purposes of this model are to simulate the thermal transient and stationary solution combined with structural analysis.

2D-Model

The second model is of two dimensional type to be axially symmetric along the y-axis. The planar contour, depicted in Figure 4.3 (b), is derived from the cross sectional area of the volumetric model that belongs to the x-y half-plane in positive x-direction. In the upper section of the thermal barrier cylinder of the 3D-model there are eight circumferential drillings of radius $r_b = 1.6$ mm, that reduce the cross sectional area and consequently the heat flow (assumed the temperature gradient does not change significantly). Hence a constriction in the wall thickness is introduced in the 2D-model to account for this cross sectional reduction with

$$t_b = t\left[1 - \frac{8}{\pi}\arctan\left(\frac{r_b}{r_m}\right)\right] = 0.4\left[1 - \frac{8}{\pi}\arctan\left(\frac{1.6}{6.8}\right)\right] = 0.165 \text{ mm}, \tag{4.1}$$

where t is the original wall thickness and r_m stands for the mean circumferential radius. Although the actual thruster geometry is far from this plain symmetry the two dimensional model can be of great value for a rapid estimation about how changing load parameters and geometry adaptations have an effect on the temperature and stress fields.

Bi-material joint interface

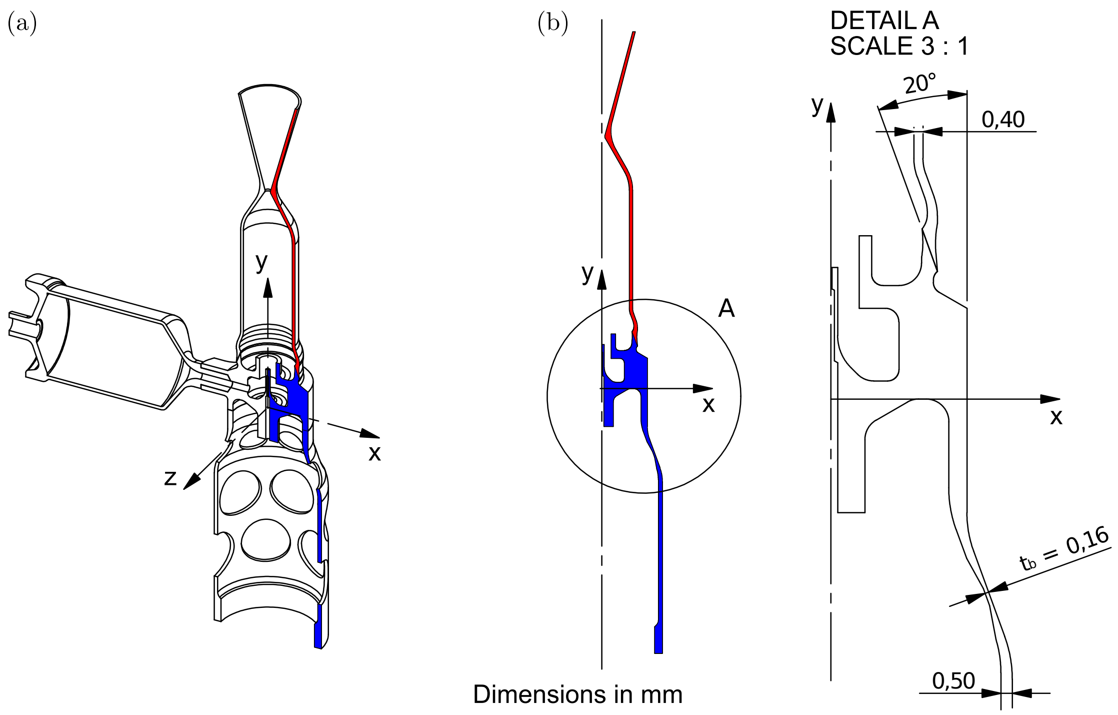

Figure 4.3: (a) Three dimensional solid body model; (b) two dimensional model, axially symmetric along the y-axis.

The idealized interface of the bi-material joint to connect the thrust chamber (made of iridium or platinum) with the injector manifold (made of NiCr25FeAlY) is depicted in Figure 4.4. As a consequence of joining two materials having different mechanical parameters, care has to be taken about the geometric outline at the junctions of interface and the outside free surface to avoid unbound values of the stress fields at these points, marked with A and B in Fig. 4.4. Examples within classic elasticity theory that yield solutions with existing stress singularities are discussed in detail in review [48] and [49]. These occur e.g. at loactions with concentrated loads as well as at discontinuities in boundary conditions with regard to geometry, surface loads, and at distinct interfaces of different materials. In terms of polar coordinates r and θ with the origin in the junction point of the interface and the free surface, the stress field for a bi-material configuration can be expressed according to reference [15]

$$\sigma_{ij} = K r^{-\gamma} F_{ij}(\theta). \tag{4.2}$$

Here K is a stress intensity factor, γ is the singularity exponent expressing the order

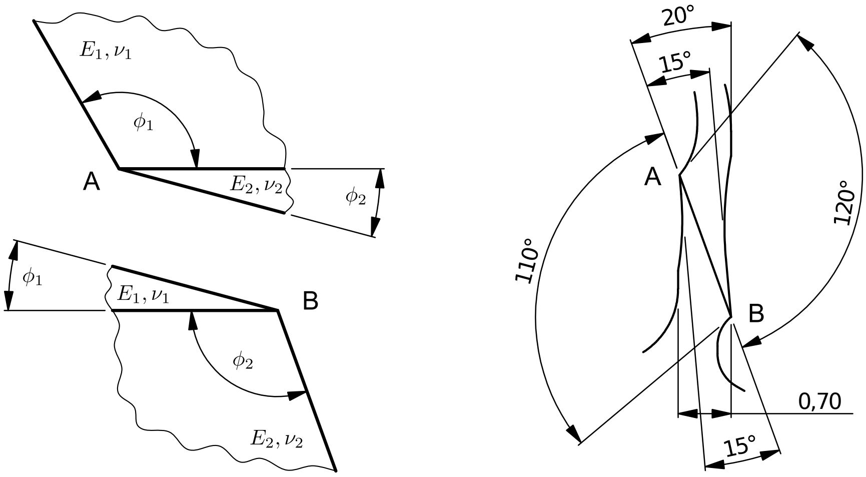

Figure 4.4: Bi-material wedges with the upper (point A) and lower (point B) interface/free surface edge (Left); Detail of the idealized welded joint geometry (Right).

of the power singularity, and finally the term $F_{ij}(\theta)$ which depends on θ. Due to the resulting singularity within close proximity to the junction point the stress fields here are physically not meaningful in their value, but they qualitatively indicate higher stress intensities in this region. It follows that the occurence of the singularitiy here does not depend on the magnitude of the far stress field present. Hence the introduction of plasticity theory would erroneously predict plastic strains at these points, therefore it is not suited to correct this deficiency. Combinations of the vertex angles ϕ_1 and ϕ_2, that ensure the absence of singularities in any point of the bi-material interface for specific boundary conditions can be drawn from design charts, as presented in [11] for the constituents steel and aluminum. For the present material combination the same strategy was pursued. Lee and Barber have developed the open source program [1] *Wedge Solver* for automatically solving the asymptotic two dimensional wedge problem. A manual is published in [42]. This tool was used to test the bi-material wedges of Fig. 4.4, with the vertex angle combinations for point A $\{\phi_1 = 120°,\ \phi_2 = 15°\}$ and point B $\{\phi_1 = 15°,\ \phi_2 = 110°\}$. Properties for material 1 (iridium or platinum) and material 2 (NiCr25FeAlY) were input at 293 K and 1373 K. The plain strain state was chosen with boundary conditions at the free faces to be stress free (${}^{i}\sigma_{\theta\theta} = 0, {}^{i}\sigma_{r\theta} = 0$, with the material index $i = 1, 2$) and perfectly bonded at the interface ($^1\sigma_{\theta\theta} = {}^2\sigma_{\theta\theta}, {}^1\sigma_{r\theta} = {}^2\sigma_{r\theta}, {}^1u_r = {}^2u_r, {}^1u_\theta = {}^2u_\theta$). In all cases the eigenvalues λ from the characteristic equation were real and identical to $\lambda = 1$. Consequently $\gamma = 1 - \lambda = 0$ and so no singularities are found to be present.

---

[1] It can be downloaded from
`http://www-personal.umich.edu/~jbarber/asymptotics/intro.html`

4.2 Thermal Loads

In a chemical rocket motors the combustion chamber together with the nozzle throat are those parts subjected to the highest thermal loads. In case of long term or steady-state operation, the heat flux transferred into the chamber walls requires cooling to keep the temperature of components below the limits of structural weakening. Some applied cooling techniques comprise [9]: *regenerative cooling*, *radiation cooling*, and *film cooling*. Most main engines from launch vehicles, burning liquid (cryogenic) propellants with a high energy density at high chamber pressures, use a combination of regenerative and film cooling, the latter one is covered in detailed in [6]. Miniaturised hot gas thrusters, as the present one, are commonly cooled only by radiation due to size and simplicity of the system. The heat transferred in the thrust chamber from the hot gas-side to the wall by conduction is negligible and for small chambers with low pressures even the contribution of radiation effects to the overall amount of heat transfer is small [10] and therefore also neglected. Through this assumptions the heat transfer mechanisms applied to the model are reduced to convection inside and radiation outside the thrust chamber.

4.2.1 Convective Heat Transfer Inside the Nozzle and Combustion Chamber

The heat flux induced by convective heat transfer between a conveying medium and a contact surface is defined by the expression

$$\dot{q} = \frac{\dot{Q}}{A} = \alpha(T_{medium} - T_{surface}). \tag{4.3}$$

This shows, that $\dot{q}$ depends on the heat-transfer coefficient α and a specific temperature difference between the medium and the contact surface. In case of a convergent-divergent nozzle a general analytic solution to determine the value of α has yet not been found. It has been shown by experiments that the heat-transfer coefficient varies with the axial position, reaching a maximum value close to the throat in the convergent part of the nozzle, as described e.g. in [41] and [27]. In the following values referred to as *local* are related to the distance on the y-axis of symmetry, counted from the nozzle entry, as the main position variable.

Bartz equation

Based on the empirically found power law relation $\alpha_g \sim (\rho v)^m$ for the heat-transfer coefficient between the hot-gas and the chamber wall, Bartz has stated the following expression in [8]

$$\alpha_g = \left[\frac{0.026}{D_t}\left(\frac{\eta^{0.2} c_p}{\mathrm{Pr}_c^{0.6}}\right)_0 \left(\frac{p_c}{c^*}\right)^{0.8} \left(\frac{D_t}{R}\right)^{0.1}\right] \left(\frac{A_t}{A}\right)^{0.9} \sigma. \tag{4.4}$$

The correction factor σ accounting for property variations across the turbulent boundary layer is given as

$$\sigma = \left[0.5\frac{T_w}{T_0}\left(1 + \frac{\kappa - 1}{2} M^2 + 0.5\right)\right]^{\left(\frac{\omega}{5} - 0.8\right)} \left[1 + 1 + \frac{\kappa - 1}{2} M^2\right]^{-\frac{\omega}{5}}. \tag{4.5}$$

The variables in the terms above are the local gas-side wall temperature T_w, Prandtl number Pr_c, the dynamic viscosity η, specific heat at constant pressure c_p, ratio of specific heats κ, chamber pressure p_c, the characteristic velocity c^*, and the local cross-sectional area A. The subscripts 0 and t indicate the gas properties at the stagnation condition and the local condition at the nozzle throat, respectively. The temperature exponent of viscosity is chosen to be $\omega = 0.6$, according to [8]. Gas property values at the stagnation condition are given in Table 2.2. The Mach number M is implicitly determined by the following relation assuming a one-dimensional isentropic gas flow through the nozzle

$$\frac{R_t^2}{R^2} = \frac{A_t}{A} = \frac{\rho v}{\rho_t v_t} = M\left[\frac{(\kappa + 1)}{2 + (\kappa - 1) M^2}\right]^{\frac{\kappa+1}{2(\kappa-1)}}. \tag{4.6}$$

The wall heat flux $\dot{q}_w$ is then computed by

$$\dot{q}_w = \alpha_g (T_{aw} - T_w), \tag{4.7}$$

where T_{aw} is the adiabatic wall temperature which is defined by

$$T_{aw} = T\left(1 + r\frac{(\kappa - 1)}{2}M^2\right). \tag{4.8}$$

In above expression the free stream temperature is obtained from the isentropic gas flow relation

$$T = T_0\left(1 + \frac{(\kappa - 1)}{2}M^2\right)^{-1}. \tag{4.9}$$

According to [35] the recovery factor is chosen as $r = \mathrm{Pr}_c^{1/3}$, yielding values of 0.908 up to 0.913 for the present Prandtl numbers from Table 2.2. These are in fair agreement with $r = 0.89$ chosen by Bartz, although in reference [13] a value of 0.8 is already regarded as conservative approach for the recovery factor.
The curves of both temperatures T and T_{aw} along the nozzle axis are depicted in Figure 4.5 for the nominal pressure of 10 bar and the design limit pressure of 12 bar. Figure 4.6 shows the heat-transfer coefficient, determined by equation (4.4), plotted over the nozzle axis. The curves have a strong positive gradient at the end of the converging part of the nozzle having a maximum at the throat, followed by a steep decrease at the beginning of the divergent part. In the throat region the wall temperature has a strong influence on the magnitude of α_g.

Turbulent boundary-layer analysis

As mentioned in [35], a modified theory was developed to estimate the heat-transfer coefficient between hot gases streaming through a De-Laval nozzle and the nozzle wall. It was shown by Back et al. in [27] that values of α_g computed with this version better agree with experimentally found results compared to values yielding from equation 4.4, especially in the case of lower stagnation pressures p_0.

A detailed description of the derivation and applied assumtions leading to the turbulent boundary-layer analysis is presented in reference [47]. In the following a set of equations from this theory is given. These expressions were programmed as APDL subroutines which allows the computation of the local heat-transfer coefficients during the runtime of an ANSYS simulation.

Beginning with the determination of the local Mach number M equation (4.6) is solved with regula falsi method regarding the conditions of subsonic- in the converging and

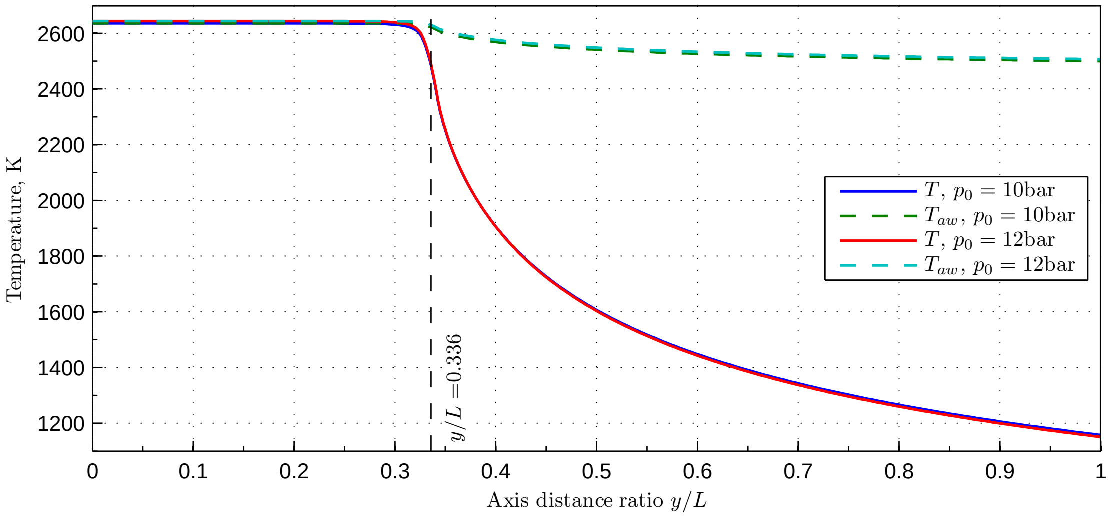

Figure 4.5: Profile of the free stream temperature T and the adiabatic wall temperature T_{aw} plotted over the axis distance at static pressures of 10 and 12 bar.

transsonic-flow in the diverging parts of the nozzle. At this point equations (4.9), (4.8), and by assuming one-dimensional isentropic gas flow relation the flow density according to

$$\rho v = p_0 \kappa M \left(c_p T_0 (\kappa - 1)\right)^{-\frac{1}{2}} \left(1 + \frac{\kappa - 1}{2} M^2\right)^{-\frac{\kappa+1}{2(\kappa-1)}}, \tag{4.10}$$

are known at each postion.

The force equilibrium for the potential mass flow in the boundary layer yields a differential equation that describes the momentum thickness θ of the boundary layer along the nozzle-axis, denoted as *Momentum Equation*, which is given to be

$$\frac{\mathrm{d}\theta}{\mathrm{d}y} = \frac{C_f}{2} \left[1 + \left(\frac{\mathrm{d}R}{\mathrm{d}y}\right)^2\right]^{\frac{1}{2}} - \theta \left[\frac{2 - M^2 + \frac{\delta^*}{\theta}}{M\left(1 + \frac{\kappa - 1}{2} M^2\right)} \frac{\mathrm{d}M}{\mathrm{d}y} + \frac{1}{R} \frac{\mathrm{d}R}{\mathrm{d}y}\right]. \tag{4.11}$$

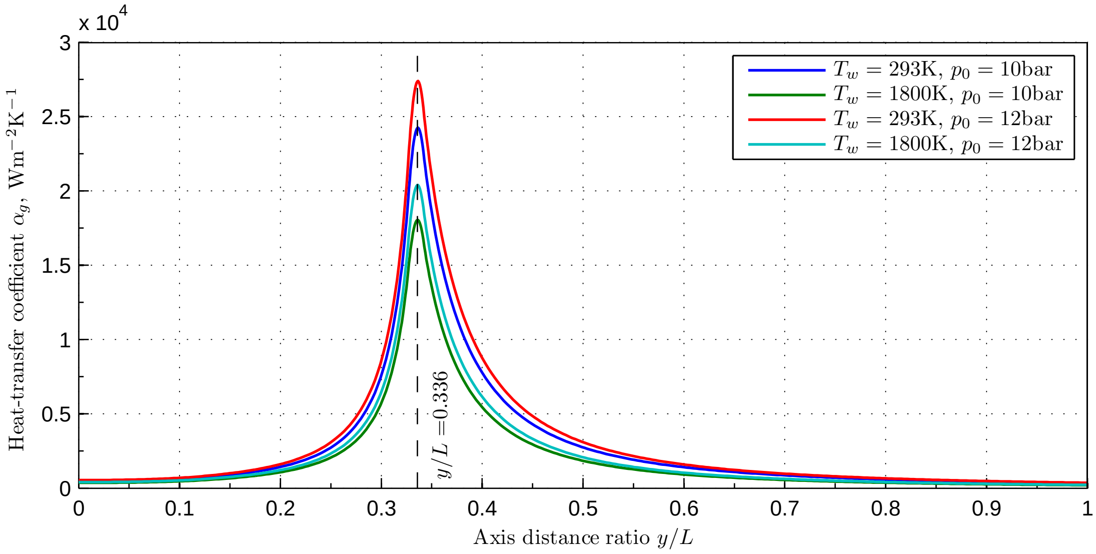

Figure 4.6: Heat-transfer coefficient α_g according to equation (4.4), plotted over the axis distance, at static pressures of 10 and 12 bar and different, constant wall temperatures of 293 K and 1500 K.

The following so called *Energy Equation*, specified to be

$$\frac{\mathrm{d}\Phi}{\mathrm{d}y} = \mathrm{St}\left(\frac{T_{aw}-T_w}{T_0-T_w}\right)\left[1+\left(\frac{\mathrm{d}R}{\mathrm{d}y}\right)^2\right]^{\frac{1}{2}} - \Phi\left[\frac{1-M^2}{M\left(1+\frac{\kappa-1}{2}M^2\right)}\frac{\mathrm{d}M}{\mathrm{d}y}+\frac{1}{R}\frac{\mathrm{d}R}{\mathrm{d}y}-\frac{1}{T_0-T_w}\frac{\mathrm{d}T_w}{\mathrm{d}y}\right], \qquad (4.12)$$

is used to determine the energy thickness Φ of the boundary layer at the nozzle wall. The previous equation is based on a constant enthalpy flux of the adiabatic potential mass flow within the boundary layer. Both differential equations, (4.11) and (4.12), are numerically solved by a fourth order Runge-Kutta algorithm utilizing a step size control from COLLATZ [55].

The skin-friction coefficient, in general definded by $C_f = 2\tau_w/(\rho v^2)$, is being determined by solving the following expressions which are based on a modified computation of COLES method for a flat plate:

$$\mathrm{Re}_{\varPhi} = \frac{\rho v \varPhi}{\eta_0} \left(1 + \frac{\kappa - 1}{2} M^2\right)^m , \tag{4.13}$$

$$\overline{C_f \mathrm{Re}_{\bar{\theta}}} = \left(\frac{T_{aw}}{T}\right)^{1-m} C_{f_a} \mathrm{Re}_{\varPhi}, \tag{4.14}$$

$$\bar{C}_f = \frac{0.009896}{(\overline{C_f R_{\bar{\theta}}})^{0.562}}, \qquad \overline{C_f R_{\bar{\theta}}} \leq 2.51, \tag{4.15}$$

$$\bar{C}_f = \text{linearly interpolated from Table 4.1,} \qquad 2.51 < \overline{C_f \mathrm{Re}_{\bar{\theta}}} \leq 64.8,$$

Table 4.1: Local friction law according to COLE's relation for a turbulent boundary layer.

$\overline{C_f \mathrm{Re}_{\bar{\theta}}}$	2.51	3.10	3.97	4.88	5.73	7.41	8.94	12.75	16.36	23.2	29.6	35.9	41.8	53.6	64.8	
$\bar{C}_f$	0.00590	0.00524	0.00464	0.00426	0.00398	0.00363	0.00340	0.00308	0.00290	0.00269	0.00255	0.00246	0.00238	0.00227	0.00219	

$$\left(\frac{2}{\bar{C}_f}\right)^{\frac{1}{2}} = 2.44 \left[\ln \overline{C_f \mathrm{Re}_{\bar{\theta}}} - \ln\left(3.781 \bar{C}_f - \frac{25.104}{\sqrt{2}} \bar{C}_f^{(\frac{3}{2})}\right)\right] + 7.68, \quad \overline{C_f \mathrm{Re}_{\bar{\theta}}} > 64.8, \tag{4.16}$$

$$C_{f_a} = \bar{C}_f \left(\frac{T}{T_{aw}}\right) \left[1 + 17.2 \left(\frac{T_0}{T_{aw}} - 1\right) \left(\frac{\bar{C}_f}{2}\right)^{\frac{1}{2}} - 305 \left(\frac{T_0}{T_{aw}} - \frac{T}{T_{aw}}\right) \frac{\bar{C}_f}{2}\right]^{-m} . \tag{4.17}$$

The variables introduced in above equations are the energy thickness Reynolds number $\mathrm{Re}_{\varPhi}$, the adiabatic skin-friction coefficient C_{f_a}, the variable $\overline{C_f \mathrm{Re}_{\bar{\theta}}}$ denotes the implicitly given product of C_{f_a} and Re_{θ} (latter one is defined through equation (4.13) by replacing $\varPhi$ with θ) for low-speed flow, and $\bar{C}_f$ which is the low-speed flow value of C_{f_a}. There are two optional ways to determine the skin-friction coefficient as described below.

In the first method C_f is directly related to C_{f_a} which is evaluated at free-stream gas properties (referred to as *FSP* in the following). This represents the case of an adiabatic nozzle wall. For a specific interval of $\overline{C_f \mathrm{Re}_{\bar{\theta}}}$, with appropriate values of $\mathrm{Re}_{\varPhi}$ from (4.13) as well as $\bar{C}_f$ from (4.15), (4.16) and Table 4.1, equations (4.14), and

(4.17) yield two values of C_{f_a}. These are correlated by successive iteration till to the satisfaction of a certain convergence criteria. The nonlinear implicit equation (4.16) is solved with respect to $\bar{C}_f$ by the Newton-Raphson method. C_f is then given by

$$C_f = C_{f_a}, \qquad \text{(FSP)}. \tag{4.18}$$

The second method applies a film-temperature correction (*FTC*) to determine C_f, at gas-properties evaluated at the arithmetic-mean temperature of T and T_w, representing the case of a severely cooled nozzle wall. Here the skin-friction coefficient is determined by equation (4.19) wherein $\bar{C}_f$ results from (4.15), (4.16) and Table 4.1 but with a substitution of the variable $\overline{C_f \mathrm{Re}_{\bar{\theta}}}$ according to the product of $\bar{C}_f \mathrm{Re}_\theta$. In this case C_f is determined according to

$$C_f = \bar{C}_f \left[\frac{1}{2}\left(\frac{T_w}{T} + 1\right)\right]^{\frac{(m-3)}{4}}, \qquad \text{(FTC)}. \tag{4.19}$$

The Stanton number, as included in equation 4.12, is computed according to

$$\mathrm{St} = \frac{\dfrac{C_f}{2}\left(\dfrac{\Phi}{\theta}\right)^n}{1 - 5\left(\dfrac{C_f}{2}\right)^{\frac{1}{2}}\left[1 - \mathrm{Pr}_c + \ln\left(\dfrac{6}{5\mathrm{Pr}_c + 1}\right)\right]}. \tag{4.20}$$

The last unknown in equation 4.11 is the shape parameter to express the ratio of displacement thickness δ^* to momentum thickness θ as determined with the following expression. *Case I:* $\zeta \geq 1$

$$\frac{\delta^*}{\theta} = \frac{\dfrac{T_w \zeta^7}{7T} - I_2 - I_3}{I_1} \tag{4.21}$$

wherein

$$\zeta = \left[\frac{\Phi I_1}{\theta\left(I_2' + I_3'/\zeta\right)}\right]^{\frac{1}{8}} \tag{4.22}$$

Case I: $\zeta < 1$

$$\frac{\delta^*}{\theta} = \frac{\dfrac{T_w}{7T} - I_6 - I_7}{I_4 + I_5} \tag{4.23}$$

wherein

$$\zeta = \left[\frac{\Phi(I_4 + I_5)}{\theta I_1'}\right]^{\frac{1}{8}} \tag{4.24}$$

The integrals in above equations I_i $(i = 1, \dots, 7)$ and I_j' $(j = 1, 2, 3)$ are given in appendix A.1. Their values are computed with Gauss-Legendre integration method of 10th order, as described in [31]. Equations (4.22) and (4.24) are solved for ζ by utilizing regula falsi method. To improve the solutions of Φ, θ, C_f, $\delta^*$and St the algorithm ranging from equation (4.11) to (4.24) is iterated until reaching the convergence of successive values of ζ.

From the general definition of the Stanton number $\mathrm{St} = \alpha/(\rho c_p v)$ the local heat-transfer coefficient is then found to be

$$\alpha_g = c_p \rho v \mathrm{St}, \tag{4.25}$$

and the wall heat flux q_w is determined again through equation (4.7).

This algorithm and the necessary subroutines were implemented as macros, written in the APDL language, which are then called during the FEM routine. A verificaton of the turbulent boundary-layer code, was conducted with a sample computation with the equal input data as taken in the original source [47]. A comparison of the resulting heat-transfer coefficient values with those given in the reference curves show a good correlation with acceptable deviations of the numeric values. A possible explanation could be the utilization of an implicit method for solving the differential equations numerically in the original source. Curves of the heat-transfer coefficient, again plotted versus the axis distance, determined with the turbulent boundary-layer algorithm are depicted in Figure 4.7 for varying conditions of the stagnation or chamber pressure, the wall temperature, and the method used to compute the skin friction coefficient. In principle the shape of the α_g curves are similar to those presented in Figure 4.6, but the maximum values here are obviously just a fourth of those gained with the *Bartz equation*. Another finding is the partial dependence of the heat-transfer coefficient value on the wall temperature in relation to the method by which C_f is being calculated. The influence of T_w nearly vanishes for those skin friction coefficients evaluated with the FSP option, in contrast to a significant effect of T_w when choosing the FTC option.

For both methods, the *Bartz equation* as well as the *turbulent boundary-layer analysis*, the remaining unknown term is the distribution and magnitude of the wall temperature T_w. As it was described above, especially the values of T_w in the throat section are able to weight the actual size of α_g and consequently the heat flux into the wall of this area. Therefore T_w is prescribed by a certain initial temperature profile along the axis of the nozzle at the beginning of an analysis. During a transient thermal analysis the resulting local wall temperatures of the previous time step solution are then used for recomputing the local values of the heat-transfer coefficient in the current time step. In case of a stationary thermal analysis the final values of α_g are determined after the convergence of iterative temperature solutions, using the same procedure to update the wall temperatures like for transient solutions.

Due to default of wall temperatures measurements, acquired in practical firing tests with the actual thruster geometry, only results found in publications are supposed to answer the question about the method applied to determine the heat-transfer coefficient in the thermal model. Comparisons between measured and predicted heat transfer coefficients, as conducted in references [27] and [47], propose the use of film-temperature correction (FTC) option to estimate the heat flux in rocket motors with a combustion process, while the evaluation of the skin friction coefficient at free-stream gas properties (FSP) are more accurate in case of hot gases in absence of combustion products. The heat transfer coefficient in the following thermal FEA is then evaluated with the turbulent boundary-layer analysis utilizing the FTC option, as recommended.

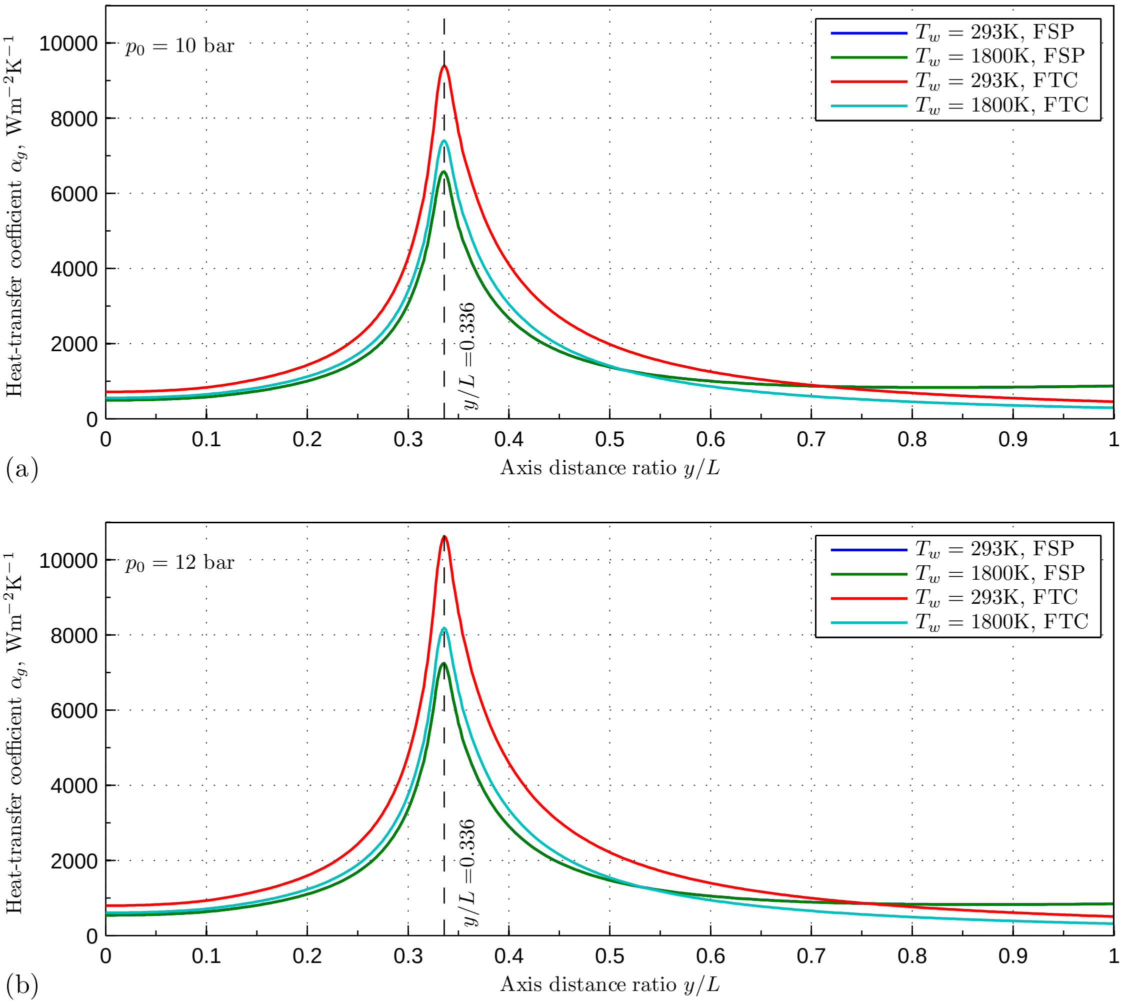

Figure 4.7: Heat-transfer coefficients plotted over the axis distance for a stagnation pressure of (a) 10 bar and (b) 12 bar at varying wall temperature and skin friction values.

4.2.2 Radiative Heat Transfer at Exterior Surfaces

Thermal radiation is considered to be the only heat flow which accounts for the cooling in this model. Based on the energy transport in form of electromagnetic waves it is the only form of heat transfer without matter being involved. Thus a permanent cooling through thermal radiation is inevitable for the temperature control of space crafts.

The radiative heat flow from a black body is described by the Stefan-Boltzmann law

$$\dot{Q} = \sigma A T^4 \tag{4.26}$$

where A and T are the area and temperature of the surface, respectively and the Stefan-Boltzmann constant written as $\sigma = 5.6704 \cdot 10^{-8}$ $\mathrm{Wm^{-2}K^{-4}}$. The thruster model is assumed to be a grey body emitting a radiative heat flow

$$\dot{Q} = \varepsilon(T) \sigma A T^4, \tag{4.27}$$

that is reduced by an emissivity factor $\varepsilon(T)$, $0 < \varepsilon(T) < 1$ relative to the black body. For outer surfaces of the thruster the value of emissivity is chosen to be a constant $\varepsilon(T) = \varepsilon = 0.8$, independent of the surface temperature. Rhenium is used as a common surface coating on rocket nozzles [2], applied e.g. with chemical vapour deposition (CVD), which posses an emittance in that range. Acting as heat sink, the background radiation into outer space is modelled with a temperature of 2.7 K.

4.2.3 Further Contributions to Heat Transfer

Fuel line and oxidizer line

A simple estimation of the convective heat transfer through the fuel line is based on the assumption of a fully developed flow through a pipe having a mean inner diameter $d_f = 0.3$ mm. The fuel properties are approximated with these of $C_{12}H_{26}$, taken at a fluid temperature of 373 K from [34]. Determining the flow velocity through

$$v_f = \frac{4\dot{m}_f}{d_f^2 \pi \rho_f} = \frac{4\dot{m}}{d_f^2 \pi \rho_f (O/F + 1)} = \frac{4 \cdot 0.336 \cdot 10^{-3}}{0.3^2 \cdot 10^{-6} \pi \; 691.5 \; (7.25 + 1)} = 0.832 \text{ ms}^{-1}, \tag{4.28}$$

the Reynolds number yields

$$\mathrm{Re} = \frac{v_f d_f \rho_f}{\eta_f} = \frac{0.832 \cdot 0.3 \cdot 10^{-3} \; 691.5}{0.51 \cdot 10^{-3}} = 338.58 \tag{4.29}$$

---

[2] Rhenium coating from ULTRAMET
`http://www.ultramet.com/refractory_metal_coatings.html`

which characterises the pipe flow to be laminar. The heat-transfer coefficient follows from the *Graetz-Nusselt* asymptotic solution with

$$\alpha_f = 3.657\frac{\lambda_f}{d_f} = 3.657\frac{0.118}{0.3\cdot 10^{-3}} = 1438.41\ \mathrm{Wm^{-2}K^{-1}}. \tag{4.30}$$

Again pipe flow relations are used to calculate the amount of heat transferred from the water/oxygen gas mixture into the wall of the oxidizer line, connecting the decomposition chamber with the injector manifold. The heat-transfer coefficient of the turbulent pipe flow with gas properties from Table 2.1 is determined by the *Gnielinsky* equation, which is

$$\alpha = \left(\frac{\lambda_D}{d}\right)\frac{\mathrm{Re}\mathrm{Pr}_D(0.78\ln\mathrm{Re}-1.5)^{-2}/8}{1+12.7(0.78\ln\mathrm{Re}-1.5)^{-1}/\sqrt{8}(\mathrm{Pr}_D^{2/3}-1)} = 2889.4\ \mathrm{Wm^{-2}K^{-1}}. \tag{4.31}$$

Decomposition chamber, injector manifold and combustion chamber entrie

At these locations the exact circumstances of the gas flow are left unclear and a typical value for gases of $\alpha = 100\ \mathrm{Wm^{-2}K^{-1}}$, from [33] at the decomposition temperature $T_D = 960.3$ K is set to estimate the convective heat transfer.

4.3 Mechanical Loads

In general the spectra of mechanical loads are different for specific mission stages, for instance during the launch of the spacecraft or in the following service times of certain components and devices in space. Structural loads acting on the spacecraft structure and components during the launch are caused by:

- inertia forces, caused by the in-flight acceleration and vibrations
- shock loads, due to launch vehicle stage and spacecraft separation as well as the fairing jettison
- drop of static pressure inside the payload compartment of the launch vehicle

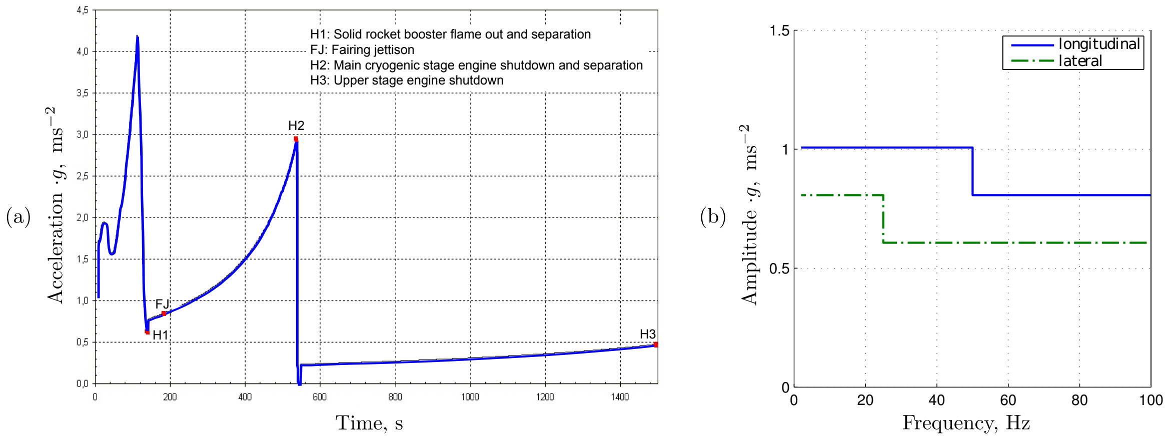

Figure 4.8: Typical load spectra during the launch of Ariane 5 from [5]. (a) Longitudinal static acceleration; (b) Sine excitation at spacecraft base.

Figure 4.8 shows exemplary diagrams of the longitudinal static acceleration and dynamic equivalent sinusoidal excitation of the spacecraft mounting base during the flight of the Ariane 5 launch vehicle from [5]. A complete examination of these load

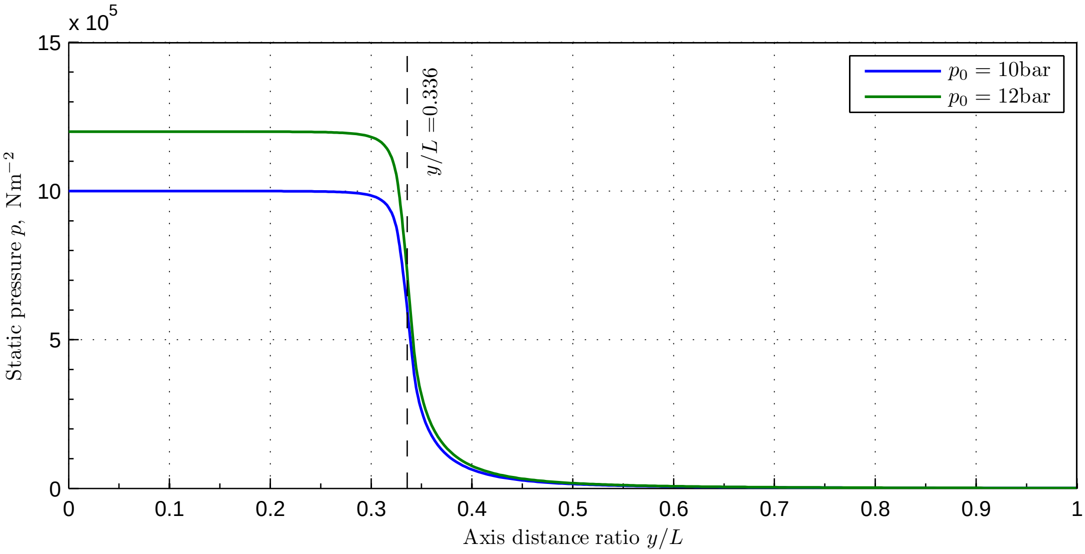

Figure 4.9: Static gas pressure distribution inside the nozzle versus axial distance ratio.

scenarios for the present thruster would not only imply additional knowledge about the structural design of the spacecraft, but also go beyond the scope of this work. Structural loads acting on the thruster while operation are only considered due to the internal pressure for present computation model. The distribution of the pressure exerted on the walls inside the decomposition and combustion chamber, as well as the injector manifold is taken to be constant, at a value equal to the combustion pressure $p_c = p_0$. As mentioned before due to this assumption any loss of pressure is neglected till to the nozzle entrie. The static pressure of the gas flow inside the nozzle is determined by the isentropic gas relation

$$p = p_0 \left(1 + \frac{(\kappa - 1)}{2} M^2\right)^{\frac{\kappa}{1-\kappa}} . \tag{4.32}$$

The situation of the gas pressure acting on the nozzle wall is plotted along the axis distance in Figure 4.9.

4.4 Thermal and Structural FEA Model

The imported thruster geometries in two and three dimensions are being meshed by using the mesh generator routines *AMESH* and *VMESH* without mapping. The mesh size control is either automatically done with an adjustment to the geometry contour or with a prescribed element edge length within specific model regions. The elements used to generate the meshes are listed and characterised below.

Thermal solid elements:

SOLID87	3-D 10-node tetrahedron with 6 integration points, temperature DOF, quadratic shape functions, and a consistent (not diagonalised) convection matrix for strong temperature gradients
PLANE77	2-D 8-node quadrilateral shape with 3x3 integration points, temperature DOF, quadratic shape functions, and a consistent (not diagonalised) convection matrix, axisymmetric elment behaviour

Thermal surface effect elements:

SURF152	3-D 6-node triangular shape with 6 integration points, having an extra node for radiation, temperature DOF at each node, quadratic shape functions, radiation formfactor FORMF = 1, Stefan-Boltzmann constant SBCONST = $5.6704e-8$, emissivity EMIS = 0.8
SURF151	2-D 3-node line with midside node and 2 integration points, having an extra node for radiation, temperature DOF, quadratic shape functions, axisymmetric elment behaviour, radiation formfactor FORMF = 1, Stefan-Boltzmann constant SBCONST = $5.6704e-8$, emissivity EMIS = 0.8

Structural solid elements:

SOLID92	3-D 10-node tetrahedron with 4 internal integration points and additional 6 at the face with pressure load, translational DOF's (UX, UY, and UZ), quadratic shape functions
PLANE82	2-D 8-node quadrilateral shape with 2x2 internal integration points and additional two at the line with pressure load, translational DOF's (UX, and UY), quadratic shape functions, axisymmetric element behaviour

The general procedure was to generate the mesh with thermal solid elements (SOLID87 and PLANE77) first, then followed by overlaying outer surfaces with the thermal effect elements (SURF152 and SURF151) in a manner that they share their nodes with underlying solid elements. The correct assignment of materials while creating surface elements is essential, since an overlay of two thermal effect surface elements, but having different materials, on the same outer surface position is accepted by the program. The increased radiation surface resulted in ironic temperature differencies between the 2D- and the 3D-model.

The mesh used for the structural analysis was not altered, but the existing solid elements of the thermal mesh were changed to the type of structural solid ones (SOLID92 and PLANE82). This allows a direct nodal temperature transfer from the thermal

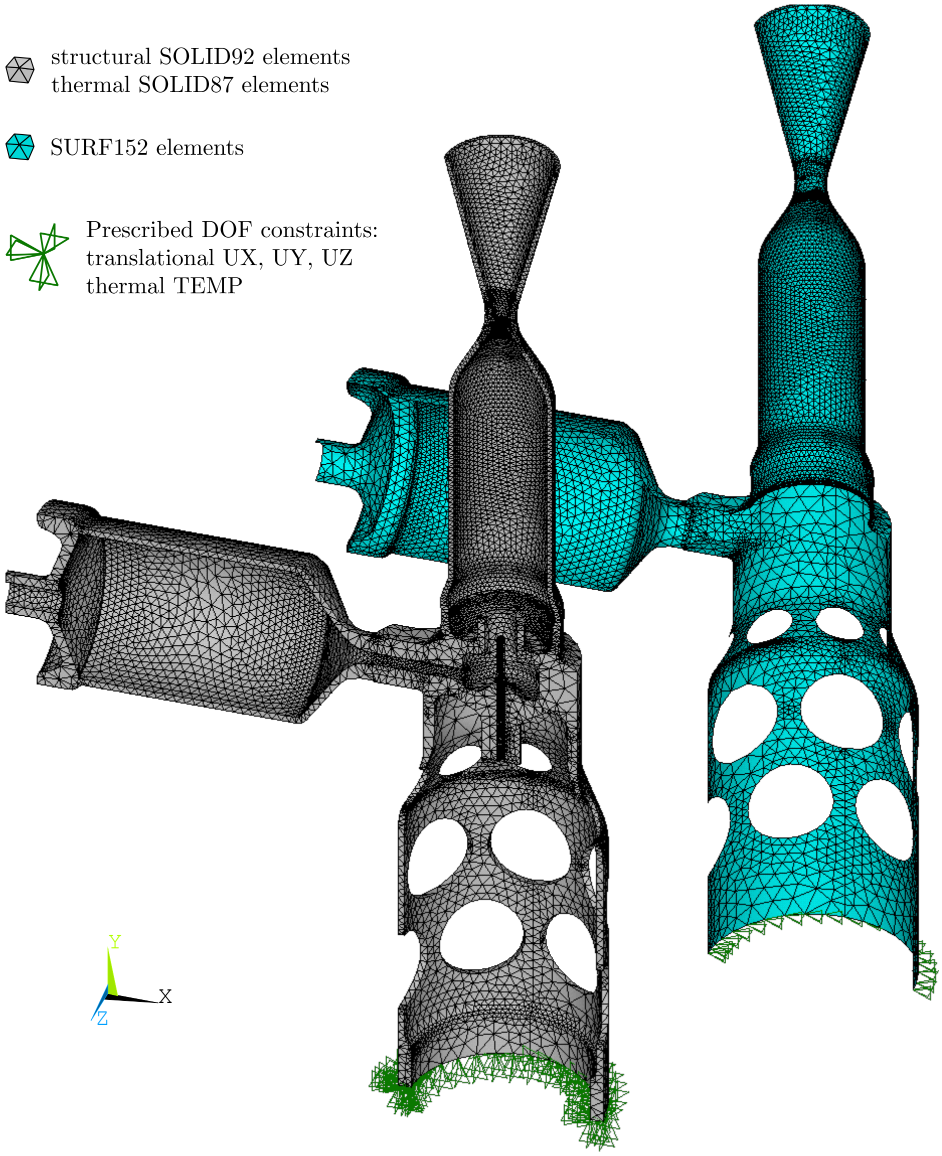
structural SOLID92 elements
thermal SOLID87 elements
SURF152 elements
Prescribed DOF constraints:
translational UX, UY, UZ
thermal TEMP
Y
X
Z

Figure 4.10: Element plot of the 3-D model.

result, to be used as a prescribed nodal temperature field within the structural analysis. The thermal surface effect elements were redefined as null element and therefore ignored during solution. The thermal and structural models are being saved in separate databases for later reuse and manipulation in transient or cyclic solutions. Figure 4.10 shows the three dimensional model meshed with tetrahedral elements, and the detached surface built up of thermal effect elements. Considering the strucural model the nodes at the bottom ring of the thermal barrier cylinder are fixed, having translational constrained DOF as UX = UY = UZ = 0. To establish the symmetry condition these nodes which are lying on the x-y plane are constrained with UZ = 0 (DOF symbols are not shown for these nodes in Fig 4.10). Hence the elements lack of rotational degrees of freedom the necessary locking of rotations about x- and y-axis (ROTX = ROTY = 0) is omitted. Regarding the thermal model the temperature of these nodes is prescribed with TEMP = 293 K. In addition to this the temperature of the extra node, which accounts for the radiative heat transfer from the surface effect elements, is fixed to 2.7 K. The same boundary conditions are applied in the two dimensional structural, respectively thermal FEA models for the nodes at the baseline of the thermal barrier cylinder, see Figure 4.12, and the extra radiation node.

The convective thermal loads inside the thruster, as described above in Section 4.2.1, are defined via element surface loads. Two locally varying parameters, the heat transfer coefficient (film coefficient HCOEF) and the bulk temperature of the fluid (TBULK) are input at nodes that span a free surface of each element focused on. Bulk temperatures and heat transfer coefficient values are kept constant once applied, except within the regions of combustion chamber and nozzle. Here the HTC values, computed according the turbulent boundary-layer analysis with the *FTC* option, vary depending on the actual wall temperature. The situation of these convective loads in the thermal equilibrium state is depicted in Figures 4.11 (a) and (b) for the three dimensional and in Figures 4.12 (a) and (b) for the two dimensional FEA models respectively.

Considering the structural loads, the normal pressure exerted on the inner surfaces is the only contribution to the external forces acting here. The definiton as a surface element load is done like above, but with locally varying values of the normal pressure as nodal input data. The pressure distribution is illustrated in Figure 4.11 (c) as contour plot of the three dimensional model and in Figure 4.12 (c) as face outlines of two dimensional FEA model.

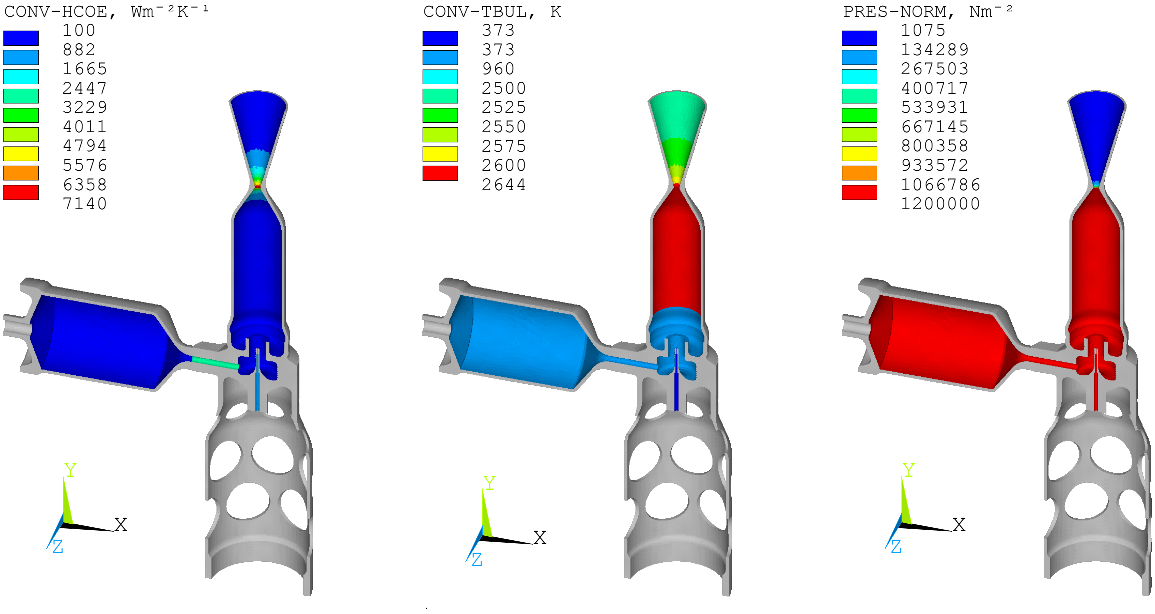
CONV-HCOE, Wm⁻²K⁻¹
100
882
1665
2447
3229
4011
4794
5576
6358
7140
CONV-TBUL, K
373
373
960
2500
2525
2550
2575
2600
2644
PRES-NORM, Nm⁻²
1075
134289
267503
400717
533931
667145
800358
933572
1066786
1200000
Y
X
Z

(a) (b) (c)

Figure 4.11: Contour plot of nodal surface loads acting upon the inner walls of the 3-D model. Thermal load defined as convective heat transfer (a) distribution of the heat transfer coefficient and (b) distribution of the fluid bulk temperature; (c) Normal pressure applied as structural load.

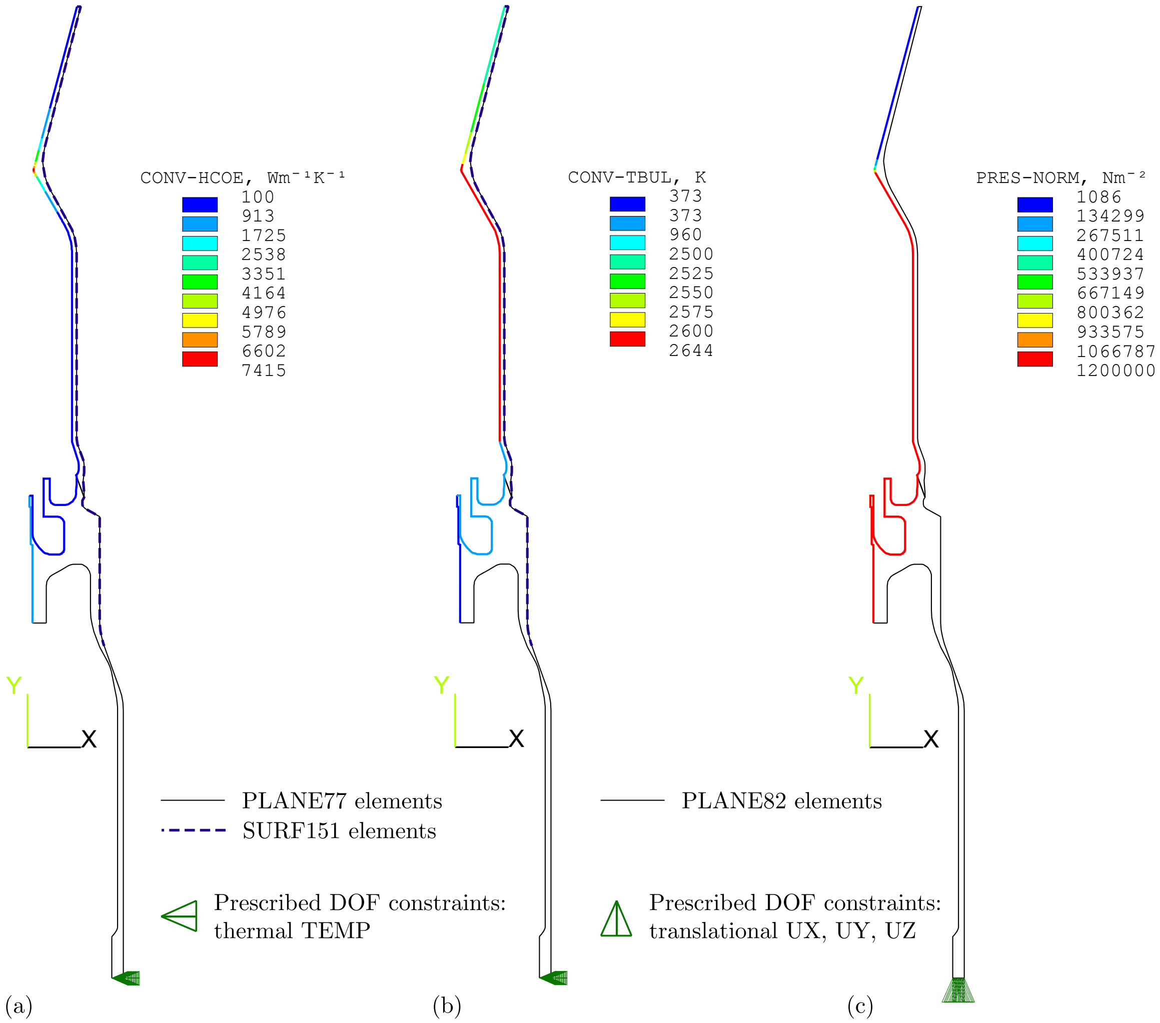
CONV-HCOE, Wm⁻¹K⁻¹
100
913
1725
2538
3351
4164
4976
5789
6602
7415
CONV-TBUL, K
373
373
960
2500
2525
2550
2575
2600
2644
PRES-NORM, Nm⁻²
1086
134299
267511
400724
533937
667149
800362
933575
1066787
1200000
Y
X
Y
X
Y
X
PLANE77 elements
SURF151 elements
PLANE82 elements
Prescribed DOF constraints: thermal TEMP
Prescribed DOF constraints: translational UX, UY, UZ

(a) (b) (c)

Figure 4.12: Outline of the 2-D axisymmetric FEA models. Thermal model with both element types, the prescribed temperature DOF together with the distribution of (a) the heat transfer coefficient and (b) the bulk temperature of the fluid; (c) Structural model with translational DOF and the internal pressure acting as structural load.

5 FEA Results and Discussion

In the following sections the FEA results from the combined thermo-mechanical investigations of the exemplary thruster geometry are presented. The chapter is split into two sections, each dedicated to one of the thrust chamber materials Pt-10%Rh DPH and iridium, beginning with the former one.

5.1 Material Combination with Pt-10%Rh DPH

5.1.1 Stationary Thermal Analysis

In this section the stationary temperature fields are presented for the 3-D model, starting with the thermal solution when the thruster is out of operation, or in the idle cold state. Here the fuel valves are shut, hence the thermal loads due to the H_2O_2 decomposition and the combustion in the following are not present. The only thermal input comes from the base of thermal-barrier cylinder which is constricted to a constant temperature of 293 K, assumed to be equal the inner satellite structure. The contour plot of the temperature field in this case is shown in Figure 5.1. Due to the radiation into outer space the temperature continuously drops from the base towards the nozzle. The lowest values are encountered at the decomposition chamber cap, on the outer edge of the centre bore hole. The thermal solution of the operational hot firing state is considered next. In this load case the complete set of thermal loads are active, see Fig. 4.11 (a) and (b). Temperatures of selected nodes that are placed on the thrust chamber are listed for discrete time stamps in Table 5.1. After a time of 2 seconds nodes at nozzle throat and exit are near thermal equilibrium, whereas those in the chamber are increasingly unbalanced in direct relation to the distance from the throat.

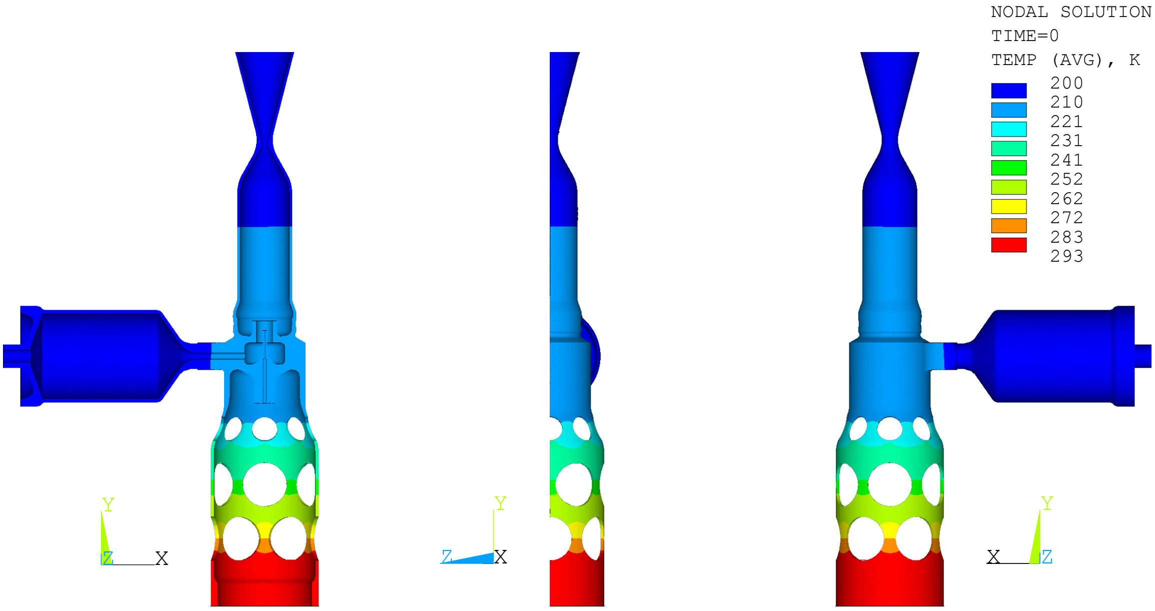

Figure 5.1: Contour plot of averaged nodal temperature solution in the stationary cold state.

The stationary thermal solution is taken in a first validation attempt regarding the use of the platinum alloy as a thrust chamber material. The temperature distribution, that arises after the fourth equilibrium iteration, is depicted in Figure 5.2. The hottest region spreads from the nozzle entry downstream to about half the length of the divergent part. The maximum temperature value of 1999 K is located inside the nozzle throat. Comparing stationary data at both chamber pressures $p_0 = 12$, and $p_0 = 10$ bar of the throat yields a temperature difference of about 35 K. Bearing in mind the melting point of 2123 K the temperature ratio reached is $T_S/T_m = 1999/2123 \approx 0.94$. This value quite exceeds 0.88, which is defined by a reasonable temperature limit of 1873 K (1600°C) for structural applications.

There is no significant margin left towards higher service temperatures for the platinum alloy as thrust chamber material for this model configuration. Because of this, and a lack of material properties given at these temperature level, further structural investigations are not considered to give reasonable predictions.

Table 5.1: Temperatures in K of nodes located on the thrust chamber, at discrete time stamps.

		Pressure $p_0 = 12$ bar				Pressure $p_0 = 10$ bar			
Node locations		time in s				time in s			
		0	1	2	∞	0	1	2	∞
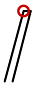	Nozzle exit	209.1	1099.8	1465.1	1655.2	209.1	1052.6	1425.1	1632.5
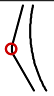	Nozzle throat	209.7	1558.9	1860.7	1998.6	209.7	1492.8	1808.0	1962.8
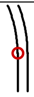	Nozzle entry	210.1	1150.5	1567.9	1801.2	210.1	1097.3	1518.6	1772.1
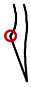	Point A	211.4	459.3	669.8	1234.7	211.4	444.0	647.3	1218.6
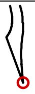	Point B	211.7	370.0	521.7	1145.6	211.7	360.6	507.1	1132.3

5.2 Material Combination with Iridium

5.2.1 Thermal Analysis of the 3-D Model

The focus is now drawn onto the thermal inquiry of the thruster with a chamber made of iridium, the second material of interest. Figure 5.3 shows the transient temperature field during heating at distinct times beginning at 0.2 seconds up to 60 seconds after ignition. Here the individual front views of the model are scaled with a unique contour layout to mark the time-dependent temperature propagation through the structure.

The stationary cold state is not shown because it is practically the same as in Fig. 5.1. The temperature distribution of the thermal solution, regarding the stationary hot condition during the operation is depicted separately in Figure 5.4. Taking a closer look at the distribution of the temperature contour edges of the thrust chamber, the manifold, and the barrier cylinder indicates that these is nearly symmetric around the thrust chamber axis for both the transient, as well as the stationary plots. Because of

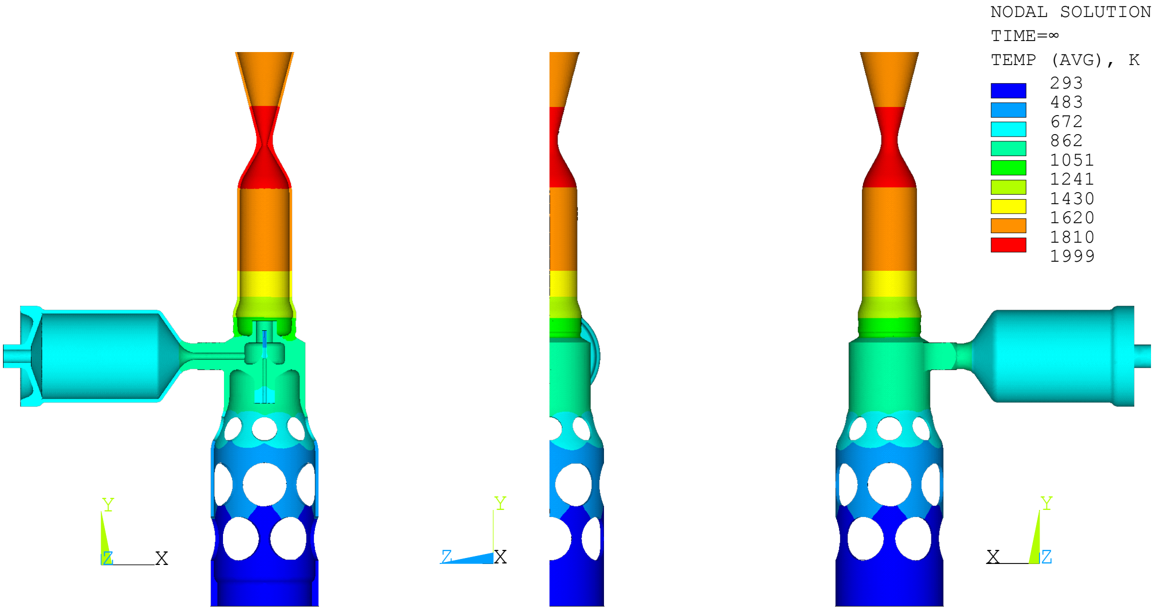

Figure 5.2: Contour plot of averaged nodal temperatures in the stationary thermal hot state.

the high thermal flux acting inside, the nozzle region is rapidly heated up. Considering the upper part of the combustion chamber together with the nozzle, it is found that temperatures does not change significantly after passing a time of 10 seconds from ignition. In contrast to this, the dynamic heating of the decomposition chamber and the thermal barrier cylinder is more retarded. Here the thermal equilibrium is not reached even after one minute of firing.

A diagram of continuously interpolated temperature curves versus time is shown in Figure 5.5 (a) for a selected set of nodes. The curves at positions 1 up to 3, belonging to the convergent-divergent nozzle, show a step like characteristic in comparison with the slower ones from positions 4 to 6. Expressed in numbers the node at position $R2$ expiriences a sharp temperature increase of 2907 Ks^{-1} from zero-time up to 0.2 seconds, while the increase at position $R4$ is more than one order of magnitude lower with 236 Ks^{-1}. The temperature rate of position $R6$ at the onset of the thermal barrier cylinder is equal to $4 \cdot 10^{-2}$ Ks^{-1} in the interval from 0 to 0.2 seconds.

As mentioned above a two dimensional, axisymmetric model will be used to study the mechanical effects off cyclic thermal loadings, alternating from the cold to the stationary hot state. Therefore temperature differences of nodes facing each other

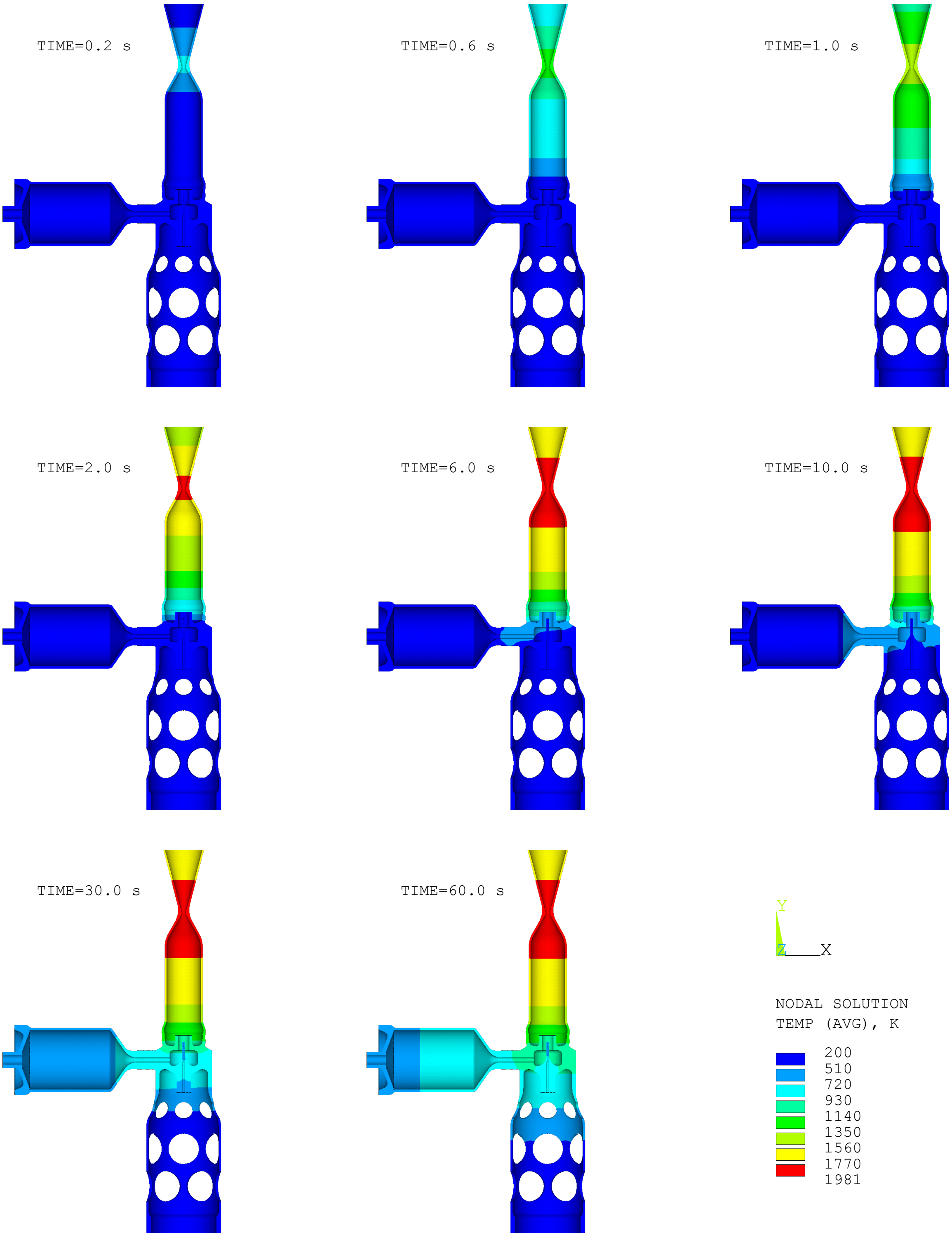

Figure 5.3: Temperature field at specific times during heating. The model is depicted in the front view.

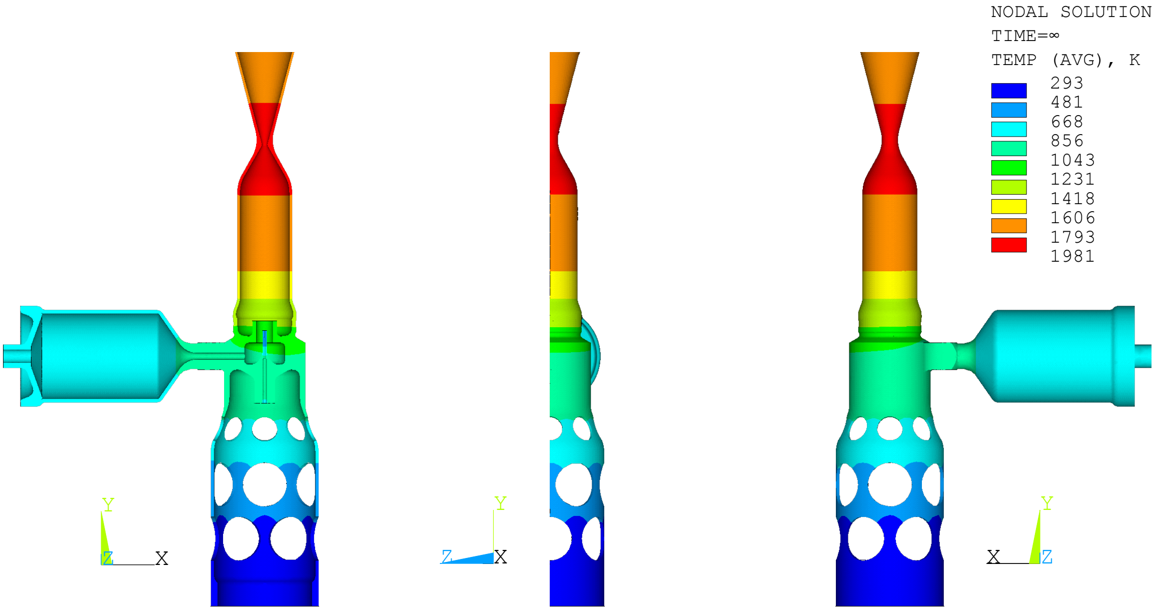

Figure 5.4: Contour plot of averaged nodal temperatures of the stationary thermal solution.

are plotted in Figure 5.5 (b) to verify the assumption of a rotational symmetric temperature distribution. At zero-time the deviations between left and right side nodes nearly vanish at every location. The differences in temperature of the hot state reach a maximum at location 6 with a value of $\Delta T_6 = 21.4$ K. Although there is the lowest absolute temperature $T_{R6} = 967$ K within the present set of nodes the difference is only 2.2%, which is acceptable.

Again the highest stationary temperature value is found inside the throat to be 1980 K. Related with the melting point of iridium this gives a ratio of $T_S/T_m = 1980/2720 \approx 0.73$, which lies in the lower service temperature range for this metal. The temperature situation at the welding zone to connect the thrust chamber with the propellant manifold is also given in Fig. 5.5 through points $R4$, $R5$, Ł4, and $L5$. In the hot equilibrium state the upper point of the butt weld R4 reaches a maximum temperature of $T_{R4} = 1275$ K whereas the lower end has a value of $T_{R5} = 1167$ K, which yields a difference of 108 K. Value T_{R4} is also regarded as the maximum service temperature the NiCr25FeAlY alloy is being exposed to, and lies below the maximum tolerable service temperature of 1473 K, from Section 3.2. In Figure 5.6 the radiated heat flows from outer surfaces of the particular components are plotted versus the

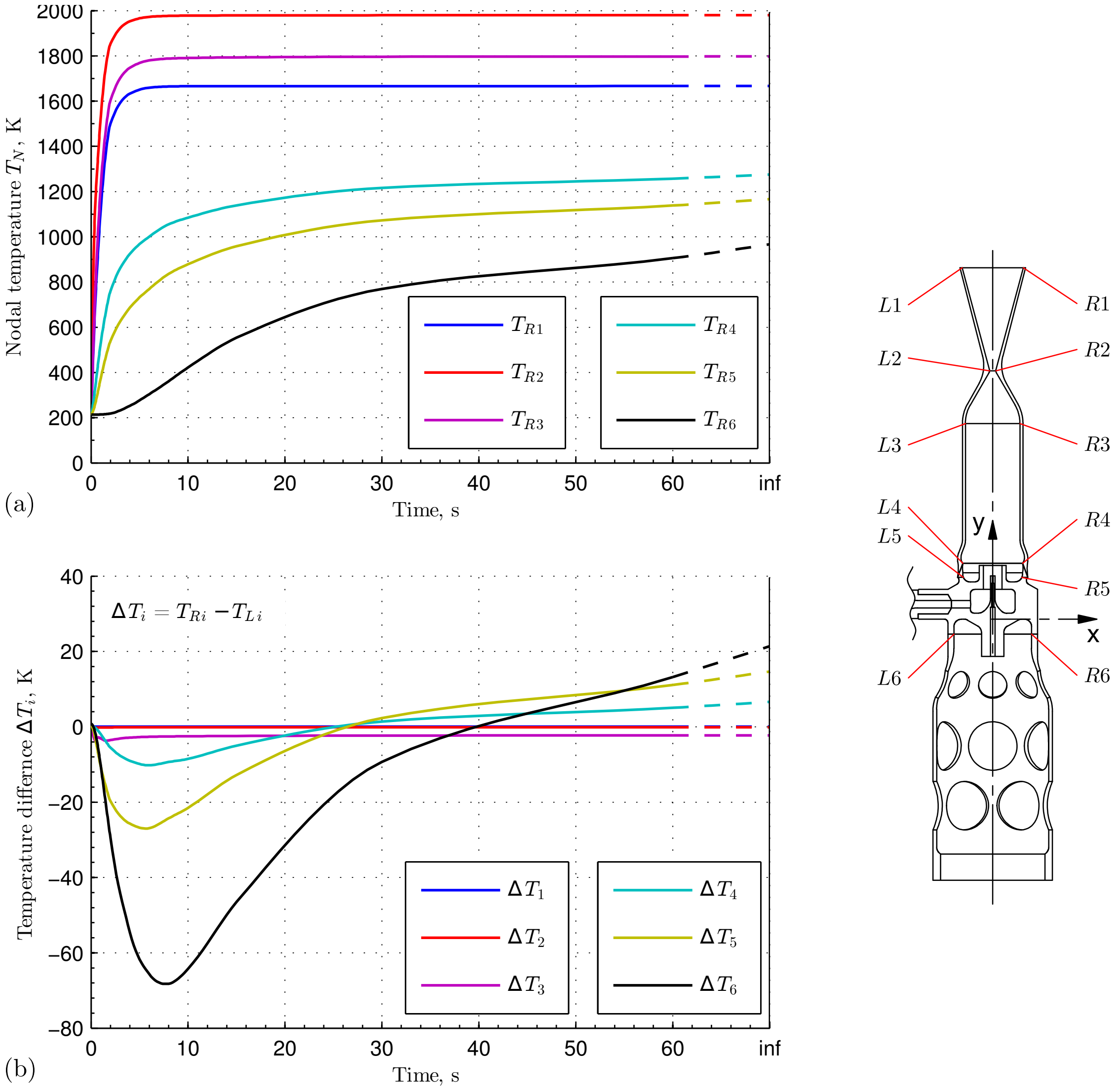

Figure 5.5: Interpolated temperatures curves plotted versus heating time (solid lines) which are expanded towards the stationary state (dashed lines). The selected nodes are lying in the x-y-plane, located on the inner sides of the thruster wall. (a) Absolute temperatures from nodes lying to the right of the y-axis; (b) Temperature difference of opposite nodes.

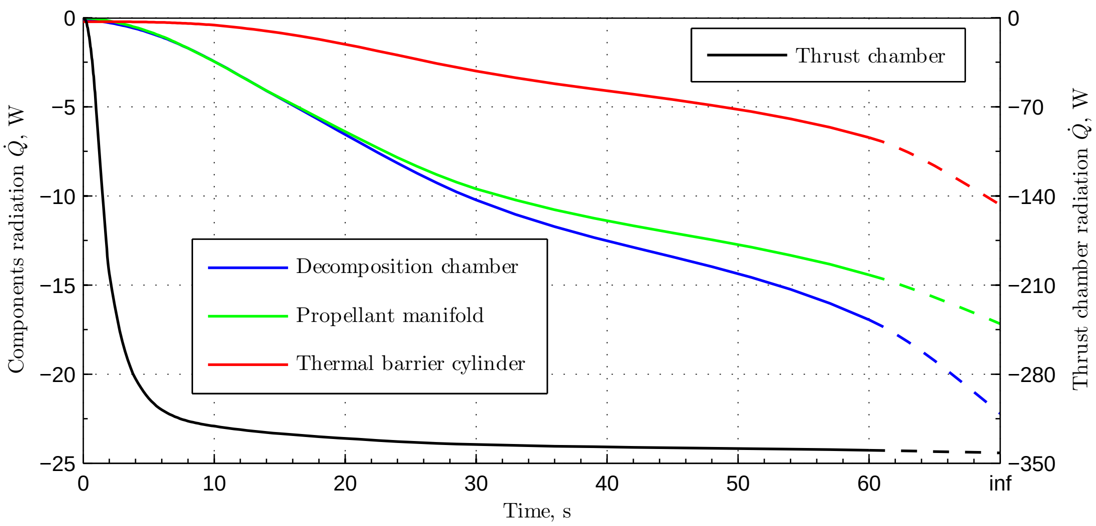

Figure 5.6: Total radiative heat flow from outer surfaces of single thruster components during the first 60 seconds of firing. The dashed lines are interpolations towards the stationary solution.

time during start up and interpolated towards stationary firing state. The total reaction heat flow at locations with constrained temperatures is plotted in Figure 5.7. The extra node represents the outer space and therefore balances the overall radiation coming from the thruster. As seen in Fig. 5.6 the biggest contribution to this heat flow comes from the thrustchamber, which reaches equilibrium very fast. The transient heat flow curve could be described with a bilinear function as simplification. In the stationary state the total radiation has a magnitude of 392 W. The blue curve is the heat flow through the circular ring at the base of the thermal barrier cylinder (see Fig. 4.10) into the satellite structure. At the beginning a value of −0.4 W indicates that heat is being transferred into the thruster. During the start up phase the sign becomes positive and the heat flow into the satellite gets a value of 1.6 W in the stationary state, which is only 0.4% of the total radiation. This clearly shows the insulation effect of the thermal barrier cylinder.

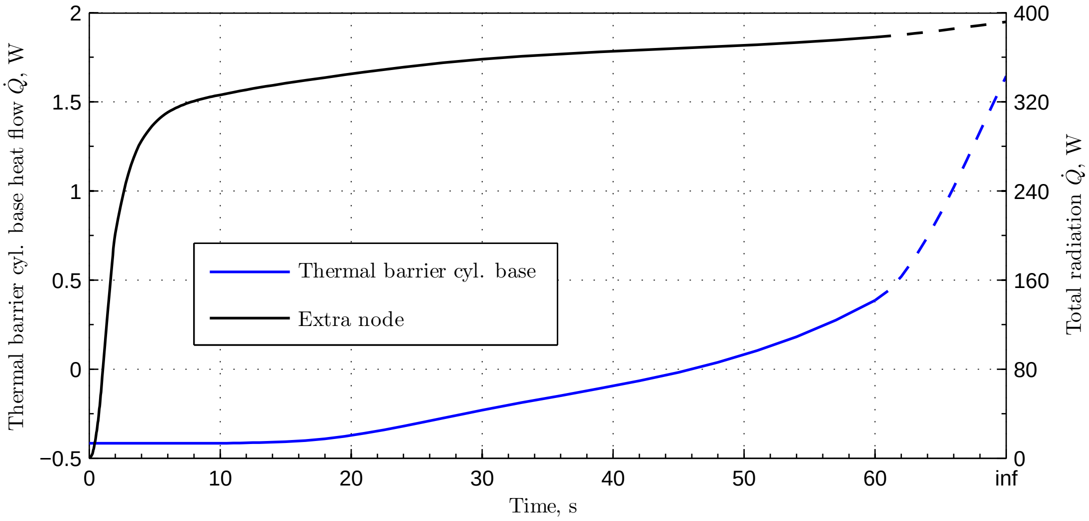

Figure 5.7: Reaction heat flow at the outer space node and into the base of thermal barrier cylinder, which are both constrained in temperature. The dashed lines expand the transient state after 60 seconds towards the stationary solution.

5.2.2 3-D Thermo-Stress Analysis

In the following the results from the structural FEA analysis are presented and discussed. The structural analysis is nonlinear because the stress-strain constitutive equation of the material was implemented as bilinear isotropic. Another important point is the temperature dependence of mechanical properties concerning the elastic modulus, the yield strength, and the Poisson ratio (as listed in Table 3.2 for iridium, and Table 3.4 for the NiCr25FeAlY alloy). The reference temperature for thermally induced strain is set to be eqval 293 K. In a short recapitulation, the structural loads comprise a static internal pressure at any time (see Fig. 4.11 (c)), and a body temperature field that varies in every time step.

The results description is introduced with a contour plot of the nodal displacements in y-direction, shown in Figure 5.8. The displacements are scaled by a factor of 20 to emphasise the deformed structure relative to the undeformed model edges. In the cold equilibrium state the body temperature field (see Fig. 5.1) drops below 293 K, consequently the structure undergoes a contraction with a minimum of $UY = -0.0456$ mm in y-direction at the nozzle exit. In the stationary firing state the structure undergoes a strong thermal expansion due to the high temperatures of the thrust chamber (see Fig. 5.4), which results in a maximum displacement of about $UY = 0.89$ mm, or 1.1% of the total thruster length. The obvious tilt of the decomposition chamber in Fig. 5.8 (b) is linked to the temperature difference in y-direction across the connection bar, located between chamber and the propellant manifold. The difference between the upper- and lower-edge temperatures reaches about 20 K at the manifold, and descends steadily towards the decomposition chamber, where it vanishes. Figure 5.9 shows the von Mises equivalent stress distribution, defined as

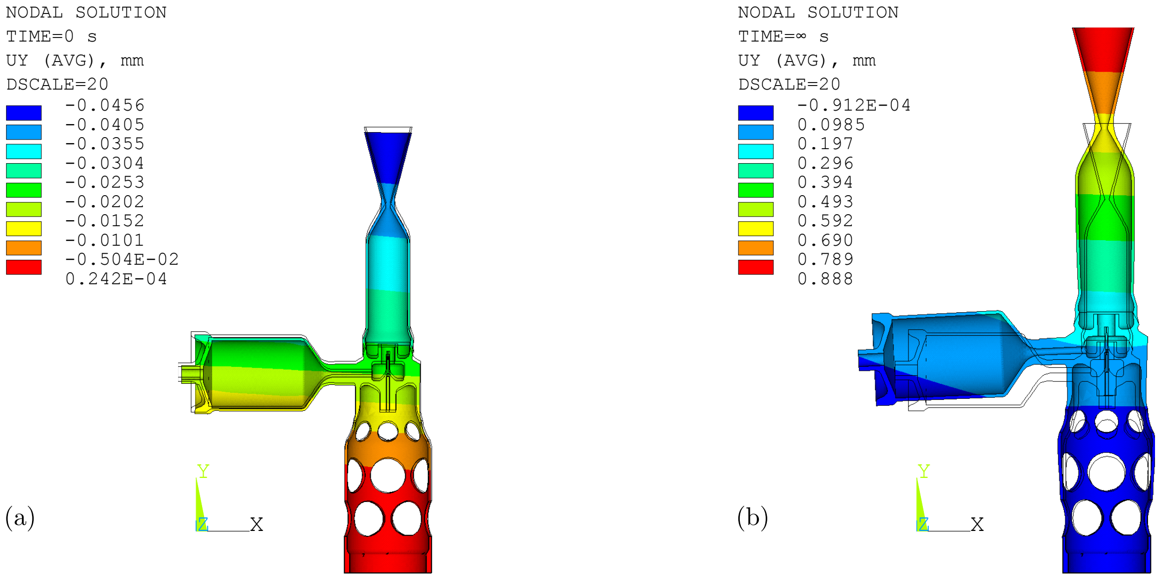

Figure 5.8: Contour plot of the nodal displacements in y-direction UY scaled with a factor of 20, at zero-time (a), and in stationary hot state (b). Black outlines represent the undeformed body edges.

$$\sigma_{eq} = \left(\frac{1}{2}\left[(\sigma_{xx}-\sigma_{yy})^2 + (\sigma_{yy}-\sigma_{zz})^2 + (\sigma_{zz}-\sigma_{xx})^2 + 6(\sigma_{xy}^2 + \sigma_{yz}^2 + \sigma_{zx}^2)\right]\right)^{\frac{1}{2}}, \quad (5.1)$$

in the structure at different times in the transient heating periode. At zero-time the stresses are concentrated in the vicinity of the inner and outer edges of the circumferential welded joint (points A and B respectively in Fig. 4.4). The stresses are rotationally symmetric along the thrust chamber axis, according with the welding geometry and the temperature field. Since the pressure exerted up on the inner walls does not cause stresses of that magnitude, these are mainly induced by the mismatching CTE values from both materials. These stress levels already cause a symmetric plastic flow in the iridium thrust chamber along the outer edge of the circular chamfer where ε^p_{eq} gains a value of $0.7 \cdot 10^{-3}$ at the tip. The plastic equivalent strain output from ANSYS, as defined in [1]

$$\varepsilon^p_{eq} = \frac{1}{1+\nu}\left(\frac{1}{2}\left[(\varepsilon^p_1 - \varepsilon^p_2)^2 + (\varepsilon^p_2 - \varepsilon^p_3)^2 + (\varepsilon^p_3 - \varepsilon^p_1)^2\right]\right)^{\frac{1}{2}} \tag{5.2}$$

where $\nu = 0.5$, requires a short discussion. This term is by no means linked with the accumulated equivalent plastic strain increment, since ε^p_{eq} yields only a comparative value of the present plastic strains at a certain point of the load history. Equation 5.2 can be rewritten as

$$\varepsilon^p_{eq} = \frac{1}{1+\nu}\left(\frac{3}{2}e^p_{ij}e^p_{ij}\right)^{\frac{1}{2}} \qquad i,j = x,y,z \tag{5.3}$$

where the components of the deviatoric plastic strain tensor are

$$e^p_{ij} = \varepsilon^p_{ij} - \frac{1}{3}\varepsilon^p_{kk}\delta_{ij} = \varepsilon^p_{ij}$$

since the plastic volume strain $\varepsilon^p_{ii} = 0$. With $\nu = 0.5$ equation 5.2 is finally transformed into

$$\varepsilon^p_{eq} = \frac{1}{1+0.5}\left(\frac{3}{2}\varepsilon^p_{ij}\varepsilon^p_{ij}\right)^{\frac{1}{2}} = \left(\frac{2}{3}\varepsilon^p_{ij}\varepsilon^p_{ij}\right)^{\frac{1}{2}}. \tag{5.4}$$

With the important exception that in eqn. 5.4 total plastic strain components are used, eqn. 5.4 looks like the relation for calculating the equivalent plastic strain increment $\mathrm{d}\bar{\varepsilon}^p$, where the components of the incremental plastic strain tensor are used. The accumulated amount of plastic deformation in a structural part depends on the load history. Within the context of plasticity theory a plastic strain *increment* $\mathrm{d}\varepsilon^p_{ij}$ is related to a load increment in the plastic flow state. The incremental plastic work $\mathrm{d}W^p = \sigma_{ij}\mathrm{d}\varepsilon^p_{ij} = \bar{\sigma}\mathrm{d}\bar{\varepsilon}^p$ defines the equivalent plastic strain increment $\mathrm{d}\bar{\varepsilon}^p$, where $\bar{\sigma}$ is the equivalent stress. The accumulated equivalent plastic strain is then

$$\bar{\varepsilon}^p = \int\limits_C \mathrm{d}\bar{\varepsilon}^p = \int\limits_C \left(\frac{2}{3}\mathrm{d}\varepsilon^p_{ij}\mathrm{d}\varepsilon^p_{ij}\right)^{\frac{1}{2}}. \tag{5.5}$$

The situation at 0.4 s is plotted in Fig. 5.9 (b), because at this time the highest stress values occur during the starting phase. Finally the stress distribution in the stationary hot firing state is depicted in Fig. 5.9 (c). Here the maximum stress values drop below those reached at prior time, firstly because the body temperature field is more uniform now, and secondly the higher temperatures diminish the mechanical properties.

In the following, expressions which are termed radial or tangential refer to the cylindric coordinate system whose axis of symmetry is coincident with the y-axis of the thrust chamber in the common orientation (see Fig 4.3). At zero-time, when the material is in virgin condition, a validation of the results output from the FEA is done by a comparison of the radial stresses σ_{rr} and tangential stresses $\sigma_{\varphi\varphi}$, mapped on paths in x, -z, and -x directions, located on the cross section in the middle of the cylindric combustion chamber. The general formulation of stresses in a cylinder, with outer R_o and inner radius R_i, that is exerted to pressure loads p_o and p_i follows from [29]

$$\sigma_{rr}(r) = \frac{R_i^2 R_o^2 (p_o - p_i)}{R_o^2 - R_i^2} \frac{1}{r^2} + \frac{p_i R_i^2 - p_o R_o^2}{R_o^2 - R_i^2} \tag{5.6}$$

$$\sigma_{\varphi\varphi}(r) = -\frac{R_i^2 R_o^2 (p_o - p_i)}{R_o^2 - R_i^2} \frac{1}{r^2} + \frac{p_i R_i^2 - p_o R_o^2}{R_o^2 - R_i^2}. \tag{5.7}$$

The diagrams of radial stresses and tangential stresses are shown in Figure 5.10 (a), and (b), respectively. In general a good correlation between the numerically computed stresses and the theoretical ones is observed. The numerical stresses are lines, because the element length coincides with the wall thickness in this region. The wrongly negative radial stress values at the outer radius are likely to be the product of interpolation. With increasing body temperatures the yield strength values as well as the elastic modulus are lowerd. This leads to larger structural deformations in the elastic regimes and to an extension of plastic flow zones in the structure. The most critical regions to focus on are the nozzle throat and the welded interface between the thrust chamber and the propellant manifold. Therefore a more detailed view of the stress situation and the plastic strains at these locations is given in the next two Figures 5.11, and 5.12 for the stationary hot firing condition. The maximum $\bar{\sigma}$ values in the nozzle region are found in two circular patterns, downstream and upstream the throat (Fig. 5.11 (a)), where the temperature reaches a value of around 1900 K. The

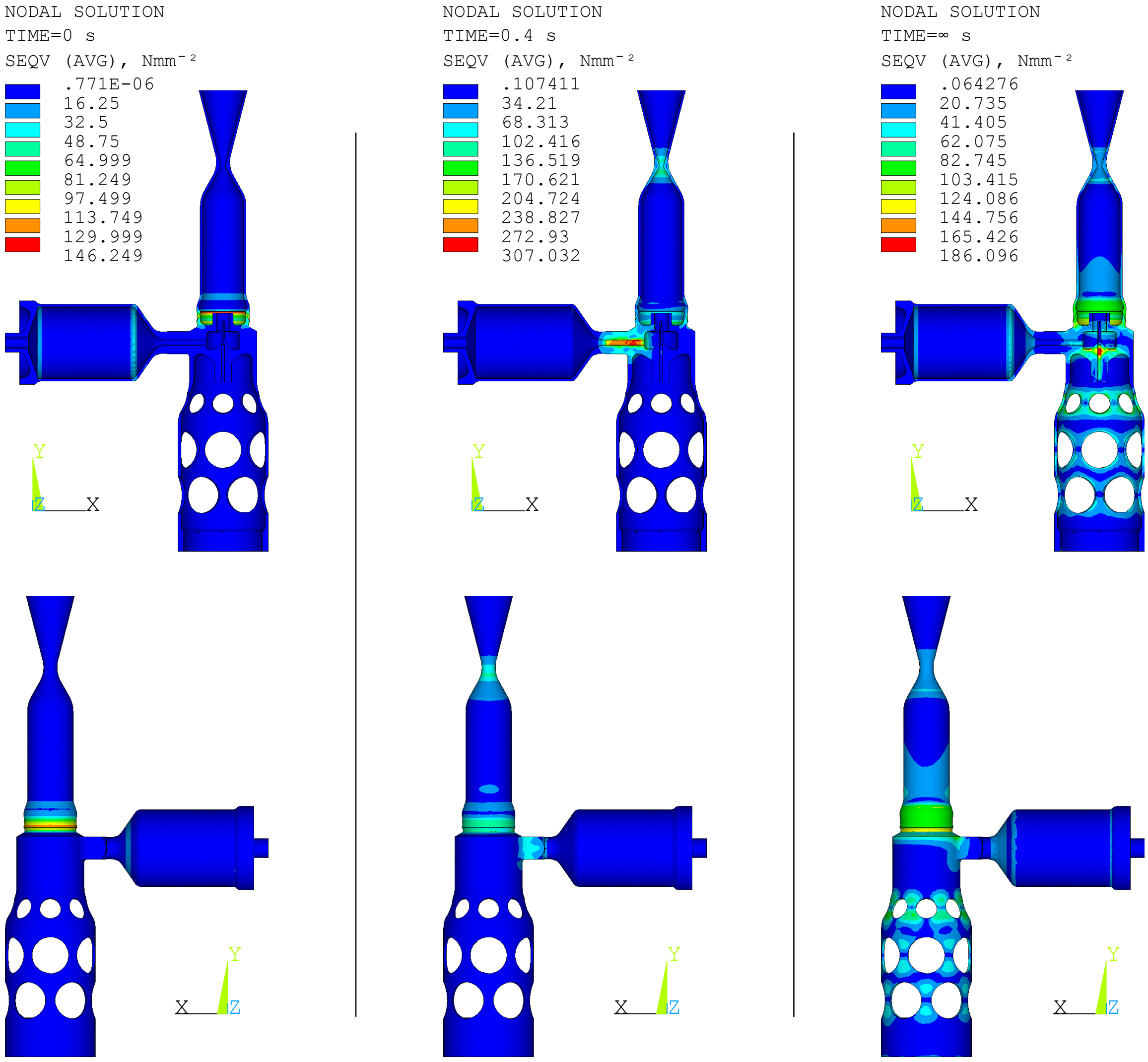
NODAL SOLUTION
TIME=0 s
SEQV (AVG), Nmm⁻²
.771E-06
16.25
32.5
48.75
64.999
81.249
97.499
113.749
129.999
146.249
NODAL SOLUTION
TIME=0.4 s
SEQV (AVG), Nmm⁻²
.107411
34.21
68.313
102.416
136.519
170.621
204.724
238.827
272.93
307.032
NODAL SOLUTION
TIME=∞ s
SEQV (AVG), Nmm⁻²
.064276
20.735
41.405
62.075
82.745
103.415
124.086
144.756
165.426
186.096
Y
Z
X

(a) (b) (c)

Figure 5.9: Distribution of the von Mises equivalent stress σ_{eq} ($SEQV$), plotted in the front (at top) and back view of the thruster, at the states of (a) stationary cold stand-by, (b) transient heating after 0.4 s, and (c) stationary hot operation.

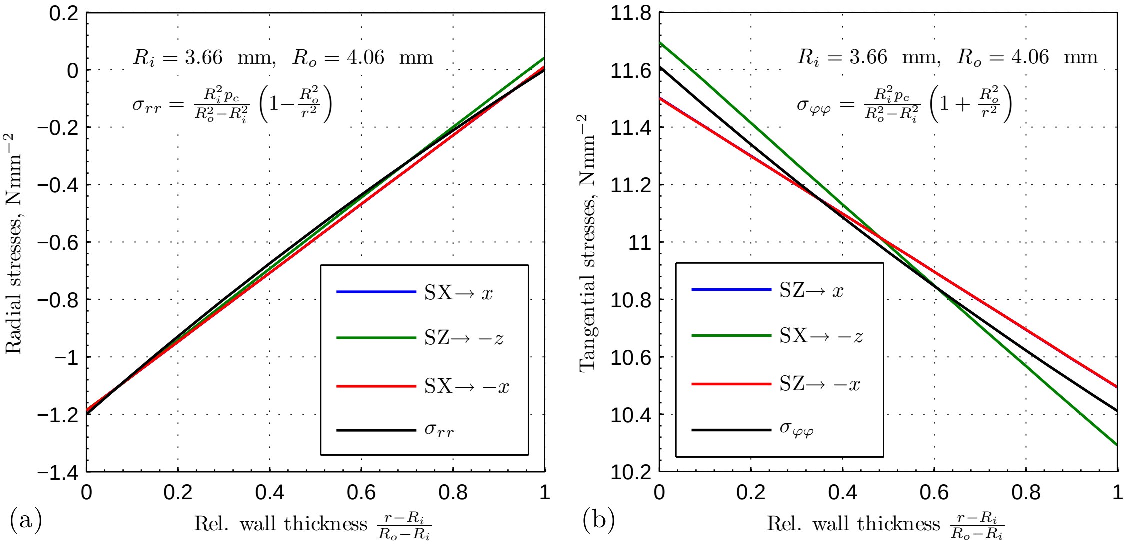

Figure 5.10: Radial stresses (a) and tangential stresses (b) at zero-time, in x, -z, and -x directions, located in the cross section in the middle of the cylindric combustion chamber, where the pressure $p_c = 12$ bar is acting inside.

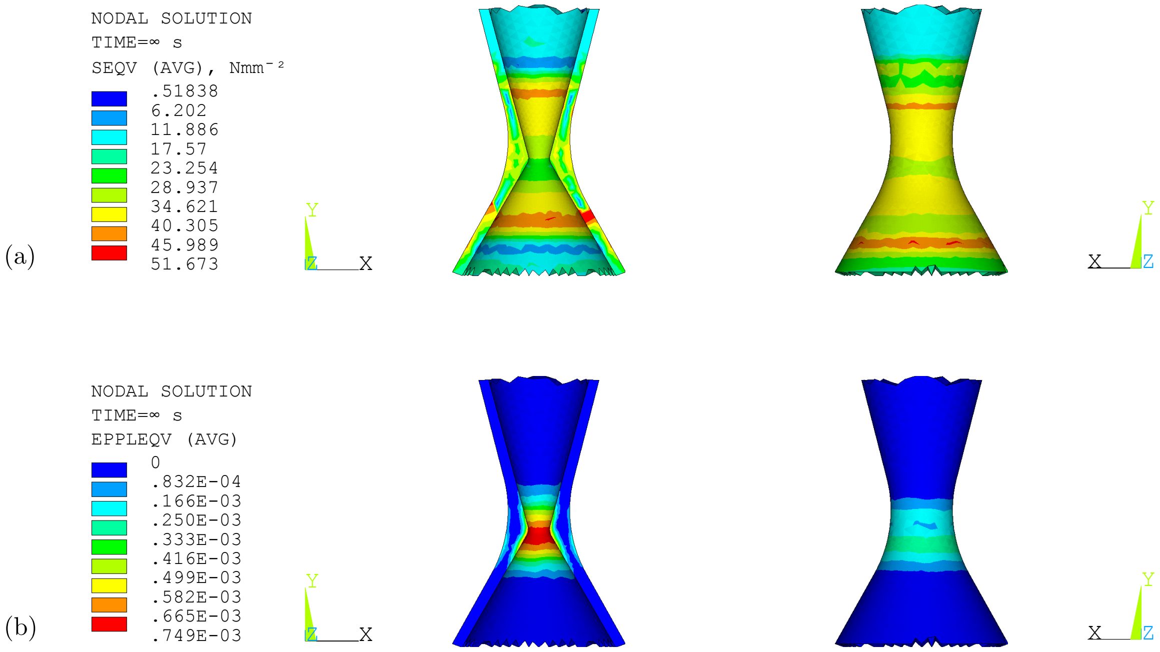
(a)
NODAL SOLUTION
TIME=∞ s
SEQV (AVG), Nmm⁻²
.51838
6.202
11.886
17.57
23.254
28.937
34.621
40.305
45.989
51.673
Y
Z
X
Y
X
Z
(b)
NODAL SOLUTION
TIME=∞ s
EPPLEQV (AVG)
0
.832E-04
.166E-03
.250E-03
.333E-03
.416E-03
.499E-03
.582E-03
.665E-03
.749E-03
Y
Z
X
Y
X
Z

Figure 5.11: Detailed contour plot of (a) equivalent stress σ_{eq} ($SEQV$), and (b) equivalent plastic strain ε_{eq}^{p} ($EPPLEQV$) in the nozzle, from the stationary hot solution, shown in the front (on the left) and back view.

stress concentration mainly adds from the hoop stresses due to the thermal gradient across the wall thickness, and from a thermal expansion of the throat in radial direction, that induces stresses in axial direction. At the circumferential locations with high $\bar{\sigma}$ values at the throat, the concentrated tangential stresses in these cross sections are of compressive type at the inner nozzle wall, shifting into tensile stresses towards the opposite side of the wall. The previous also applies to the axial stresses, which span over the whole region between the two circular extremes. A definite prediction about the creep behaviour of this thermo-mechanically critical zone can not be given. In fact the highest stress values exceed the creep-rupture value of 31.8 Nmm^{-2}, to last for one hour at 1923 K (from Table 3.3), but the probes used for creep tests are loaded with a uniform tensile stress. This is not the case in the present structure, even more the stress neutral and low zones inside the wall could improve the creep resistance significantly. The plastic flow (see Fig. 5.11 (b)) is limited to the narrow throat region. After the first heating the equivalent platic strain ε_{eq}^{p} reaches a value of about 0.075% inside the throat, where it is of compressive type in both tangential, and axial directions.

Figure 5.12 shows the same kind of results but for the propellant manifold, including the connection to the thrust chamber. The stresses here are highest, to arise in the structural model. The maximum σ_{eq} value is found at the bottom of the hydrogen peroxide prechamber. Radial tensile stresses are dominating at this location, induced by the temperature difference of about 200 K between the top and the bottom of the prechamber. The stress concentration in the vicinity of the fuel pipe is mainly because of the tensile hoop stresses due to the radial temperature gradient from the relatively cold fuel pipe wall towards the warmer structure. The circular stress concentrations at the base of the welding ring from to the manifold origin from the combined axial and tangential stresses, which are both compressive at the inner side and shift to tensile stresses at the outer side. Zones with plastic flow are depicted in Fig. 5.12 (b). In the stationary hot temperature field the affected zones are expanded into both materials of the joint. Radial and axial plastic strain components mainly add to the quasi rotationally symmetric ε_{eq}^{p} with a maximum value of 1.74% at the tip of the circular chamfer of the thrust chamber.

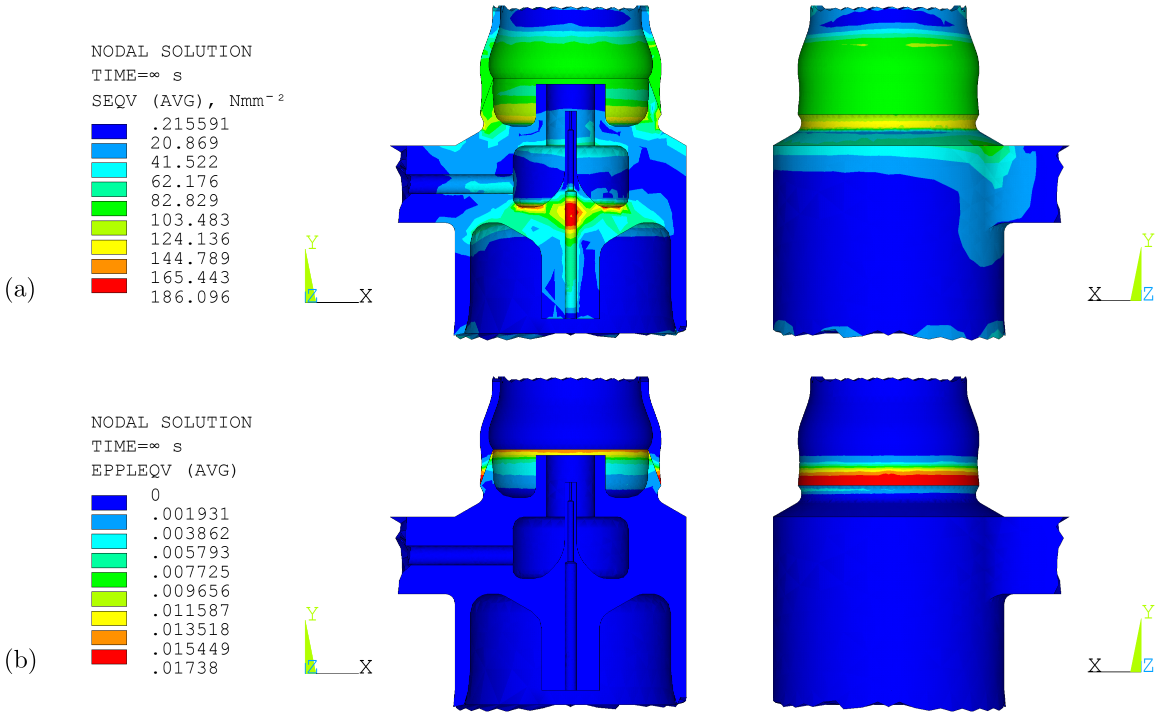

Figure 5.12: Detailed contour plot of (a) equivalent stress σ_{eq} ($SEQV$), and (b) equivalent plastic strain ε^p_{eq} ($EPPLEQV$) in the propellant manifold, from the stationary hot solution, shown in the front (on the left) and back view.

5.2.3 2-D Cyclic Thermo-Stress Analysis

The three dimensional FEA results from above have revealed a certain axially symmetric characteristic. This allows an estimation of the structural response onto cyclic thermal heating by use of an axis-symmetric 2-D FEA model (see Fig. 4.3 (b)), which is not as computationally intensive like the 3-D model. The temperature distribution of the thermal solution is not shwon as it is practically the same as shown in Section 5.2.1. During a load cycle the structure is exposed to the internal pressure (see Fig. 4.12 (c)), together with the temperature field of the stationary cold state at first, and solved. Next the temperature field is switched to the stationary hot operation state, the pressure remains unchanged, and the analysis is restarted. The load cycle ends with an analysis restart, again in the cold state. This is repeated for a total number of $n = 50$ load cycles. The stress components in the cross section of the nozzle region are plotted as contour diagrams in Figure 5.13 for the last cycle, in the hot condition. Both distributions of the axial stress σ_{zz} and the hoop stress $\sigma_{\varphi\varphi}$ can

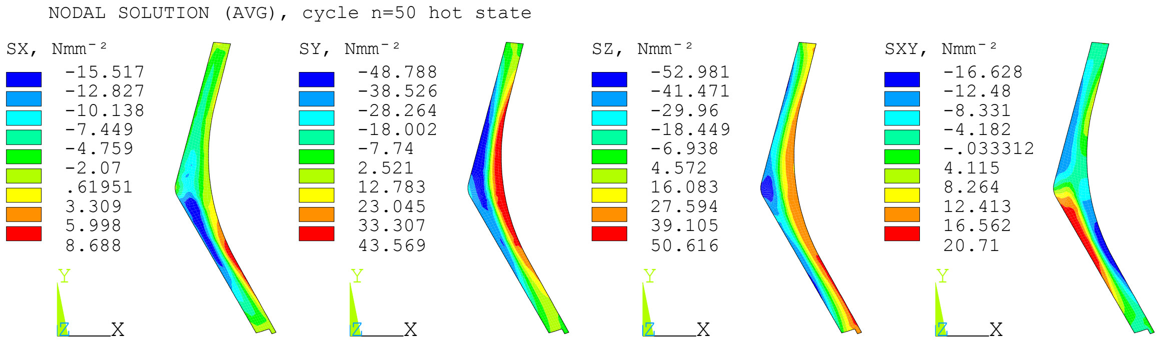

Figure 5.13: Stress components in radial σ_{rr} (SX), axial σ_{zz} (SY), and tangential $\sigma_{\varphi\varphi}$ (SZ) directions and shear stress σ_{rz} (SXY) at the nozzle region in the hot state of the 50th thermal cycle.

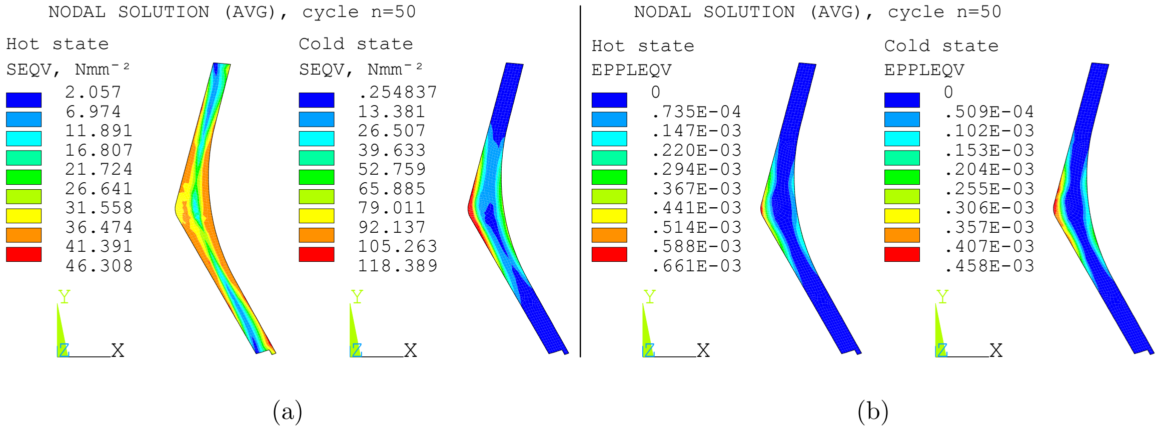

Figure 5.14: Contour plot of (a) equivalent stress σ_{eq} ($SEQV$), and (b) equivalent plastic strain ε^p_{eq} ($EPPLEQV$) in the hot state as well as the cold state of the 50th thermal cycle.

be linked to different thermal strain magnitudes, induced by the temperature gradient across the wall of the nozzle throat. The combination of these stress values in terms of the von Mise stress σ_{eq} is plotted in Figure 5.14 (a) for the same area, in both the hot and cold condition. In both states a band with very low stress values is present in the centre of the throat wall. The higher σ_{eq} values, in the cold state are linked to the temperature dependent material properties, as mentioned above. The plastic equivalent strains, expressed through ε^p_{eq} of equation 5.2, are shown in Fig. 5.14 after the completion of 50 load cycles. The areas with plastic flow are located at the inner and outer sides of the nozzle wall in the proximity of the throat. At the inside the components in axial ε^p_{zz} and tangential $\varepsilon^p_{\varphi\varphi}$ direction are compressive strains, whereas

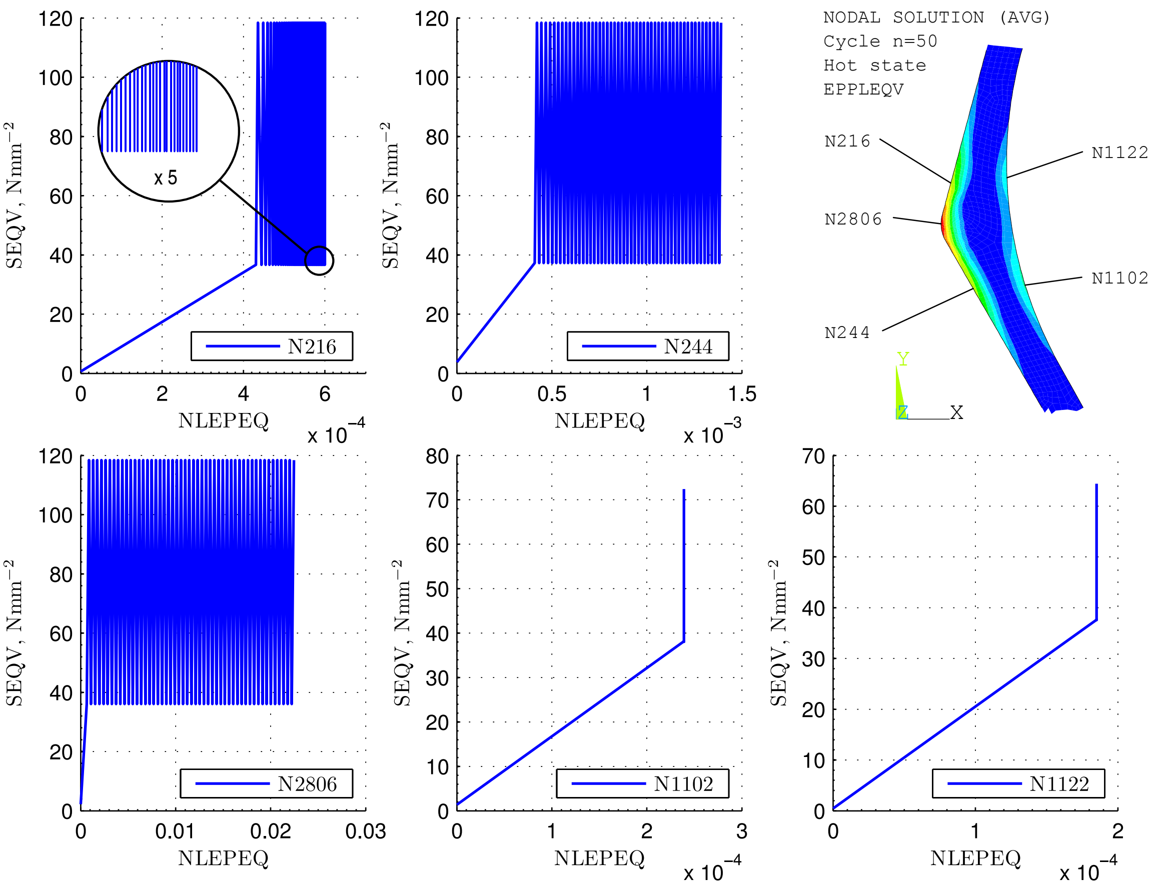

Figure 5.15: Stress σ_{eq} $(SEQV)$ - accumulated equivalent plastic strain $\bar{\varepsilon}^p$ $(NLEPEQ)$ load history digrams of selected nodes at the nozzle throat over 50 cycles.

tensile strains are present at the outside. Since the ε^p_{eq} strain values increase with the number of thermal load cycles cyclic plastification is present in this case. The question if cyclic loading, in this case the changing temperature field, leads to either a stable plastic deformation (plastic shake down) or a progressive one due to ratcheting, is of great importance to predict the life span of a structure. This is the main reason, why cyclic loading was simulated in the end. Figure 5.15 shows the resulting load history diagrams of selected nodes, with $\bar{\varepsilon}^p$ strains plotted at the abscissa and the values of σ_{eq} over the ordinate, after the completion of 50 thermal cycles. Obviously the plastic deformations at the outer nodes N1102 and N1122 are of the stable type where the increment of $\Delta\bar{\varepsilon}^p = 0$. Each of the nodes that are located at the inner side developes ratcheting as plastic flow type. Considering node N216 for example the gain from the second up to the last load cycle is ${}^{50}\bar{\varepsilon}^p - {}^{2}\bar{\varepsilon}^p = 1.6467 \cdot 10^{-4}$, or 27.4% of the total accumulated strain value ${}^{50}\bar{\varepsilon}^p = 6.0 \cdot 10^{-4}$, while the the plastic equivalent strain at the end of the last cycle reaches a value of ${}^{50}\varepsilon^p_{eq} = 4.6 \cdot 10^{-4}$. The total accumulated strain at node N2806 with the strongest plastic deformation to be found in this area is ${}^{50}\bar{\varepsilon}^p = 2.24 \cdot 10^{-2}$ with an increment of $\Delta\bar{\varepsilon}^p = 4.4 \cdot 10^{-4}$ each cycle. Again the plastic equivalent strain at node N2806 has a much lower value of ${}^{50}\varepsilon^p_{eq} = 4.4 \cdot 10^{-4}$. The differences between the two strain values $\bar{\varepsilon}^p$ and ε^p_{eq} indicate that the loading pathes during cyclic loading are not radial with a constant orientation in the space of plastic strain increments. Even revertive yielding during the cooling phase might be expected.

Finally the results for the cross sectional area around the bi-material welding zone are presented as above in the next figures. Nodal stress components in the hot state of the 50th load cycle are depicted in Figure 5.16, the equivalent stresses in the hot and cold state are shown in Figure 5.17 (a). The values are not averaged at the material interface. The distributions of the σ_{zz} and $\sigma_{\varphi\varphi}$ stresses in the proximity of the joint are the result of the much higher CTE value of the NiCr25FeAlY alloy from the propellant mainfold compared with the CTE of iridium at the same temperatures. Therefore the thermal expansion of the manifold gets restricted by the combustion chamber, which is widened inversely by the former one. The von Mises stress σ_{eq} reaches the maximum in the welding ring of the injector for both states. Figure 5.17 (b) shows the formation of plastic deformations in both materials near the joint. Hence in the low temperature field the difference in material yield strength values $\mathrm{R_{p0.2}}$ near 293 K, becomes clearly visible by the σ_{eq} stress discontinuity at the material interface along the joint. A great area of the iridium part from the joint is affected by plastic flow. The point with the considerable maximum ε^p_{eq} value of about 16.3% is also found therein, which could likely be the starting place of developing flaws. During each thermal cycle the wall locally bulges inwards and gets increasingly kinked at this point. The load history diagrams in Figure 5.18 show the magnitude of accumulated plastification at specific nodes located at the joint. Node N634 at the lower edge of the bi-material wedge outside shows the highest increase of accumulated plastic strain after 50 cycles, reaching a value of ${}^{50}\bar{\varepsilon}^p = 1.507$ with an increment of $\Delta\bar{\varepsilon}^p = 3.01 \cdot 10^{-2}$ or about 3% each cycle. Node N702 located at the hot spot of the ε^p_{eq} strain contour shows a similar evolution with a gain of $\Delta\bar{\varepsilon}^p = 1.22 \cdot 10^{-2}$ or 1.2% each periode and a value of ${}^{50}\bar{\varepsilon}^p = 0.611$. The totally accumulated equivalent plastic strain values ${}^{50}\bar{\varepsilon}^p$

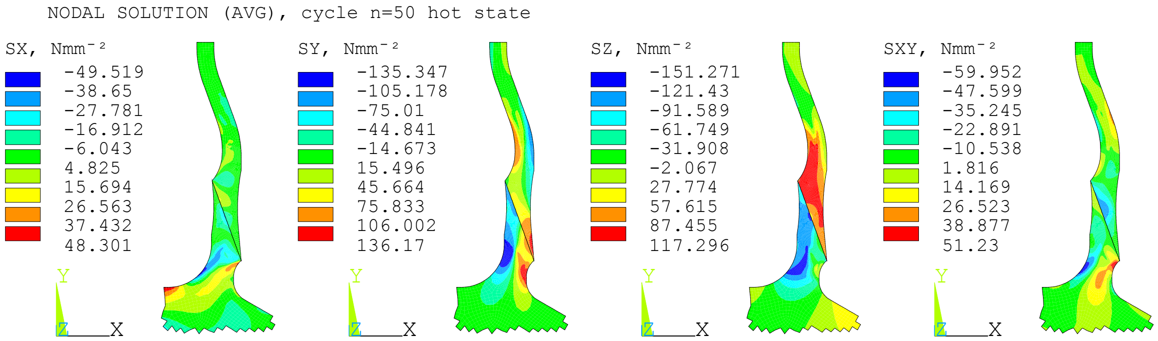

Figure 5.16: Stress components in radial σ_{rr} (SX), axial σ_{zz} (SY), and tangential $\sigma_{\varphi\varphi}$ (SZ) directions and shear stress σ_{rz} (SXY) in the proximity of the welded joint in the hot state of the 50th thermal cycle.

at the other nodes range from 24.7% at N624, 56.7% at N666, up to 84.6% at N4454. The increments $\Delta\bar{\varepsilon}^p$ at each cycle are approximately 0.5% at N624, 1.1% at N666, and 1.7% at N4454. Former plastic strain values indicate that a material failure due to ratcheting is likely to occour within a few thermal load cycles. The accumulated equivalent plastic strain increments of this scale in the proximity of the joint will add microstructural damage to a certain extent in both materials. A crack initiation is more likely to occur firstly in the upper part of the joint than in the lower section made of nicke base alloy, because of the brittle behaviour of iridium at lower temperatures. Although the ultimate stress of iridium $R_m = 395$ Nmm^{-2} at 298 K provides some load-bearing buffer in terms of work hardening, this one becomes deminished by a low breaking elongation of only 9.6%.

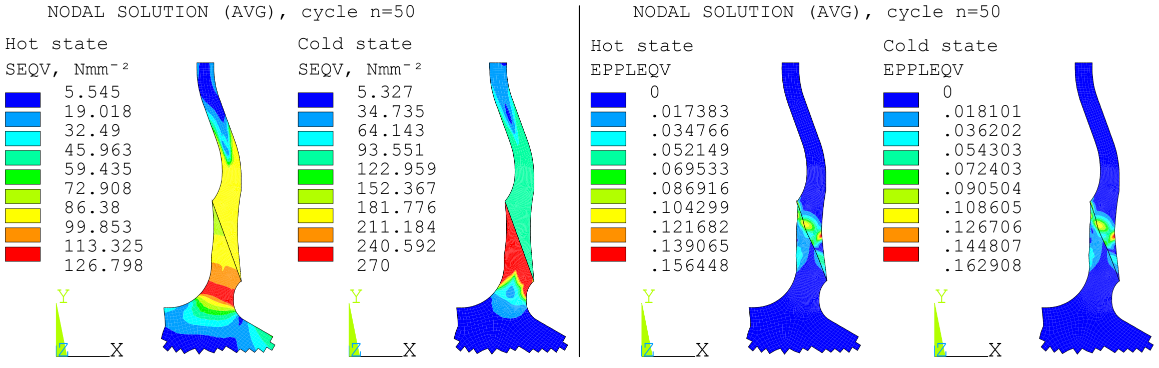
NODAL SOLUTION (AVG), cycle n=50
Hot state
SEQV, Nmm⁻²
5.545
19.018
32.49
45.963
59.435
72.908
86.38
99.853
113.325
126.798
Cold state
SEQV, Nmm⁻²
5.327
34.735
64.143
93.551
122.959
152.367
181.776
211.184
240.592
270
NODAL SOLUTION (AVG), cycle n=50
Hot state
EPPLEQV
0
.017383
.034766
.052149
.069533
.086916
.104299
.121682
.139065
.156448
Cold state
EPPLEQV
0
.018101
.036202
.054303
.072403
.090504
.108605
.126706
.144807
.162908
Y
Z
X

(a) (b)

Figure 5.17: Contour plot of (a) equivalent stress σ_{eq} ($SEQV$), and (b) equivalent plastic strain ε^p_{eq} ($EPPLEQV$) in the hot state as well as the cold state of the 50th thermal cycle.

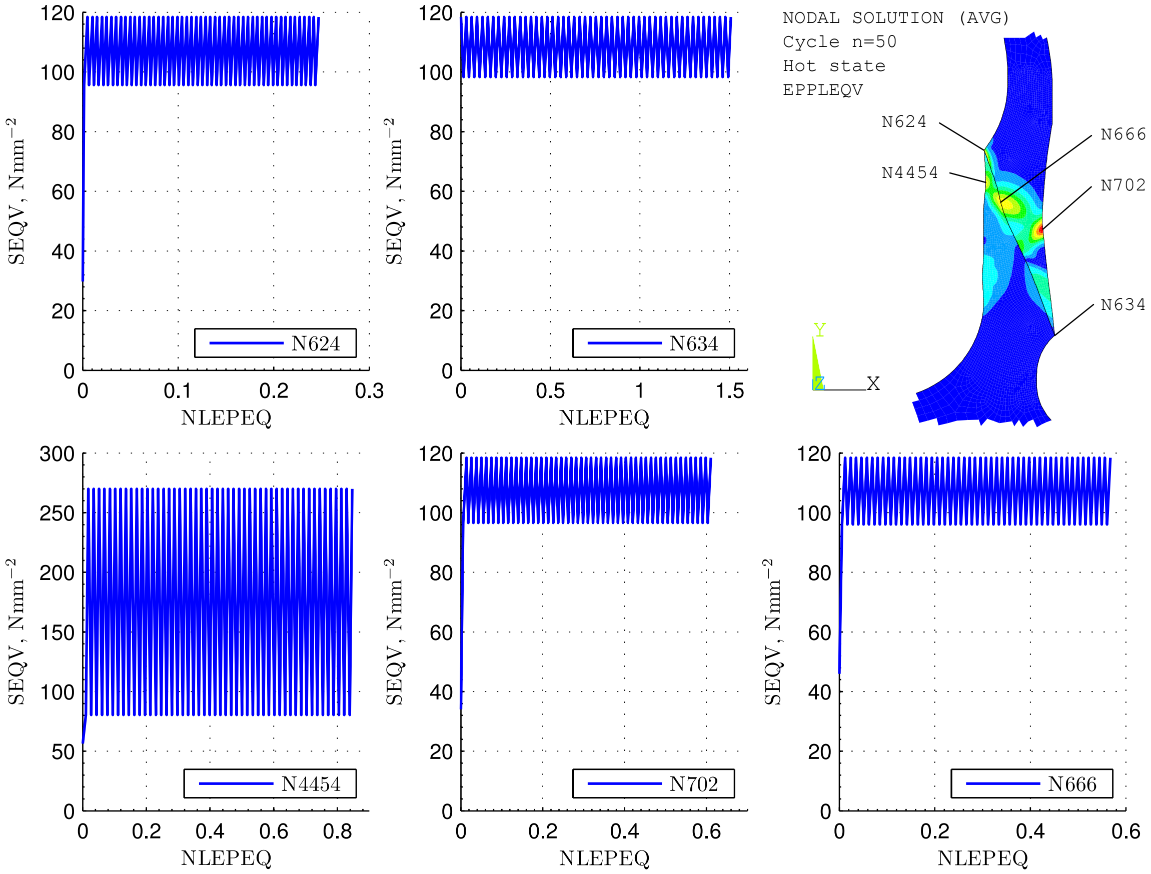

Figure 5.18: Stress σ_{eq} ($SEQV$) - plastic strain ε^p_{eq} ($EPPLEQV$) load history digrams of selected nodes in the joint region over 50 cycles.

6 Conclusion

The thruster, investigated in the context of this work, is a preliminary design study whereof the geometry of the exemplaric model for the finite elements analysis was derived from. Thermal and mechanical loads were defined and implemented. The physical model used to describe the fluid flow is one-dimensional, isentropic by assuming ideal gas behaviour, which is a strong idealisation of the real circumstances.

Materials were mechanically idealised to be of perfect plasticity post yield type, with temperature dependent property parameters. At this point a more sophisticated model to describe the constitutive equation could be used in coming simulations, if associated material test data is provided. The thermal results showed a rapide heating of the thrust chamber within five seconds after ignition mainly due to the high values of the heat flux in the nozzle. The maximum temperatures in the stationary hot state exceed the limit of the service temperature form the Pt-10%Rh DPH alloy in the vicinity of the nozzle throat. The iridium configuration was found to be capable of bearing the thermal load in a tolerable temperature range. Plastic deformations in the wall section of the nozzle throat, as well as on both sides of the bi-material joint developed after the first heat up. Cyclic thermal loading caused strong ratcheting in the wall region around the bi-material joint. Here the highest values of accumulated equivalent plastic strain occured in the iridium part of the joint. In this case the structural bearing is a matter of low-cycle fatigue and the lifespan must be considered to be very limited.

A spacer ring made of a more ductile material compared to iridium, like a Pt-Ir alloy, could be inserted as part of the combustion chamber between the injector and the iridium thrust chamber as a relief effort. In this area temperatures are low enough allowing the use of a platinum alloy. The existing Pt-Ir alloys with an Iridium content of up to 40wt% and the lack of intermetallic compounds in the Pt-Ir system indicate that joining of these materials by welding should be possible. The cyclic loading from the stationary thermal cold state followed by the hot state, as conducted in this work, represent the thermo-mechanical worst case. Hence the inquiry of pulse mode operation would be an important point, if certain operational specifications are available. In addition to the thermal stress analysis, the evaluation of stresses caused by the dynamic load spectra during the rocket launch periode should be conducted to guarantee the structural integrity of the truster.

A Appendix

A.1 Integrals from the turbulent boundary-layer analysis

Gauss-Legendre integration method: The general definition is

$$\int_{-1}^{1} f(x)\mathrm{d}x \approx \sum_{i=1}^{n} w_i f(x_i) \tag{A.1}$$

where the w_i represent weight factors at the integration points x_i, which are the zeros of the Legendre polynomials. Values are listed for the order $n = 10$ in Table A.1, from [52]. Arbitrary integration limits have to be transformed to coincide with $[-1, 1]$ by the following substituion

$$\int_{a}^{b} f(s)\mathrm{d}s = \frac{b-a}{2} \int_{-1}^{1} f\left(x\frac{b-a}{2} + \frac{b+a}{2}\right) \mathrm{d}x. \tag{A.2}$$

Table A.1: Weights w_i and integration points x_i for Gauss-Legendre method of order $n = 10$, from [52].

w_i	x_i
$w_{10} = w_1 = 0.066671344308688$	$x_{10} = -x_1 = 0.973906528517172$
$w_9 = w_2 = 0.149451349150581$	$x_9 = -x_2 = 0.865063366688985$
$w_8 = w_3 = 0.219086362515982$	$x_8 = -x_3 = 0.679409568299024$
$w_7 = w_4 = 0.269266719309996$	$x_7 = -x_4 = 0.433395394129247$
$w_6 = w_5 = 0.295524224714753$	$x_6 = -x_5 = 0.148874338981631$

The integrals from the turbulent boundary-layer analysis are then given as

$$I_1 = \int_0^1 \frac{s^7(1-s)}{1+\frac{C_1}{\zeta}s - C_2 s^2}\mathrm{d}s \approx \frac{1}{2}\sum_{i=1}^{10} w_i \left[\frac{\left(\frac{x_i+1}{2}\right)^7\left(1-\left(\frac{x_i+1}{2}\right)\right)}{1+\frac{C_1}{\zeta}\left(\frac{x_i+1}{2}\right) - C_2\left(\frac{x_i+1}{2}\right)^2}\right], \tag{A.3}$$

$$I_2 = \int_0^1 \frac{s^7}{1+\frac{C_1}{\zeta}s - C_2 s^2}\mathrm{d}s \approx \frac{1}{2}\sum_{i=1}^{10} w_i \left[\frac{\left(\frac{x_i+1}{2}\right)^7}{1+\frac{C_1}{\zeta}\left(\frac{x_i+1}{2}\right) - C_2\left(\frac{x_i+1}{2}\right)^2}\right], \tag{A.4}$$

$$I_3 = \int_1^\zeta \frac{s^6}{1+\frac{C_1}{\zeta}s - C_2}\mathrm{d}s \approx \frac{\zeta-1}{2}\sum_{i=1}^{10} w_i \left[\frac{\left(x_i\frac{\zeta-1}{2}+\frac{\zeta+1}{2}\right)^6}{1+\frac{C_1}{\zeta}\left(x_i\frac{\zeta-1}{2}+\frac{\zeta+1}{2}\right) - C_2}\right], \tag{A.5}$$

$$I_4 = \int_0^\zeta \frac{s^7(1-s)}{1+\frac{C_1}{\zeta}s - C_2 s^2}\mathrm{d}s \approx \frac{\zeta}{2}\sum_{i=1}^{10} w_i \left[\frac{\left(\frac{\zeta(x_i+1)}{2}\right)^7\left(1-\left(\frac{\zeta(x_i+1)}{2}\right)\right)}{1+\frac{C_1}{\zeta}\left(\frac{\zeta(x_i+1)}{2}\right) - C_2\left(\frac{\zeta(x_i+1)}{2}\right)^2}\right], \tag{A.6}$$

$$I_5 = \int_\zeta^1 \frac{s^7(1-s)}{1+C_1 - C_2 s^2}\mathrm{d}s \approx$$

$$\frac{1-\zeta}{2}\sum_{i=1}^{10} w_i \left[\frac{\left(x_i\frac{1-\zeta}{2}+\frac{\zeta+1}{2}\right)^7\left(1-\left(x_i\frac{1-\zeta}{2}+\frac{\zeta+1}{2}\right)\right)}{1+C_1 - C_2\left(x_i\frac{1-\zeta}{2}+\frac{\zeta+1}{2}\right)^2}\right], \tag{A.7}$$

$$I_6 = \int_0^\zeta \frac{s^7}{1+\frac{C_1}{\zeta}s - C_2 s^2}\mathrm{d}s \approx \frac{\zeta}{2}\sum_{i=1}^{10} w_i \left[\frac{\left(\frac{\zeta(x_i+1)}{2}\right)^7}{1+\frac{C_1}{\zeta}\left(\frac{\zeta(x_i+1)}{2}\right) - C_2\left(\frac{\zeta(x_i+1)}{2}\right)^2}\right], \tag{A.8}$$

$$I_7 = \int_\zeta^1 \frac{s^7}{1+C_1 - C_2 s^2}\mathrm{d}s \approx \frac{1-\zeta}{2}\sum_{i=1}^{10} w_i \left[\frac{\left(x_i\frac{1-\zeta}{2}+\frac{\zeta+1}{2}\right)^7}{1+C_1 - C_2\left(x_i\frac{1-\zeta}{2}+\frac{\zeta+1}{2}\right)^2}\right], \tag{A.9}$$

(A.10)

$$I_1' = \int\limits_0^1 \frac{s^7(1-s)}{1+C_1 s - C_2\zeta^2 s^2}\mathrm{d}s \approx \frac{1}{2}\sum_{i=1}^{10} w_i \left[\frac{\left(\frac{x_i+1}{2}\right)^7 \left(1-\left(\frac{x_i+1}{2}\right)\right)}{1+C_1\left(\frac{x_i+1}{2}\right) - C_2\zeta^2\left(\frac{x_i+1}{2}\right)^2}\right], \tag{A.11}$$

$$I_2' = \int\limits_0^{\frac{1}{\zeta}} \frac{s^7(1-s)}{1+C_1 s - C_2\zeta^2 s^2}\mathrm{d}s \approx \frac{1}{2\zeta}\sum_{i=1}^{10} w_i \left[\frac{\left(\frac{x_i+1}{2\zeta}\right)^7 \left(1-\left(\frac{x_i+1}{2\zeta}\right)\right)}{1+C_1\left(\frac{x_i+1}{2\zeta}\right) - C_2\zeta^2\left(\frac{x_i+1}{2\zeta}\right)^2}\right], \tag{A.12}$$

$$I_3' = \int\limits_{\frac{1}{\zeta}}^{1} \frac{s^6(1-s)}{1+C_1 s - C_2}\mathrm{d}s \approx$$

$$\frac{\zeta-1}{2\zeta}\sum_{i=1}^{10} w_i \left[\frac{\left(\frac{x_i(\zeta-1)}{2\zeta}+\frac{\zeta+1}{2\zeta}\right)^6 \left(1-\left(\frac{x_i(\zeta-1)}{2\zeta}+\frac{\zeta+1}{2\zeta}\right)\right)}{1+C_1\left(\frac{x_i(\zeta-1)}{2\zeta}+\frac{\zeta+1}{2\zeta}\right) - C_2}\right], \tag{A.13}$$

where

$$C_1 = \frac{T_0}{T_w} - 1, \tag{A.14}$$

$$C_2 = \left(\frac{\kappa-1}{2}M^2\right)\left(\frac{T}{T_w}\right). \tag{A.15}$$

Bibliography

[1] *Release 11.0 Documentation for ANSYS.* ANSYS, Inc., 2007.

[2] Nicrofer® 6025 HT – alloy 602 CA. Technical Report Werkstoffblatt-Nr. 4137, ThyssenKrupp VDM GmbH, 2007. URL `www.thyssenkruppvdm.de`.

[3] Physical properties of the platinum metals. *Platinum Metals Review*, 16(2):59, 1972.

[4] High-temperature alloys from Krupp VDM for industrial engineering. Technical Report VDM REPORT No. 25, ThyssenKrupp VDM GmbH, 2000. URL `www.thyssenkruppvdm.de`.

[5] *Ariane 5 User's Manual.* Arianespace, 0th revision, 5th edition, 2008. URL `www.arianespace.com`.

[6] R. Arnold. *Experimentelle Untersuchung zur Filmkühlung in Raketenbrennkammern.* Cuvillier Verlag, Göttingen, 2008.

[7] C. R. Barber. The platinum metals in the measurement of temperature. *Platinum Metals Review*, 13(2):65–67, 1969.

[8] D. R. Bartz. A simple equation for rapid estimation of rocket nozzle convective heat-transfer coefficients. *Jet Propulsion vol. 27*, pages 49–51, 1957.

[9] G.P. Sutton; S. Biblarz. *Rocket Propulsion Elements*, page 286 pp. John Wiley & Sons, 7th edition, 2001.

[10] G.P. Sutton; S. Biblarz. *Rocket Propulsion Elements*, chapter 8. John Wiley & Sons, 7th edition, 2001.

[11] R. D. Bitsche. *Design and computational analysis of compound castings and other multi-material structures.* PhD thesis, Technische Universität Wien, 2009.

[12] N. Wingborg; M. Johansson; L. Bodin. *ADN-Based Liquid Monopropellants: Propellant Selection and Initial Thruster Development.* 3rd Int. Conf. on Green Propellant for Space Propulsion, France, (ESA SP-635, Dec. 2006), 2006.

[13] C. Kirchberger; R. Wagner; H.-P. Kau; S. Soller; P. Martin; M. Bouchez; C. Bonzom. *Prediction and Analysis of Heat Transfer in Small Rocket Chambers.* AIAA-2008-1260, 46th AIAA Aerospace Sciences Meeting and Exhibit, 2008.

[14] D.C. Agarwal; U. Brill. Combating high temperature corrosion with alloy 602CA (UNS N06025) in various environments and industries. CORROSION 2002, Paper No. 02372, NACE International, Houston, Texas, 2002.

[15] C. M. Chimani, H. J. Böhm, and F. G. Rammerstorfer. On stress singularities at free edges of bimaterial junctions – a micromechanical study. *Scripta Materialia*, 36(8):943 – 947, 1997.

[16] B. Barter; A. S. Darling. Thermal expansion of rhodium-platinum alloys. *Platinum Metals Review*, 4(4):138–140, 1960.

[17] The PGM Database. URL `http://www.platinummetalsreview.com/jmpgm/index.jsp`.

[18] European Aeronautic Defence and Space Company (EADS) Astrium. URL `http://cs.astrium.eads.net/sp/SpacecraftPropulsion/Showcase/AlphaBus.htm`.

[19] Centre National d'Etudes Spatiales (CNES). URL `http://smsc.cnes.fr/MYRIADE/GP_plateforme.htm`.

[20] R. Völkl; B. Fischer; R. Teschner; D.Lupton. Finite element modelling of strains and stresses in platinum alloy bushings for textile glass fibre production. *Glass Science and Technology*, 74(5):2–11, 2001.

[21] B. Fischer et al. High temperature tensile properties of platinum materials. 27th International Precious Metals Conference, Dorado, Puerto Rico, 2003, .

[22] D. F. Lupton et al. Platinum materials for the glass industry. 24th International Precious Metals Conference, Williamsburg, USA, 2000, .

[23] R. Völkel et al. Platinum base alloys for high temperature space applications. 6th European Conference on Advanced Materials and Processes (EUROMAT 99), Munich, Germany, 1999,, .

[24] R. Weiland et al. High-temperature mechanical properties of the platinum group metals. *Platinum Metals Review*, 50(4):158–170, 2006.

[25] E. Messerschmid; S. Fasoulas. *Raumfahrtsysteme*, pages 258–262. Springer-Verlag Berlin Heidelberg, 3rd edition, 2009.

[26] E. Messerschmid; S. Fasoulas. *Raumfahrtsysteme*, pages 287–294. Springer-Verlag Berlin Heidelberg, 3rd edition, 2009.

[27] Back L. H.; P. F. Massier; H. L. Gier. Convective heat transfer in a convergent-divergent nozzle. *Int. J. Heat and Mass Transfer, vol. 7*, pages 549–568, 1964.

[28] L. Gimeno-Fabra. *Design, Manufacture and Properties of Cr-Re Alloys for Application in Satellite Thrusters.* PhD thesis, Universitat Politècnica de Catalunya, UPC, 2006.

[29] S. Timoshenko; J. N. Goodier. *Theory of Elasticity*, page 59. McGraw-Hill Book Company, 2 edition, 1951.

[30] J. R. Handley. Increasing applications for iridium. *Platinum Metals Review*, 30 (1):12–13, 1986.

[31] R. W. Freund; R. H. W. Hoppe. *Stoer/Bulirsch: Numerische Mathematik 1*, pages 187–196. Springer-Verlag Berlin Heidelberg, 10th edition, 2007.

[32] D. K. Huzel; D. H. Huang. Design of liquide propellant rocket engines. Technical Report NASA-SP-125, National Aeronautics and Space Administration, 1971.

[33] Verein Deutscher Ingenieure, editor. *Dubbel*, page D 26. Springer-Verlag Berlin Heidelberg New York, 20th edition, 2001.

[34] Verein Deutscher Ingenieure, editor. *VDI-WÄRMEATLAS*, pages Dca 8–36. Springer-Verlag Berlin Heidelberg New York, 10th edition, 2006.

[35] Verein Deutscher Ingenieure, editor. *VDI-WÄRMEATLAS*, pages Mn14–15. Springer-Verlag Berlin Heidelberg New York, 10th edition, 2006.

[36] C. T. Liu; H. Inouye. Study of iridium and iridium–tungsten alloys for space radioisotopic heat sources. Technical Report ORNL-5240, Oak Ridge National Laboratory, 1976.

[37] Reed B. D.; Biaglow J. A.; Schneider S. J. Iridium-coated rhenium radiation-cooled rockets. Technical Report NASA-TM-107453, Lewis Research Center, 1997.

[38] Reed B. D.; Schneider S. J. Testing of wrought iridium/chemical vapor deposition rhenium rocket. Technical Report NASA-TM-107452, Lewis Research Center, 1996.

[39] J. Merke; D. Lupton; M. Topfer; H. Knake. High temperature mechanical properties of the platinum group metals. *Platinum Metals Review*, 45(2):74–82, 2001.

[40] Bombelli V.; Simon D.; Marée T.; Moerel J. L. *Economic Benefits of the Use of Non-Toxic Mono-Propellants for Space Craft Applications.* AIAA-2003-4783, 39th Joint PropulsionConference, 2003.

[41] Jones W. L.; Quentmeyer R. J.; Schacht R. L. Experimental investigation of hot-gas side heat-transfer rates for a hydrogen-oxygen rocket. Technical Report NASA-TN-D-2832, National Aeronautics and Space Administration, 1965.

[42] D. Lee and J. R. Barber. An automated procedure for determining asymptotic elastic stress fields at singular points. *Journal of Strain Analysis for Engineering Design*, 41(4):287–295, 2006.

[43] E. P. George; C. G. McKamey; E. K. Ohriner; E. H. Lee. Deformation and fracture of iridium: microalloying effects. *Materials Science and Engineering A*, 319-321:466–470, 2001.

[44] S. Gordon; B. McBride. Computer program for calculation of complex chemical equilibrium compositions and applications. Technical Report NASA Reference Publication 1311, National Aeronautics and Space Administration, 1994.

[45] E. K. Ohriner. Processing of iridium and iridium alloys. *Platinum Metals Review*, 52(3):186–197, 2008.

[46] H.-J. Bargel; G. Schulze. *Werkstoffkunde*, pages 286–289. Springer-Verlag Berlin Heidelberg, 10 edition, 2008.

[47] D. G. Elliot; D. R. Bartz; S. Silver. Calculation of turbulent boundary-layer growth and heat transfer in axi-symmetric nozzles. Technical Report 32-387, Jet Propulsion Laboratory, 1963.

[48] G.B. Sinclair. Stress singularities in classical elasticity–i: Removal, interpretation, and analysis. *Applied Mechanics Reviews*, 57(4):251–298, 2004.

[49] G.B. Sinclair. Stress singularities in classical elasticity–ii: Asymptotic identification. *Applied Mechanics Reviews*, 57(5):285–439, 2004.

[50] H. P. Singh. Determination of thermal expansion of germanium, rhodium and iridium by x-rays. *Acta Crystallographica Section A*, 24(4):469–471, 1968.

[51] D. Schlain; F. X. McCawley; G. R. Smith. Electrodeposition of platinum metals from molten cyanides. *Platinum Metals Review*, 21(2):38–42, 1977.

[52] M. Abramowitz; I. A. Stegun, editor. *Handbook of Mathematical Functions*, page 916. Washington, DC: National Bureau of Standards, 10th edition, 1972.

[53] M. Tajmar. *Advanced Space Propulsion Systems*, pages 20–22. Springer-Verlag Wien New York, 2003.

[54] M. Turner. *Rocket and Spacecraft Propulsion*, pages 101–103. Springer-Verlag Berlin Heidelberg New York, 3rd edition, 2009.

[55] K. Meyberg; P. Vachenauer. *Höhere Mathematik 2*, pages 59–62. Springer-Verlag Berlin Heidelberg New York, 4th edition, 2003.

[56] P. Panfilov; A. Yermakov. Brittle intercrystalline fracture in iridum. *Platinum Metals Review*, 45(4):179–183, 2001.

[57] V.A. Zinov'yev. *Metals At High Temperatures: Standard handbook of properties*, pages 195–202. Hemisphere Publishing Corporation, 1990.